Fabiano Fernandes Bargos

Aspects of the Discretized Peridynamic Theory and the Finite Element Method for Concurrent Multiscale Simulation

Aspectos da Teoria Peridinâmica Discretizada e do Método dos Elementos Finitos para Simulação em Múltiplas Escalas Concorrentes

26/2013

CAMPINAS

2013

UNIVERSIDADE ESTADUAL DE CAMPINAS
FACULDADE DE ENGENHARIA MECÂNICA

Fabiano Fernandes Bargos

Aspects of the Discretized Peridynamic Theory and the Finite Element Method for Concurrent Multiscale Simulation

Supervisor: Prof. Dr. Marco Lúcio Bittencourt

Aspectos da Teoria Peridinâmica Discretizada e do Método dos Elementos Finitos para Simulação em Múltiplas Escalas Concorrentes

Doctoral Thesis presented to the Faculty of Mechanical Engineering, University of Campinas, to obtain the PhD grade in Mechanical Engineering in the area of Solid Mechanics and Mechanical Design.

Tese de Doutorado apresentada à Faculdade de Engenharia Mecânica da Universidade Estadual de Campinas, para a obtenção do título de Doutor em Engenharia Mecânica, na área de Mecânica dos Sólidos e Projeto Mecânico.

ESTE EXEMPLAR CORRESPONDE À VERSÃO FINAL DA TESE DEFENDIDA PELO ALUNO FABIANO FERNANDES BARGOS, E ORIENTADA PELO PROF. DR. MARCO LÚCIO BITTENCOURT

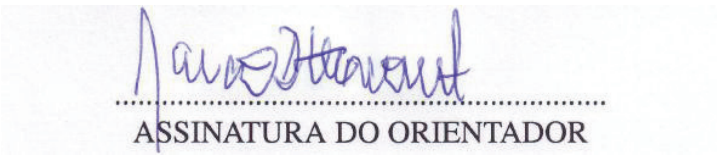

ASSINATURA DO ORIENTADOR

CAMPINAS
2013

Ficha catalográfica
Universidade Estadual de Campinas
Biblioteca da Área de Engenharia e Arquitetura
Rose Meire da Silva - CRB 8/5974

B238a

Bargos, Fabiano Fernandes, 1984-
Aspectos da teoria peridinâmica discretizada e do método dos elementos finitos para simulação em múltiplas escalas concorrentes / Fabiano Fernandes Bargos. – Campinas, SP : [s.n.], 2013.

Orientador: Marco Lúcio Bittencourt.
Tese (doutorado) – Universidade Estadual de Campinas, Faculdade de Engenharia Mecânica.

1. Métodos de simulação. 2. Multiescala. 3. Método dos elementos finitos. 4. Mecânica da fratura. 5. Dinâmica Molecular. I. Bittencourt, Marco Lúcio,1972-. II. Universidade Estadual de Campinas. Faculdade de Engenharia Mecânica. III. Título.

Informações para Biblioteca Digital

Título em inglês: Aspects of the discretized peridynamic theory and the finite element method for concurrent multiscale simulation
Palavras-chave em inglês:
Simulation Methods
Multscale
Finite Element Methods
Fracture Mechanics
Molecular Dynamics
Área de concentração: Mecânica dos Sólidos e Projeto Mecânico
Titulação: Doutor em Engenharia Mecânica
Banca examinadora:
Marco Lúcio Bittencourt [Orientador]
Renato Pavanello
Paulo Sollero
Sergio Persival Baroncini Proença
Caetano Rodrigues Miranda
Data de defesa: 28-02-2013
Programa de Pós-Graduação: Engenharia Mecânica

UNIVERSIDADE ESTADUAL DE CAMPINAS

FACULDADE DE ENGENHARIA MECÂNICA

COMISSÃO DE PÓS-GRADUAÇÃO EM ENGENHARIA MECÂNICA

DEPARTAMENTO DE PROJETO MECÂNICO

Ph.D THESIS

Aspects of the Discretized Peridynamic Theory and the Finite Element Method for Concurrent Multiscale Simulation

Aspectos da Teoria Peridinâmica Discretizada e do Método dos Elementos Finitos para Simulação em Múltiplas Escalas Concorrentes

Author: Fabiano Fernandes Bargos
Supervisor: Prof. Dr. Marco Lúcio Bittencourt

The following members of the Defense Committee have approved this Thesis:

Prof. Dr. Marco Lúcio Bittencourt, President
Instituição UNICAMP/FEM/DPM

Prof. Dr. Renato Pavanello
Instituição UNICAMP/FEM/DMC

Prof. Dr. Paulo Sollero
Instituição UNICAMP/FEM/DMC

Prof. Dr. Sergio Persival Baroncini Proença
Instituição USP/EESC/SET

Prof. Dr. Caetano Rodrigues Miranda
Instituição UFABC/CCNH

Campinas, 28 de fevereiro de 2013.

Acknowledgements

I would like to express my gratitude to:

Professor Marco Lúcio Bittencourt for all the opportunities and experiences that I had during these years at Unicamp.

Professor George Em Karniadakis for introducing me to the field of peridynamics during my stay at Brown University.

Dr. Michael L. Parks for hosting me at Sandia National Laboratories and for his guidance and help with peridynamics during the last one and a half year.

All my colleagues, friends now after six years, from Unicamp.

My wife for her support all these years especially during our time in the United States.

CAPES and CNPq for the indispensable financial support.

The art of living is to enjoy what we can see and not complain about what remains in the dark. When we are able to take the next step with the trust that we will have enough light for the step that follows, we can walk through life with joy and be surprised at how far we go.

Henri J. M. Nouwen "Bread for the Journey: A Daybook of Wisdom and Faith"

Resumo

Nesse trabalho, considera-se a simulação em múltiplas escalas concorrentes, usando a teoria peridinâmica e a elasticidade clássica, para a simulação de problemas de engenharia. Primeiramente a teoria peridinâmica em uma dimensão é estudada em detalhes com o foco na aplicação de condições de contorno de Dirichlet. Problemas de estado plano de tensão em chapas com e sem furo são considerados. É proposto um método de pós-processamento dos resultados de peridinâmica para o cálculo das tensões no material. Em seguida, a peridinâmica discretizada é acoplada ao método dos elementos finitos por meio de dois diferentes programas de computador, um especializado em peridinâmica e o outro em elementos finitos. A modelagem acoplada é usada para prever a formação e a propagação de uma trinca em uma chapa com furo. O fenômeno macroscópico de formação e propagação de trincas é resultado de processos físicos com origem na escala atomística. No entanto, as simulações existentes deste tipo problema são normalmente feitas com abordagens baseadas na teoria do contínuo, como a mecânica da fratura e o dano contínuo, que não consideram aspectos atomísticos do problema. A teoria peridinâmica é uma formulação da mecânica do contínuo em termos de equações integrais, permitindo a solução de problemas que apresentam descontinuidades. Na peridinâmica, trincas se propagam autonomamente como componentes naturais da deformação do material. Há um paralelo entre a formulação peridinâmica e a dinâmica molecular, um método atomístico. Em ambas as abordagens o movimento de uma partícula é encontrado através de um processo de somatório de forças devido às partículas vizinhas. No esquema de simulação em múltiplas escalas concorrentes aqui proposto, a peridinâmica é usada em pequenas porções do domínio onde a falha do material é esperada e a elasticidade clássica, usando o método dos elementos finitos, é utilizada no restante do domínio do problema. Os resultados mostram que a metodologia proposta para cálculo de tensões é satisfatória. A importância da correta imposição de condições de contorno de Dirichlet no domínio de peridinâmica também é destacado (este aspecto é de fundamental relevância para a abordagem acoplada, peridinâmica/elementos finitos). Finalmente, o padrão de propagação da trinca está de acordo com os resultados esperados.

Palavras-chave: Teoria Peridinâmica, Método dos Elementos Finitos, Mecânica da Fratura, Simulação em Múltiplas Escalas.

Abstract

We consider the peridynamic theory and the theory of classical elasticity for concurrent multiscale simulation of engineering problems. First the peridynamic theory in one dimension is studied in details focusing on the application of Dirichlet boundary conditions. Two-dimensional plane stress problems in plates with or without hole are considered. We propose a methodology to post-processing the peridynamics results in order to estimate stresses in the material. Then, the discretized peridynamics is coupled to finite elements by two different computer programs, one specialized in peridynamics and the other in finite elements. The coupled approach is used to estimate the crack formation and propagation in a plate with hole. The macroscopic phenomenon of crack formation and propagation is a result of physical processes with their origin in the atomistic scale. However, computer simulations of this type of problem are usually performed with continuum based approaches, such as fracture mechanics and continuum damage, which do not consider atomistic aspects of the problem. The peridynamic theory is a formulation of continuum mechanics in terms of integral equations allowing the solution of problems with discontinuities. In peridynamics cracks progress autonomously as natural consequence of the material deformation. There is a parallel between the peridynamic formulation and molecular dynamics, an atomistic method. In both approaches the motion of a particle is found by a process of summation of forces due to neighboring particles. In our concurrent multiscale scheme, peridynamics is used in small portions of the domain where material failure is expected and classical elasticity is used for modeling the rest of the problem domain. The results show that the proposed methodology for computing stresses is satisfactory. The importance of correctly imposing Dirichlet boundary conditions in the peridynamic domain is also highlighted (this aspect is of fundamental relevance for the coupled peridynamics/finite element approach). Finally, the pattern of the cracking agrees with the expected results.

Keywords: Peridynamic Theory, Finite Element Method, Fracture Mechanics, Multiscale Simulation.

LIST OF FIGURES

LIST OF TABLES

TABLE OF CONTENTS

1 INTRODUCTION

The knowledge about the behavior of materials in extreme loading conditions is critical to the advancements of a variety of applications in science and engineering. In the context of engineering, an ordinary practice is to design components and structures to certain limit of stresses. Occasionally, however, due to operating conditions and performance requirements, stresses and strains can reach values higher than the expected ones. For that reason, understanding material failure, mostly crack formation and propagation, is of great interest.

In terms of materials science and engineering, fracture is a macroscopic phenomenon with its origin in the atomistic scale. In general, crack formation and propagation in ductile and brittle materials also lie on small length scale phenomena, such as dislocations and voids formation. Mechanisms and features in materials that control their deformation behavior and their strength limit have been subject to studies in a variety of scientific and engineering disciplines. Physicists often consider the smallest lengthscales, featuring a few atoms and below. On the other hand, chemists considered the bonding between different atoms or the interactions of different chemical compounds and molecules. Engineers have mainly used continuum descriptions of materials, which is totally acceptable when dealing with larger structures that feature characteristic geometric dimensions much larger than the inhomogeneities of the material (BUEHLER, 2008).

Continuum and atomistic viewpoints provide two fundamentally different approaches in treating materials, with different appeal and significance for specific applications. For many applications, the two views are complementary and the joint use of both approaches can provide much insight into the behavior of materials. The atomistic models provide a fundamental description of material properties and processes resulting in a general description of matter, since the same atomistic model of a material may be suitable to study elasticity problems, as well as dissipative materials failure such as fracture (BUEHLER, 2008). On the other hand, the finite element method (FEM), is the most indicated when dealing with larger structures that feature characteristic geome-

tric dimensions much larger than the inhomogeneities of the material.

In the context of engineering applications, problems involving fracture have been traditionally modeled using tools based on continuum mechanics. Among different reasons, two should be pointed out. First, continuum based techniques such as the FEM are widely used in engineering, both in academia and industry (the FEM is highly robust in particular for determining stress fields and very suitable for modeling structures possessing complex geometries). And second, the atomistic based approaches are computationally expensive and extremely limited in time and length scales.

Fracture mechanics is the field in continuum mechanics that deals with the behavior of cracked bodies subjected to stresses and strains. Linear elastic fracture mechanics (LEFM) has been developed using a stress intensity factor, evaluated by the stress analysis, and expressed as a function of stress and crack size (ERDOGAN, 2000). Numerical techniques for modeling these problems have been proposed. The extended finite element method (XFEM), also known as the generalized finite element method (GFEM), is a technique that extends the classical FEM approach by enriching the solution space for approximations to differential equations with discontinuous functions (BELYTSCHKO *et al.*, 2009). Other techniques, such as the moving FEM, are also found in the literature (HAWKEN *et al.*, 1991). However, these special treatments are not always satisfactory, either physically or mathematically, in part because of the need for supplemental expressions to control crack growth.

Atomistic and molecular simulation is becoming increasingly important because these methods can overcome the difficulties encountered in the methods utilizing the classical continuum mechanics. Molecular dynamics (MD) is a computer technique that tracks the trajectories of molecules and atoms by numerically solving the Newton's equations of motion for a system of interacting particles, where forces between the particles, and potential energy, are defined. MD simulations may also be used to determine macroscopic thermodynamic properties of the system. By calculating the free energy density of an atomistic system for various deformation states one can estimate

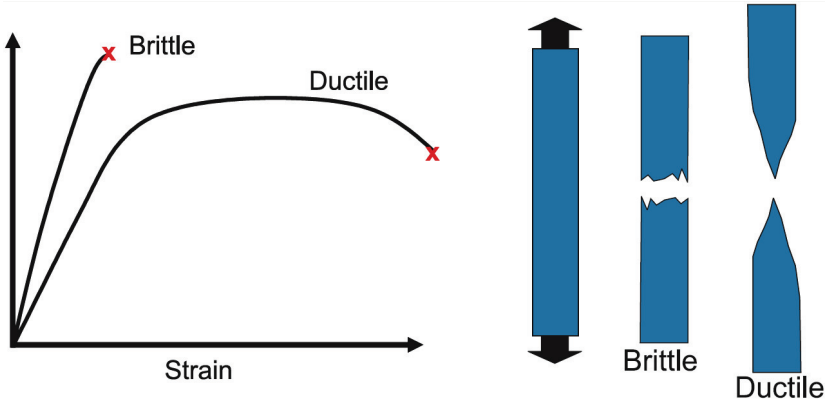

Figura 1.1: The plot shows simple, schematic stress-strain diagrams characteristic for a brittle and a ductile material. Similar curves are found for other materials, including polymers or rubber-like materials. The cross symbol ("x") indicates the point of material failure (BUEHLER, 2008).

the stress as well as the Young's modulus (GRIEBEL *et al.*, 2007). However, as pointed out before, time and length scales of this kind of approach are limited, usually in the order of picoseconds (10^{-12}s) and a few micrometers (10^{-6}m).

The link between atomistic models and the classical concept of elasticity used in continuum mechanics theories can be directly established by considering thermodynamics. In this sense, thermodynamics is the glue between atomistic methods - statistical mechanics - and continuum theories, linking microscopic states with a macroscale system (BUEHLER, 2008). In terms of thermodynamics, elastic regime is characterized by a reversible process. That is, all mechanical work done on the system is fully recoverable. In contrast, materials failure represents an irreversible process where only part of the mechanical work done on the system can be recovered, as energy was dissipated during processes associated with permanent deformation. Many investigations have been performed to explain fracture processes. Materials can fail in many ways. Brittle materials like glass shatters and quickly breaks into many small pieces. Ductile metals can be deformed permanently without breaking, with moderate resistance against the forces. Many biological tissues such as skin, or polymers and rubber are capable to sustain quite large deformation before they suddenly break. Figure 1.1 shows a schematic stress-strain curve, comparing a brittle and a ductile material.

As stated by Buehler (2008), research carried out over the last few decades revealed that the integration of different viewpoints of the matter, that is, those of physics, chemistry, and engineering is critical to make important breakthroughs to understand and improve the mechanical properties of materials.

Multiscale simulation is an approach that tries to take into account information at multiple spatial and (or) temporal scales. Traditional formulations couple MD based models to FE simulation. Problems with this kind of coupling stem from the fact that the wavelength emitted by the MD region is much smaller than what can be captured by the FE region. Since energy conservation is enforced, the wave is reflected back into the MD region leading to oscillatory solutions. When reducing the FE mesh to atomic dimensions, it is assumed that the FE mesh would be able to capture these high-frequency waves and allow them to pass through unimpeded, although other effects, such as differences in compliance between the two regions, will still cause some wave reflection. Different techniques have been proposed in order to mitigate this problem (WERNIK AND MEGUID, 2009).

Askari *et al.* (2008) claim that the onerous practical limitations of MD and the limited validity of classical elasticity have led to generalized continuum theories purporting to supply a single multiscale material model. Such theories are motivated by introducing a length-scale absent in classical elasticity. Recently, the peridynamic (PD) theory has been applied to multiscale simulation. The PD theory is a continuum mechanics formulation developed in terms of a integral operator that is not a function of the deformation gradient. It results in a more general notion of deformation and allows modeling problems involving discontinuities, such as cracking (SILLING, 2000).

An important work by Seleson *et al.* (2009) demonstrated that the PD model can be cast as an upscaling of MD. They showed that the solutions of MD simulations can be recovered by PD models. Thus, the PD model preserves characteristic properties of MD models lost by classical continuum mechanics. Furthemore, the resulting PD models can be solved more cheaply than the corresponding MD models because the PD models can be discretized on a mesh that is coarse with

respect to the atomistic lattice.

It is evident that PD theory is promising for linking different length scales. Furthermore, damage prediction in peridynamic theory is more realistic than the methods utilizing the classical continuum theory since the PD theory considers material failure as a part of the material response without resorting to any external damage criterion (KILIC, 2008). However, the PD theory is relatively new and requires more investigations.

The PD theory, and its application to multiscale simulation and its coupling with the FEM, will be discussed in Chapter 2.

1.1 Objectives and contributions

The general objective of this work is to develop concurrent multiscale simulations, using the PD theory and the FEM, focusing on the study of cracking formation and propagation.

We couple the open-source MD program LAMMPS to a FE library. The problem domain is divided into two subdomains. One part is modeled via classical elasticity and resolved using the FEM and the other part is discretized into PD points. Displacements (Dirichlet boundary conditions) are used for coupling the two parts of the domain. The communication between the two programs is performed via a wrapper program written in C++. This program is responsible to feed the two programs with boundary conditions during the simulation time. The FE input file indicates the overlapping region and routines in the wrapper code identify the PD nodes in this region.

In order to reach the general objective of this work, we systematically study some aspects of the PD theory, such as boundary conditions application, that are important when the discretized PD is coupled to the FEM.

Following are the points we consider to be the contributions of this work:

- Present a study of the one-dimensional PD stiffness matrix;
- Provide a discussion on nonlocal application of essential boundary conditions in PD;
- Study two-dimensional plane stress problems using PD in order to understand its convergence behavior before coupling PD-to-classical continuum;
- Propose a practical methodology for computing stresses in PD simulations;
- Develop a wrapper program for coupling two different programs for multiscale simulation. The developed codes permit new boundaries conditions for the overlapping layer (PD/FE) to be tested.

1.2 Organization of the text

Chapter 2 provides a brief review of the literature on multiscale modeling and explains the main approaches. A detailed review of the PD theory is also provided and different aspects of the theory are covered, such as mathematical development, material models and its application to real problems.

Chapter 3 provides the fundamentals of the bond-based PD theory and discuss the application of Dirichlet boundary conditions in an one-dimensional problem. The properties of the one-dimensional PD stiffness matrix is also discussed.

Chapter 4 focuses on the numerical solution of the PD equations using a dynamic relaxation technique with kinetic damping. Two-dimensional plates with or without hole are considered and the displacement fields are compared against FE results. Furthermore, a methodology for computing stresses for the PD solution is proposed.

Although the PD theory is promising for damage prediction, it is computationally more demanding than the FEM. Furthermore, the FEM is highly effective for modeling problems without damage and complex geometries. Hence, Chapter 5 presents the coupling between the discretized PD theory and the FEM to combine the advantages of both methods. The region involving failure is modeled using the PD theory while classical elasticity is applied to the regions without failure. The coupling introduces an overlap region in which both PD and classical elasticity equations are used. Using the displacements, a wrapper program links the two different programs used to solve the PD and the FE domains. Finally, we present the final remarks and suggestions for future work related to the PD theory in Chapter 6.

2 LITERATURE REVIEW

In the following, we provide a brief discussion on multiscale simulation. After that, we consider the PD theory, presenting some of its applications, and we also discuss some of the recent approaches for coupling peridynamics and classical elasticity.

2.1 Multiscale modeling

Multiscale modeling and simulation is the field of solving physical problems that have important features on multiple spatial and (or) temporal scales. Multiscale modeling can be broadly classified into two categories as *sequential* and *concurrent* multiscale methods. In sequential multiscale (or up-scaling procedure) macroscopic models are derived from the microscopic ones by averaging fine scale information and introducing it into coarse scale models in the form of constitutive relations (i.e., a homogenization approach). In concurrent methods (hybrid multi-scale models), two or more scales are combined in one model, making a microscopic zoom inside the macroscopic model (FISH *et al.*, 2007).

Disparity in the lengthscales between such coarse scale and fine scale phenomena can exceed 10^{10}. It is prohibitive in terms of computational cost to model coarse scale phenomena from fine scale models alone. Concurrent multiscale methods are an effective tool to handle such situations because, many times, localized areas of a problem domain need fine scale models to resolve the complicated fine scale processes while the rest of the problem domain can be modeled with a coarse scale model (FISH *et al.*, 2007).

Most of the work in concurrent modeling techniques is based on coupling molecular statics or molecular dynamics to a continuum model. In this case, a transition region is introduced to couple the different lengthscales associated with MD and the continuum as well as allow two way trans-

fer of the field variables of interest between these two regions. The literature contains numerous methods of concurrent coupling. Combined FE and atomistic models to study crack propagation in crystals (MULLINS AND DOKAINISH, 1982; KOHLHOFF *et al.*, 1991) are some of the earliest works of atomistic/continuum coupling. Fracture in nanomaterials by coupling quantum mechanics and continuum mechanics can be cited as one of the recent studies of concurrent multiscale modeling (XU *et al.*, 2012).

Pioneering approaches for multiscale methods are the quasi-continuum (QC) method (TADMOR *et al.*, 1996; MILLER AND TADMOR, 2002) and macroscopic, atomistic, ab initio dynamics (MAAD) (ABRAHAM *et al.*, 1998). Based on these techniques, various methods for multiscale modeling have been proposed such as coarse-grained molecular dynamics (CGMD) (RUDD AND BROUGHTON, 1998), bridging domain method (BDM) (XIAO AND BELYTSCHKO, 2004), and bridging scale method (BSM) (WAGNER AND LIU, 2003; PARK AND LIU, 2004).

Multiscale simulations considering PD for solving finer scales are recent, and will be presented later. As stated before, there is no limitation on time and length scales in PD, which makes the wave reflection phenomena less significative when using PD coupled to classical continuum theory for concurrent multiscale simulation. However, multiscale simulation is still an open problem, to which this project aims to contribute.

In the following section a brief review of multiscale modeling techniques is presented.

2.1.1 Macroscopic, Atomistic, Ab Initio Dynamics (MAAD)

A frequently cited reference in multiscale modeling is the Macroscopic, Atomistic, Ab-initio Dynamics (ABRAHAM *et al.*, 1998; BROUGHTON *et al.*, 1999) where crack propagation in silicon was simulated. The idea of this approach is to link three scales in a concurrent manner: Tight-binding (TB) quantum mechanics model to represent bond breaking at the crack tip, MD around

the crack tip to model processes such as dislocation loop formation and FE model farther away from the crack to capture macroscopic deformation. The interactions among three scales are taken into account by the total Hamiltonian of the system. A very thin "handshake" region is used to couple domains with each other. FE mesh is graded down to the atomic size for the reduction of wave reflection between MD and FE. However, this attempt of connecting MD and continuum mechanics using the atomic scale mesh size for FE has two problems: one numerical and one physical. The numerical issue is that simulation time of FE slows down to picosecond because the time step is governed by the element size (BATHE, 1996). The physical issue is that atomic scale FE simulation is physically unreasonable because constitutive equation of FE is based on continuum mechanics. Due to the assumption of a continuous and differentiable mass density, the atomic scale FE mesh makes this assumption invalid. Moreover, although (Abraham *et al.* (1998)) mentioned that there is no visible reflection at the FE-MD handshake region, they did not discuss the high frequency wave in the MD region. The reflection of high frequency wave at the interface between the MD and FE region still exists because atoms on the FE mesh side are stationary while atoms on the MD side are mobile (XIAO AND BELYTSCHKO, 2004).

2.1.2 Quasi-Continuum (QC) Method

The quasi-continuum method (TADMOR *et al.*, 1996; MILLER AND TADMOR, 2002) is based on an entirely atomistic description of the material. The method resolves the regions close to defects, such as dislocations, grain boundary, etc. with MD, while farther away from the defect region atoms are constrained to move in groups by the FE shape functions and mesh, thereby greatly reducing the degrees of freedom in the problem (FISH *et al.*, 2007). Finite-temperature quasicontinuum (DUPUY *et al.*, 2005) is developed as a coarse-grained alternative to MD for crystalline solids at constant temperature by using a combination of statistical mechanics and FE interpolation functions.

Although QC method suggested new approaches for a multiscale modeling, this method suf-

fers from the same issues of MAAD, i.e., elastic wave reflection in MD region and the total simulation time limit, dominated by the time step of MD, which is very short for any engineering application.

2.1.3 Coarse-Grained Molecular Dynamics (CGMD)

Coarse-grained molecular dynamics (RUDD AND BROUGHTON, 1998) uses a coarse graining procedure based on statistical mechanics to derive equations of motion for a FE mesh from the equations of motion of MD. A key idea of the method is that degrees of freedom are eliminated by using the coarse-graining approximation, that converges to the exact atomic energy, to reduce the computational cost.

Similar to MAAD, mesh size of CGMD is graded down to atomic scale in the MD region, and coarsened far from the MD region. Thus, CGMD also experiences the same issues as MAAD, such as time step limitation, the wave reflection, and the total simulation time. Additional terms are introduced in the equation of motion to reduce spurious wave reflection. It leads to additional force calculations in MD simulation which already suffers from the limited simulation time due to the computational cost. Considering that the most expensive part of MD simulation is force calculations, it is the critical limitation of the method.

2.1.4 Bridging Domain Method (BDM)

The bridging domain method (XIAO AND BELYTSCHKO, 2004) has been used to couple continuum to atomistics through an overlap region and study shock wave propagation from molecular region to the continuum region. In this approach, the system consists of three domains: molecular dynamics, continuum mechanics, and handshake region. The main idea of the model

is using a linear combination of the Hamiltonian on the handshake region. Lagrange multipliers method is applied to enforce displacement compatibility in the overlapping region between MD and continuum regions. The energy within the overlapping region goes from entirely atomistic at MD boundary to entirely continuum at FE boundary. The effect of this energy transition is that high-frequency atomic scale energy is filtered. The idea of spatial filtering is proven by the numerical examples in (XIAO AND BELYTSCHKO, 2004). A minimum overlapping distance is required for the method to eliminate high-frequency waves effectively. The minimum overlapping distance makes drawbacks such as increasing the computational cost and decreasing the MD area.

2.1.5 Bridging Scale Method (BSM)

The bridging scale method was developed by Wagner and Liu (2003) and Park and Liu (2004) where the solution is decomposed into fine and coarse scale parts and a projection operator is used to decouple the kinetic energy of the atomistic and the continuum sub-domains. BSM starts from an entire molecular system. To save computational time the system area of MD is reduced from the entire region to a small area of interest.

This approach does not grade down to the FE mesh size to the atomic size, and provides different simulation time scales on both MD and FE. Comparing the BSM to the other multiscale methods (CGMD, MAAD), one clear advantage of this approach is that FE models the entire domain, and is not graded down to the atomic scale. The result is that larger time step used in FE is not restricted by the atomic sized elements in the mesh allowing time-staggered integration schemes to be used (SYMEONIDIS AND KARNIADAKIS, 2006). Thus, the coarse scale variables can evolve on an appropriate time scale, while the fine scale variables can evolve (appropriately) on a much smaller time scale. However, additional force term is introduced to the MD model. When the computational limitation of MD is considered, the calculation of additional force can be a significant disadvantage on multiscale modeling.

2.2 The peridynamic theory

The PD theory is a promising formulation of continuum mechanics introduced in (SILLING, 2000). As opposed to classical elasticity, PD is a nonlocal theory (BAŽANT AND JIRÁSEK, 2002) where particles interact with each other across a finite distance, as in molecular dynamics. It is assumed that the interaction between particles vanishes whenever the particles are separated by a distance (in the undeformed configuration) larger than a certain defined value called horizon. In PD, cracks initiate and propagate naturally based on the deformation of the material. This is opposed to classical continuum based techniques, such as LEFM (linear elastic fracture mechanics), where the initial position of the crack is required to be known in advance (ERDOGAN, 2000).

Peridynamics is an alternative theory of solid mechanics which formulates problems in terms of integral equations rather than partial differential equations. Damage is incorporated at the level of the two-particle interactions, so crack localization and fracture occur as a natural outgrowth of the equation of motion and constitutive models (SILLING AND ASKARI, 2005). There is no supplemental relation that dictates crack growth. In particular, the stress intensity factor is not used (SILLING AND LEHOUCQ, 2010). In addition, the PD approach is a continuum theory. This means that individual atoms need not be modeled, and that a true, physically correct, interatomic potential need not be known (SILLING, 2000). It is possible to show that the PD theory converges to the classical elasticity at the limit of small horizons (SILLING AND LEHOUCQ, 2008).

In addition, there is an obvious parallel between the PD theory and MD computations, since in both approaches the motion of any particle is found by a process of summation of forces due to neighboring particles (SILLING, 2000). Seleson *et al.* (2009) considered the PD theory as an upscaling of MD showing that the same dynamics of a MD simulation for a Lennard-Jones potential was recovered by a PD model. Despite this, an important difference is that MD particles have no memory of their position in any reference configuration whereas PD ones can have.

2.2.1 Theoretical foundation

The term peridynamic was proposed in (SILLING, 2000) from the Greek roots for *near* and *force*. Nowadays the initially proposed theory is known as *bond-based* because it uses a two-particle force function (bond) to describe the interaction between material particles. In the bond-based theory, the pairwise force function contains all the constitutive information about the material. One of the difficulties that occurs with this approach is that, in many cases, it is an oversimplification to assume that any pair of particles interacts only through a central potential that is totally independent of all other local conditions. This assumption implies (for an isotropic, linear, microelastic material) in an effective Poisson's ratio of $1/4$ for three-dimensional simulations (and $1/3$ for two-dimensional).

This difficulty motivated a rethinking of the whole PD theory resulting in a generalization of the original theoretical framework (SILLING *et al.*, 2007). The outcome was a concept which preserves the idea of bonds carrying forces between pairs of particles. However, in the new approach, the forces within each bond are not determined independently of each other. This generalization permits the response of a material at a point to depend collectively on the deformation (and possibly the rate of deformation and history) of all bonds connected to the point. The material-dependent part of the PD model was rewritten by introducing a mathematical object called *force state* that is in some ways similar to the traditional stress tensor of the classical continuum mechanics. It was shown that by using this concept, the basic PD theory can be generalized to include materials with any Poisson's ratio. Also, because of the similarity to stress tensors, it is possible to apply constitutive models in the classical theory directly in the PD theory. This generalized version of the peridynamics is called *state-based* theory, as opposed to the bond-based.

Peridynamics reformulates the basic equations of motion in such a way that the internal forces are evaluated through an integral formulation that does not require the evaluation of a stress tensor field or its spatial derivatives. In (LEHOUCQ AND SILLING, 2008), a notion of a PD stress tensor,

derived from nonlocal interactions, is defined via an abstract variational formulation. At any point in the body, this stress tensor is obtained from the forces within PD bonds that go geometrically through the point. The PD equation of motion can be expressed in terms of this stress tensor resulting in a partial differential equation (PDE) that is formally identical to the classical equation of motion.

The recent survey (SILLING AND LEHOUCQ, 2010) considers the mechanical aspects of the PD continuum theory. This includes proposing the PD balance of energy and thermodynamic restrictions so that the second law of thermodynamics is not violated. Lehoucq and Sears (2011) provide a statistical mechanical foundation for PD deriving the energy and momentum balance laws for the PD formulation. The nonlocality of force interaction is intrinsic and originates in molecular force interaction that is nonlocal.

More recently, rigorous mathematical analysis of the PD models has also received much attention. Emmrich and Weckner (2007a), Emmrich and Weckner (2007b), Zhou and Du (2010) and Du and Zhou (2011) establish various existence and uniqueness results for the linear PD balance of momentum. These papers also draw equivalences with the weak solution of the classical equations of linear elasticity, and show well-posedness of the PD equations in the limit as the nonlocality vanishes. In particular, the limiting solution for both stationary and time-dependent PD models coincides with the conventional weak solution given sufficient regularity of the boundary data and material properties (SILLING, 2000).

2.2.2 Material models

The prototype microelastic brittle (PMB) material model is the constitutive model that naturally results from the initially proposed PD theory when the breakage of bonds stretched beyond a certain limit is allowed (SILLING, 2000). This is a typical behavior of brittle fracture in which no apparent plastic deformation takes place before fracture. After breakage, the bond is unable to bear

loading and remains broken. The elastic properties of the PMB model are determined by the bulk modulus and the horizon.

Silling and Bobaru (2005) introduced a new constitutive model for modeling tearing and stretching of rubber materials. Problems such as bursting of a balloon and large deformation of a network of fibers were studied with the new material model. An oscillatory crack path, when a blunt tool was forced through a membrane, was also predicted.

Within the context of the state-based theory the linear peridynamic solid (LPS) was defined. This model is a nonlocal analogue to a classical linear elastic isotropic material. The elastic properties of a classical linear elastic isotropic material are characterized by two properties, the bulk and shear moduli. For the LPS model, the elastic properties are analogously determined by the bulk and shear moduli, along with the horizon (SILLING *et al.*, 2007). It can be shown that the PMB model is a special case of the LPS model (SELESON AND PARKS, 2011).

Kilic (2008) introduced a new PD material model to include thermo-mechanical loadings. The derivation of the material model is based on equating the strain energy density of the classical continuum theory to its corresponding energy in PD theory under thermo-mechanical loading. Various benchmark problems subjected to mechanical loadings were analyzed. The validity of the predictions using the new PD material model is established with the comparison against FE results for both small and large deformations.

In (FOSTER *et al.*, 2010), a rate-dependent plastic material model within the state-based PD framework was proposed. To validate the numerical implementation of the constitutive model, a set of impact tests were conducted. Numerical results for Taylor impact (normal impact of a cylindrical rod against a smooth flat rigid target) match the experimental data. The results suggest the viability of using PD to model materials that exhibit viscoplasticity with hardening.

However, as pointed in (SILLING, 2000), not all conventional elastic materials can be mode-

led with the PD approach. But for those that can, there may be an infinite number of PD materials corresponding to the same conventional material. All the existing PD microelastic materials have a corresponding conventional elastic material (in the sense of homogeneous deformations). There is a connection between the macroelastic energy density and strain energy density of conventional elasticity. The connection is that they both represent stored energy accumulated through deformation, and this energy is recoverable by reversing the deformation.

The number of PD material models already proposed is limited, as the PD theory is a recent formulation that needs more development.

2.2.3 Applications

The PD theory has been successfully applied to damage prediction of many practical problems. Damage is incorporated into PD by causing the bonds between interacting nodes to break irreversibly. Although this breakage occurs independently among all bonds, their failure tends to organize itself along two dimensional surfaces that are interpreted as cracks. Cracks progress autonomously, their advance is determined only by the field equations and constitutive model at the bond level.

Silling (2003) considered the Kalthoff-Winkler experiment in which a plate having two parallel notches is hit by an impactor. PD simulations successfully captured the angle of crack growth that is observed in the experiments. In (SILLING AND ASKARI, 2005), a numerical method for solving dynamic problems within the PD theory was described and a plate with a center crack was considered in order to discuss numerical convergence, accuracy and stability.

Force interactions resulting from discretizing PD are similar to traditional MD forces. Thus, with minor modifications, a MD code can perform PD calculations. Parks *et al.* (2008b) implemented PD within the MD code LAMMPS (PLIMPTON, 1995), an open-source, general purpose,

massively parallel MD simulator. The PD extensions made to the LAMMPS MD package are available for download from the LAMMPS WWW Site (http://lammps.sandia.gov). Askari *et al.* (2008) reviewed some multiscale applications of PD within engineering analyses, such as trans-granular and inter-granular crack propagation in polycrystalline ceramics, obtained with the PD module in LAMMPS.

In (BOBARU AND DUANGPANYA, 2012), the PD formulation for heat transfer in one-dimension, presented in (BOBARU AND DUANGPANYA, 2010), is extended for multiple dimensions. The PD heat flux is defined and it is proposed how to connect the micro-level PD parameters to the thermal conductivity of the material. The formulation is applied to transient heat conduction in bodies with evolving discontinuities, such as insulated cracks. Heat flow problems in a body in which insulated cracks dynamically grow, intersect, and thus alter the heat flow patterns was solved with the new formulation.

2.2.4 Coupling peridynamics/classical elasticity

As solving the discretized PD equation is computationally expensive compared to FE, concurrent coupling methods between PD and classical local models have appeared in the literature. Macek and Silling (2007) used standard truss elements available in the ABAQUS (commercial FE software) to represent PD bonds. These PD elements were applied in part of the problem domain and a FE mesh with standard elements in the remainder. The conventional FE mesh is coupled with the PD truss mesh using the embedded element feature also available in ABAQUS. The resulting FE model of the PD equations was applied to penetration problems. The FE implementation of PD is especially useful in penetration modeling because it avoids many of the difficulties in describing the interface between a penetrator and a target when using conventional FE.

Agwai *et al.* (2009) and Oterkus (2010) employed the submodeling approach to couple classical elasticity with PD. In their approach, the global analysis by means of FE is performed first,

and then PD is used for submodeling. In (AGWAI *et al.*, 2009), damage prediction and failure propagation for an electronic package drop test was performed. The global model, in which failure is not monitored, is simulated using FE. The submodel is created using the PD theory, damage initiation and propagation are monitored. The PD submodel simulation predicts failure initiation and growth in the expected region. The formulation in (OTERKUS, 2010) was used for modeling three-dimensional damage growth in composite structures. The methodology was capable of assessing the durability of complex composite structures and, when compared against the experimental observations, it captured the correct failure behavior.

Liu and Hong (2012) introduced a coupling approach of the discretized PD with FE. Different from the approach in (AGWAI *et al.*, 2009) and (OTERKUS, 2010), implementing a PD model in the framework of submodeling approach, the PD subregion is directly coupled to the FE subregion in this approach. An interface element is introduced to calculate coupling forces instead of using overlapping regions to couple PD and FE subregions. The scheme is used to simulate mixed mode fracture in a concrete specimen subjected to quasi-static loading. The region where failure is expected is modeled using PD, and the remaining region is modeled using conventional FE. Numerical predictions of crack patterns are close to the experimental observations.

A one-dimensional continuum formulation is proposed in (SELESON *et al.*, 2012) for the coupled system, PD-classical elasticity. They derive a coupling starting from a single framework and derive a blended model at the level of the equations of motion, avoiding undesired spurious effects on the boundaries. The novel result is that, in contrast to classical blending methods where two or more models are joined together, they derive a coupled nonlocal/local scheme from a single framework. It is shown that the error can be controlled by the sizes of the nonlocal region and the transition region.

Works on multiscale simulations considering PD for solving finer scales are recent and testing different techniques for coupling is of fundamental importance. However, multiscale simulation is still an open problem, to which this work aims to contribute. For example, the computational tools

developed during this work will allow us to test new boundary conditions on the interface PD/FE. Domain decomposition techniques such as Dirichlet-Neumann, Neumann-Neumann and the Robin mixed condition method (that has been successfully applied to fluid structure interaction problems BADIA *et al.*, 2008) can be tested.

3 PERIDYNAMIC MODEL

The proposed PD continuum theory (SILLING, 2000) makes minimal regularity assumptions on the deformation. Instead of spatial differential operators, integration over differences of the displacement field is used to describe the existing, possibly nonlinear, forces between particles of the solid body. As it was presented in the Chapter 2, the theoretical foundation of the PD was established in (SILLING, 2000 and SILLING *et al.*, 2007). Partially following the notation in (ASKARI *et al.*, 2008), the resulting derivative-free nonlocal PD equation of motion reads

$$\rho(x)\ddot{\mathbf{u}}(\mathbf{x},t) = \int_{\mathcal{H}_x} \mathbf{f}(\mathbf{u}(\mathbf{x}',t) - \mathbf{u}(\mathbf{x},t), \mathbf{x}' - \mathbf{x})\mathrm{dV}_{\mathbf{x}'} + \mathbf{b}(\mathbf{x},t), \tag{3.1}$$

where $\mathcal{H}_x$ is a spherical neighborhood of $\mathbf{x} \in \mathcal{R}$ with radius δ called peridynamic horizon (Figure 3.1), $\mathbf{u}$ is the displacement vector field, $\mathbf{b}$ is the prescribed body force density field, ρ is the mass density in the reference configuration, and the integral, in the right hand side, expresses that the internal force density at $\mathbf{x}$ is the summation of forces over all vectors $\mathbf{x}' - \mathbf{x}$ ($\mathbf{f}$ will be latter discussed). Beyond the PD horizon δ we have

$$\mathbf{f}(\mathbf{u}(\mathbf{x}',t) - \mathbf{u}(\mathbf{x},t), \mathbf{x}' - \mathbf{x}) = 0, \quad \mathbf{x}' \notin \mathcal{H}_x. \tag{3.2}$$

The spatial point $\mathbf{y}$ (in the deformed configuration) is related to the material point $\mathbf{x}$ (in the reference configuration) via $\mathbf{y}(\mathbf{x},t) = \mathbf{x} + \mathbf{u}(\mathbf{x},t)$ where $\mathbf{u}(\mathbf{x},t)$ is the displacement of $\mathbf{x} \in \mathcal{R} \subset \mathbb{R}^3$. Deformation represents the mechanism through which continuum mechanics relates strain to the internal forces of a body. Classical elasticity assumes that the displacement field is continuously differentiable at every $\mathbf{x} \in \mathcal{R}$ so that

$$\mathbf{u}(\mathbf{x}',t) - \mathbf{u}(\mathbf{x},t) = \nabla_{\mathbf{x}}\mathbf{u}(\mathbf{x},t)(\mathbf{x}' - \mathbf{x}) + O(\|\mathbf{x}' - \mathbf{x}\|^2), \tag{3.3}$$

where $\nabla_{\mathbf{x}}$ denotes the gradient operator with respect to the material point $\mathbf{x}$. If

$$\mathbf{F} := \mathbf{I} + \nabla_{\mathbf{x}}\mathbf{u}(\mathbf{x}, t) \tag{3.4}$$

denotes the deformation gradient tensor, then

$$\mathbf{y}(\mathbf{x}', t) - \mathbf{y}(\mathbf{x}, t) \approx \mathbf{F}(\mathbf{x}, t)(\mathbf{x}' - \mathbf{x}). \tag{3.5}$$

In words, the body deformation $\mathbf{y}(\mathbf{x}', t) - \mathbf{y}(\mathbf{x}, t)$ can be approximated by the deformation gradient

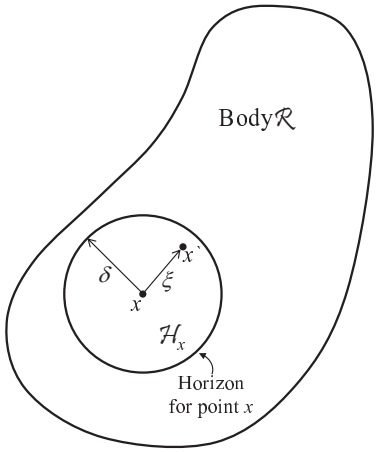

Figura 3.1: Each point x in the body interacts directly with points in the sphere $\mathcal{H}_x$ through *bonds*.

tensor acting on the bond $\mathbf{x}' - \mathbf{x}$. By relying on the true deformation $\mathbf{y}(\mathbf{x}', t) - \mathbf{y}(\mathbf{x}, t)$ (and not on the deformation gradient), PD avoids assumptions on the smoothness of the displacement field, in contrast to the classical elasticity.

This chapter is organized as follows. First, a bond-based model is demonstrated in Section 3.1, where the focus lies on the pairwise force function $\mathbf{f}$. Afterwards, we describe the numerical discretization of the PD equation for a two-dimensional domain in Section 3.2 and obtain the stiffness matrix for a PD discretization in Section 3.3. Finally, in Section 3.4, we solve a one-dimensional static problem and discuss the nonlocal application of Dirichlet boundary conditions in PD.

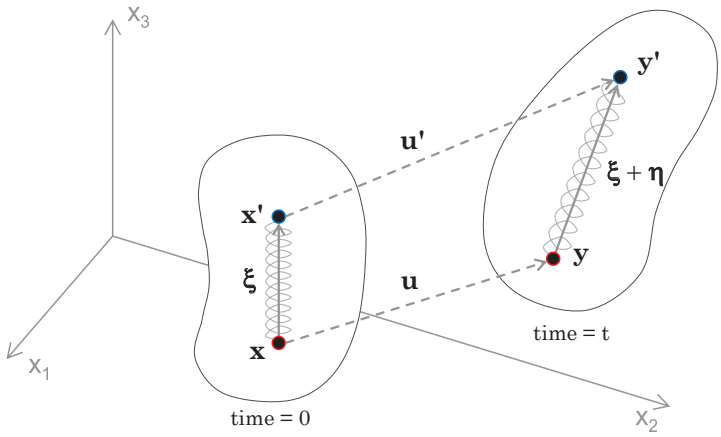

Figura 3.2: Notation for the bond-based model.

3.1 Bond-based model

In the bond-based model, the kernel $\mathbf{f}$ of equation (3.1) is a *pairwise force function* whose value is the force vector (per unit volume squared) that the particle $\mathbf{x}'$ exerts on the particle $\mathbf{x}$. The relative position of these two particles in the reference configuration is given by $\boldsymbol{\xi}$ and their relative displacement by $\boldsymbol{\eta}$:

$$\boldsymbol{\xi} = \mathbf{x}' - \mathbf{x}, \quad \boldsymbol{\eta} = \mathbf{u}(\mathbf{x}', t) - \mathbf{u}(\mathbf{x}, t), \tag{3.6}$$

Using these definitions, $\boldsymbol{\xi} + \boldsymbol{\eta}$ represents the current relative position vector between the particles (Figure 3.2). The direct physical interaction between the particles, defined by the pairwise force function, is called bond.

A material is called microelastic if there exists a so-called pairwise scalar micropotential w such that

$$\mathbf{f}(\boldsymbol{\eta}, \boldsymbol{\xi}) = \frac{\partial w}{\partial \boldsymbol{\eta}}(\boldsymbol{\eta}, \boldsymbol{\xi}), \quad \forall \boldsymbol{\eta}, \boldsymbol{\xi}. \tag{3.7}$$

The micropotential is the strain energy in a single bond and has dimensions of energy per unit volume squared. One of the simplest models that has been suggested is the proportional microelastic

material model with

$$\mathbf{f}(\boldsymbol{\eta}, \boldsymbol{\xi}) = c_{d,\delta} s(\boldsymbol{\eta}, \boldsymbol{\xi}) \frac{\boldsymbol{\xi} + \boldsymbol{\eta}}{\|\boldsymbol{\xi} + \boldsymbol{\eta}\|}, \tag{3.8}$$

where

$$s(\boldsymbol{\eta}, \boldsymbol{\xi}) = \frac{\|\boldsymbol{\xi} + \boldsymbol{\eta}\| - \|\boldsymbol{\xi}\|}{\|\boldsymbol{\xi}\|}, \tag{3.9}$$

denotes the bond stretch, that is the relative change of the length of a bond [1]. The subscript d is the dimension of the problem domain and by $\|\cdot\|$ we denote the Euclidean norm. The constants of proportionality $c_{d,\delta}$, computed using the elastic energy density of classical theory (see BOBARU *et al.*, 2009 for other examples), are (SELESON AND PARKS, 2011)

$$c_{1,\delta} = \frac{18K}{5\delta^2}, \quad c_{2,\delta} = \frac{72K}{5\pi\delta^3}, \quad c_{3,\delta} = \frac{18K}{\pi\delta^4}, \tag{3.10}$$

with the bulk modulus K, the Young's modulus E and the Poisson's ratio ν related by

$$K = \frac{E}{3(1-2\nu)}. \tag{3.11}$$

The term $c_{d,\delta}/\|\boldsymbol{\xi} + \boldsymbol{\eta}\| > 0$ is the stiffness per unit volume squared. For such a material, the magnitude of the force in a bond varies linearly with its bond stretch.

In the case of the pairwise force function defined by equation (3.8), the related micropotential is given by

$$w(\boldsymbol{\eta}, \boldsymbol{\xi}) = \frac{c_{d,\delta} s^2(\boldsymbol{\eta}, \boldsymbol{\xi})}{2}, \tag{3.12}$$

where the micropotential was chosen such that $w(0, \boldsymbol{\xi}) = 0$.

In order to model cracks and simulate fracture, damage is incorporated into a PD constitutive model by allowing the bonds for solid interactions to break irreversibly. The simplest assumption

[1] Equations (3.8) and (3.9) are frequently represented in terms of the spatial $\mathbf{y}$ and material $\mathbf{x}$ coordinates

$$\mathbf{f}(\mathbf{y}' - \mathbf{y}, \mathbf{x}' - \mathbf{x}) = cs \frac{\mathbf{y}' - \mathbf{y}}{\|\mathbf{y}' - \mathbf{y}\|}, \quad s = \frac{\|\mathbf{y}' - \mathbf{y}\| - \|\mathbf{x}' - \mathbf{x}\|}{\|\mathbf{x}' - \mathbf{x}\|}.$$

is that this breakage occurs when a bond is extended beyond some predetermined critical bond deformed length. This is realized by multiplying the pairwise force function (3.8) by the function

$$\mu(\boldsymbol{\xi}, \boldsymbol{\eta}, t) = \begin{cases} 1 & \text{if} \quad s(\boldsymbol{\xi}, \mathbf{u}(\mathbf{x}', \tau) - \mathbf{u}(\mathbf{x}, \tau)) \leq s_0 \quad \forall \tau \leq t \\ 0 & \text{otherwise,} \end{cases} \tag{3.13}$$

for some critical bond stretch s_0 for breakage. Note that the resulting pairwise force function now explicitly depends on time t.

3.2 Numerical method

The region is discretized into nodes, each with a known volume in the reference configuration. Taken together, the nodes form a grid (Figure 3.3). Let $\mathbf{x}_1, \ldots, \mathbf{x}_n$ be distinct points in $\mathcal{R}$, where $\mathcal{R} = \bigcup_{i=1}^{n} \Omega_i$ and $\mathbf{x}_i \in \Omega_i \subset \mathcal{H}(\mathbf{x}_i)$. The spatial discretization of (3.1) results in

$$\rho(\mathbf{x}_i)\ddot{\mathbf{u}}(\mathbf{x}_i, t) = \sum_{j \neq i} \mathbf{f}(\mathbf{u}(\mathbf{x}_j, t) - \mathbf{u}(\mathbf{x}_i, t), \mathbf{x}_j - \mathbf{x}_i)\mathrm{V}_j + \mathbf{b}(\mathbf{x}_i, t), \quad i = 1, \ldots, n, \tag{3.14}$$

where V_j is the volume of Ω_j. Note that the sum is not over $n - 1$ but rather over the number of $\mathbf{x}_j \in \mathcal{H}(\mathbf{x}_i)$.

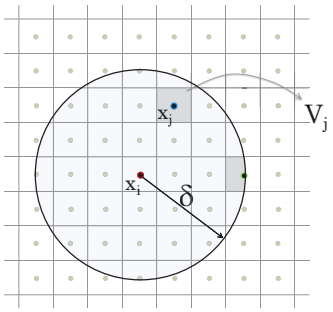

Figura 3.3: Two-dimensional diagram showing particles on a mesh (grid) with neighborhood $\mathcal{H}_x$ defined by the circular region with radius δ (horizon). The straight vertical and horizontal lines define the boundaries of each particle. The two highlighted particles, with its volume shaded by gray, are used to show that the volume associated with particles near the boundary of the horizon is not completely contained within the horizon.

Integration of the interaction force term is still an open question. It may play an important role in the numerical implementation of the PD theory as it is discussed in (YU, 2011).

3.3 One-dimensional peridynamic stiffness matrix

In this section we explicitly show that the discretization of the PD equation results in a linear system in the form $[K]\{u\} = \{f\}$, where $[K]$ is the PD stiffness matrix, $\{u\}$ the displacement vector and $\{f\}$ the load term. Let us consider a domain $\Omega = (0, L)$ divided into $N_x - 1$ uniform intervals of size Δx, so that we obtain a uniform mesh with N_x evenly-spaced nodes. We then assume that each node represents a "cell" of length Δx. Given the node distribution $x_i, i = 1, 2, ..., N_x$ over the length of a one-dimensional bar, we discretize Equation (3.1) at all points x_i.

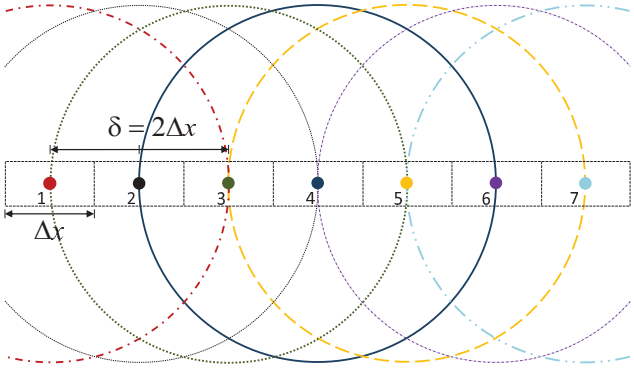

Figura 3.4: The peridynamic discrete form of a finite length one-dimensional bar.

In this particular case we use seven nodes to discretize the bar with the PD horizon $\delta = 2\Delta x$ (Figure 3.4) (note that the horizons of nodes away from the ends cover exactly five nodes). For $K = 5\delta^2/18$ the constant of proportionality is $c_{1,\delta} = 1$ (Equation 3.10). Thus, the resulting system

of equations for a static example (considering $\mathbf{b} = 0$)

$$\begin{aligned}
-\tfrac{1}{\|x_2-x_1\|}V(u_2-u_1) - \tfrac{1}{\|x_3-x_1\|}\tfrac{V}{2}(u_3-u_1) &= 0\\
-\tfrac{1}{\|x_1-x_2\|}V(u_1-u_2) - \tfrac{1}{\|x_3-x_2\|}V(u_3-u_2) - \tfrac{1}{\|x_4-x_2\|}\tfrac{V}{2}(u_4-u_2) &= 0\\
-\tfrac{1}{\|x_1-x_3\|}\tfrac{V}{2}(u_1-u_3) - \tfrac{1}{\|x_2-x_3\|}V(u_2-u_3) - \tfrac{1}{\|x_4-x_3\|}V(u_4-u_3) - \tfrac{1}{\|x_5-x_3\|}\tfrac{V}{2}(u_5-u_3) &= 0\\
-\tfrac{1}{\|x_2-x_4\|}\tfrac{V}{2}(u_2-u_4) - \tfrac{1}{\|x_3-x_4\|}V(u_3-u_4) - \tfrac{1}{\|x_5-x_4\|}V(u_5-u_4) - \tfrac{1}{\|x_6-x_4\|}\tfrac{V}{2}(u_6-u_4) &= 0\ ,\\
-\tfrac{1}{\|x_3-x_5\|}\tfrac{V}{2}(u_3-u_5) - \tfrac{1}{\|x_4-x_5\|}V(u_4-u_5) - \tfrac{1}{\|x_6-x_5\|}V(u_6-u_5) - \tfrac{1}{\|x_6-x_5\|}\tfrac{V}{2}(u_6-u_5) &= 0\\
-\tfrac{1}{\|x_4-x_6\|}\tfrac{V}{2}(u_4-u_6) - \tfrac{1}{\|x_5-x_6\|}V(u_5-u_6) - \tfrac{1}{\|x_7-x_6\|}V(u_7-u_6) &= 0\\
-\tfrac{1}{\|x_6-x_7\|}V(u_6-u_7) - \tfrac{1}{\|x_5-x_7\|}\tfrac{V}{2}(u_5-u_7) &= 0
\end{aligned}$$

using $\Delta x = 1$ and the "volume" $V = 1$ we obtain

$$\begin{aligned}
-u_2 + u_1 - \tfrac{1}{4}(u_3-u_1) &= 0\\
-u_1 + 2u_2 - u_3 - \tfrac{1}{4}(u_4-u_2) &= 0\\
-\tfrac{1}{4}(u_1-u_3) - u_2 - 2u_3 - u_4 - \tfrac{1}{4}(u_5-u_3) &= 0\\
-\tfrac{1}{4}(u_2-u_4) - u_3 - 2u_4 - u_5 - \tfrac{1}{4}(u_6-u_4) &= 0\ .\\
-\tfrac{1}{4}(u_3-u_5) - u_4 - 2u_5 - u_6 - \tfrac{1}{4}(u_6-u_5) &= 0\\
-\tfrac{1}{4}(u_4-u_6) - u_5 - 2u_6 - u_7 &= 0\\
-u_6 + u_7 - \tfrac{1}{4}(u_5-u_7) &= 0
\end{aligned} \tag{3.15}$$

Rewriting the above equations in matrix-vector form

$$\begin{bmatrix}
\frac{5}{4} & -1 & -\frac{1}{4} & & & & \\
-1 & \frac{9}{4} & -1 & -\frac{1}{4} & & & \\
-\frac{1}{4} & -1 & \frac{5}{2} & -1 & -\frac{1}{4} & & \\
 & -\frac{1}{4} & -1 & \frac{5}{2} & -1 & -\frac{1}{4} & \\
 & & -\frac{1}{4} & -1 & \frac{5}{2} & -1 & -\frac{1}{4}\\
 & & & -\frac{1}{4} & -1 & \frac{9}{4} & -1\\
 & & & & -\frac{1}{4} & -1 & \frac{5}{4}
\end{bmatrix}
\begin{Bmatrix} u_1\\ u_2\\ u_3\\ u_4\\ u_5\\ u_6\\ u_7 \end{Bmatrix} =
\begin{Bmatrix} 0\\ 0\\ 0\\ 0\\ 0\\ 0\\ 0 \end{Bmatrix}. \tag{3.16}$$

Note that the PD stiffness matrix $[K]$ is a band matrix with number of non-zero sub-diagonals given by the horizon δ. The row sums are all zero showing that the matrix is singular (rigid body mode), which is correct in the absence of boundary conditions. Also note that the stiffness matrix is symmetric positive semidefinite. If a prescribed displacement is imposed to system, we can solve for the nodal displacements of the unconstrained points. The boundary conditions are non-locally applied on a layer of size $2\Delta x$, which is the same size of the PD horizon δ, at the ends of the bar. For this example, the prescribed displacements are $u_1 = 0.0, u_2 = 0.1, u_3 = 0.5$ and $u_4 = 0.0$. After applying the boundary conditions, the PD stiffness matrix become positive definite and the system of equations to be solved is given by

$$\begin{bmatrix} 1 & & & & & & \\ & 1 & & & & & \\ & & \frac{5}{2} & -1 & -\frac{1}{4} & & \\ & & -1 & \frac{5}{2} & -1 & & \\ & & -\frac{1}{4} & -1 & \frac{5}{2} & & \\ & & & & & 1 & \\ & & & & & & 1 \end{bmatrix} \begin{Bmatrix} u_1 = 0.0 \\ u_2 = 0.1 \\ u_3 \\ u_4 \\ u_5 \\ u_6 = 0.5 \\ u_7 = 0.6 \end{Bmatrix} = \begin{Bmatrix} 0.00 \\ 0.10 \\ 0.10 \\ 0.15 \\ 0.65 \\ 0.50 \\ 0.60 \end{Bmatrix} \tag{3.17}$$

resulting in following displacement vector

$$u = \begin{Bmatrix} 0.0 & 0.1 & 0.2 & 0.3 & 0.4 & 0.5 & 0.6 \end{Bmatrix}^T. \tag{3.18}$$

3.4 One-dimensional static problem with no external load

In the following, we consider a one-dimensional case without external load with Dirichlet boundary conditions $u(0) = 0$ and $u(1) = 1$. The main purpose of this experiment is to demonstrate the importance of correctly imposing the boundary conditions nonlocally in the PD model. The PD solution will be compared with the classical elasticity solution using linear FE. We consider a one-

dimensional domain $\Omega = (0, 1)$ divided into 50 uniform intervals Δx. The Dirichlet boundary conditions are imposed on $u(0) = 0$ and $u(1) = 1$ for the FE model. For the PD model, the boundary of the domain is extended to a nonlocal boundary layer, so that additional nodes are added to the left and to the right sides of the domain. We use a fixed horizon of $\delta = 4\Delta x$ and vary the size of the boundary layer when imposing boundary conditions.

In Figure 3.5 we present the displacement profile for the FE and PD models. We observe that the profiles produced by the PD model is highly influenced by the size of the boundary layer. Observe that, in order to have a linear displacement profile the size of the boundary layer has to be at least of the same size of the horizon, in this case $\delta = 4\Delta x$. It is know that in PD the boundary conditions should be imposed over a boundary layer, since PD is a nonlocal theory. The size of this layer is not easily found in the literature, however.

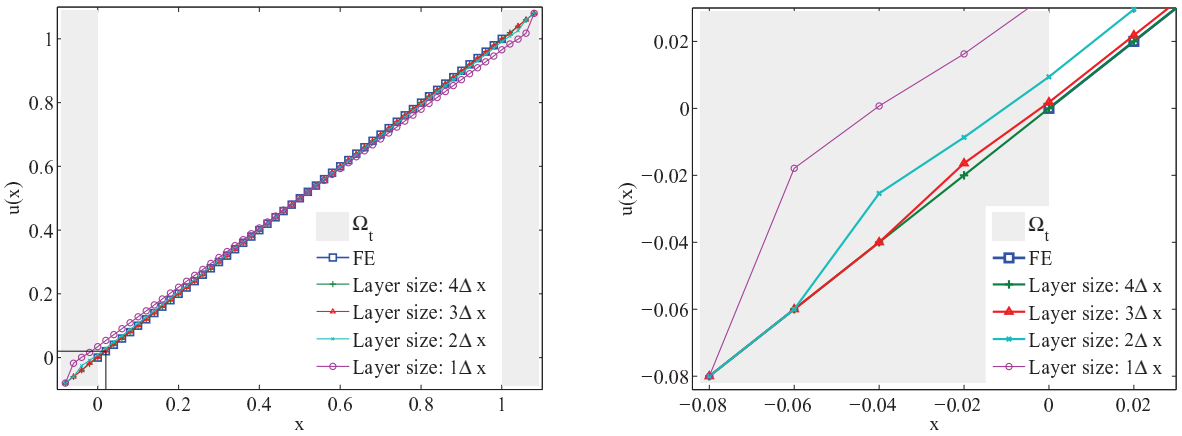

(a) PD solution

(b) Zoom in the boundary layer

Figura 3.5: Displacement profile comparison for the a one-dimensional case with no external load with Dirichlet boundary conditions $u(0) = 0$ and $u(1) = 1$; The extended layers (Ω_t) for imposing boundary conditions in the PD model are shaded by gray. The same horizon ($\delta = \Delta x$) was used in all PD simulations but we vary the size of the boundary layers from 1 to 4. Note that a linear profile is produced only when the boundary layer is of the same size of the horizon ($4\Delta x$).

4 NUMERICAL SOLUTION METHOD

In this chapter, we solve two-dimensional plane stress problems using the PD theory. We use the dynamic relaxation method (DRM) with kinetic damping to obtain the steady-state solutions to the system of ordinary differential equations resulting from the discretization of the PD equation and then we compare the results against FE results. We propose a methodology to compute the stresses from the PD solution as a post-processing step of the simulation. Since PD is entirely based on the relative displacements among particles the concept of stress is not necessary. However, engineering failure criteria are usually based on stresses distribution. As cited before, in (LEHOUCQ AND SILLING, 2008) a notion of a PD stress tensor is defined via a variational formulation derived from nonlocal interactions. We intend to estimate stresses in a more practical manner focusing on engineering applications. We propose a simple methodology in which we generate a Delaunay triangulation on the PD grid and then compute stresses in the same manner as in the FE. The stress is evaluated at the integration point of the triangular element and then it is transferred to the PD nodes by a smoothing scheme in which the stress at the nodes is weighted by the element area.

In the following, we first introduce the dynamic relaxation method (DRM) with kinetic damping in Section 4.1. Then we study plates with and without hole with prescribed displacements in one and two directions. Finally, we consider the problem of coupling PD and FE for concurrent multiscale simulations in two-dimensional domains. A plate with hole at its center is used to display damage prediction capabilities of the coupled scheme.

4.1 The dynamic relaxation method (DRM)

We briefly introduce the simple and effective dynamic relaxation method (DRM) with kinetic damping that is used in this study. A more detailed description of the method is found in (BARNES, 1988; WAKEFIELD, 1999; WOOD, 2002; HAN AND LEE, 2003; LEE *et al.*, 2011).

We adopted the DRM to simulate the quasi-static loading condition of the two-dimensional problems. The method is based on the fact that the static solution is the steady-state part of the transient response of the system. An artificial damping is introduced to guide the solution into the steady-state regime as fast as possible. The dynamic equilibrium equation can be written as follows

$$\mathbf{p}^n = \mathbf{M}\mathbf{a}^n + \mathbf{C}\mathbf{v}^n + \mathbf{K}\mathbf{d}^n. \tag{4.1}$$

where $\mathbf{p}^n$ it the load, $\mathbf{M}$, $\mathbf{C}$ and $\mathbf{K}$ are mass, viscous damping and stiffness terms, respectively. $\mathbf{a}^n$, $\mathbf{v}^n$ and $\mathbf{d}^n$ are the acceleration, velocity and displacement vectors at time step n.

We use a velocity-Verlet scheme when discretizing time in LAMMPS. The velocity-Verlet scheme is generally expressed in three steps

$$\mathbf{v}_i{}^{n+1/2} = \mathbf{v}_i{}^n + \frac{\Delta t}{2m_i}\mathbf{f}_i{}^n, \tag{4.2}$$

$$\mathbf{y}_i{}^{n+1} = \mathbf{y}_i{}^n + (\Delta t)\mathbf{v}_i{}^{n+1/2}, \tag{4.3}$$

$$\mathbf{v}_i{}^{n+1} = \mathbf{v}_i{}^{n+1/2} + \frac{\Delta t}{2m_i}\mathbf{f}_i{}^{n+1}, \tag{4.4}$$

where m_i denotes the mass of a particle and $\mathbf{f}_i^n$ denotes the net force density on particle i at timestep n (the LAMMPS command `fix nve` performs a velocity-Verlet integration).

By considering the DRM without viscous damping ($\mathbf{C} = 0$), the number of parameters is reduced and the analysis becomes simpler. The numerical analysis in the DRM is controlled only by time increments and nodal mass terms. In the kinetic damping process, the behavior of the structure can be re-established by setting the nodal velocity to zero at the kinetic energy peak state. The iterative procedures are repeated until the appropriate convergence criterion is satisfied.

The mass matrix is the most important and unique term that is used to control the convergence process of the DRM with the kinetic damping technique. To determine the static equilibrium with

the DRM, the mass terms do not need to be the true structural mass (it can be chosen to obtain faster convergence). Let the mass matrix $\mathbf{M}$ be replaced by a fictitious diagonal mass matrix $\mathbf{\Lambda}$. There are many different methods for choosing the fictitious mass term $\mathbf{\Lambda}$. One of the most common choice is to take $\mathbf{\Lambda}$ proportional to stiffness of the system (KILIC, 2008)

$$\lambda_{ii} \geq \alpha \frac{1}{4} \Delta t^2 \sum_j |K_{ij}|, \tag{4.5}$$

in which K_{ij} are the terms of the stiffness matrix of the system of equations under consideration.

Following (KILIC, 2008; LEE *et al.*, 2011), we take the time step size of 1 ($\Delta t = 1$), the constant $\alpha = 2$ and the fictitious mass terms as

$$\lambda_{ii} = \frac{1}{2} \sum_j |K_{ij}|. \tag{4.6}$$

4.2 Benchmark solutions - two-dimensional problems

The effectiveness of the PD solutions are demonstrated by considering basic structural components subjected to prescribed loads. The components considered are plates with or without a circular hole. The effects of grid refinement and the PD horizon are analyzed. In the Appendix A we provide the LAMMPS input files used in this section.

The PD solution for the two-dimensional problems was obtained using the PD module in LAMMPS that allows only structured (evenly-spaced) grids in both x- and y-direction. We vanish the forces in the orthogonal direction (z) to the plane xy, that is equivalent to a plane stress problem in classical continuum mechanics. Since the symmetry of the problems is evident, in the FE simulations we model just one-quarter of the domain. However, to avoid introducing boundary errors in the areas that we want to estimate stresses, we modeled the entire plate in the PD simulation.

Five evenly-spaced grids were used in the PD simulations (Table 4.1). The same discretization is used in both x- and y-direction. We vary the value of the horizon from $\delta = 3\Delta$ to $\delta = 6\Delta$, where Δ is the grid spacing. In the PD simulations, the boundaries of the domain are extended to a nonlocal boundary layer of 10mm for all grids (the boundary layers adds more points). We show the PD results just for one-quarter of the domain even though we have solved the entire plate.

Poisson's ratio $\nu = 1/3$ and Young's modulus (elastic modulus) $E = 72$ GPa where used in both PD and FE simulations (in this case the bulk modulus is $K = 72$ GPa; see Equation (3.11)).

PD Grid	No. of Points in Each Direction	No. of Points (Total)	No. of Free Points
1	61 x 61	3,721	2,401
2	121 x 121	14,641	9,801
3	241 x 241	58,081	39,601
4	481 x 481	231,361	159,201
5	601 x 601	361,201	249,001

Tabela 4.1: Features of the two-dimensional PD grids used in the simulation.

To evaluate the PD solutions we use the FE results as the reference values. For the plate without hole we use a FE mesh of 400 quadrilateral elements and 441 nodes (evenly-spaced in both x- and y-direction). In addition, for the plate with hole, the reference FE solution was obtained with a mesh with 861 quadrilateral elements and 927 nodes.

We have chosen, due to the large amount of data that was generated, to show the PD results for two grids, 1 (61x61) and 4 (481x481), only. The results for the other cases are shown in Appendix B.

4.2.1 Plate with prescribed displacements in x

Consider the plate without external load shown in Figure 4.1 with Dirichlet boundary conditions and prescribed displacements

$$\begin{aligned} u(-50, y) &= -5.0 \times 10^{-3}\text{mm} \quad \text{and} \\ u(50, y) &= 5.0 \times 10^{-3}\text{mm}. \end{aligned}$$

Observe that the prescribed displacements on the PD boundaries must have a linear gradient profile (i.e., proportional to the point position x)

$$\begin{aligned} u(-60 \leq x \leq -50, y) &= x \times 10^{-4}\text{mm} \quad \text{and} \\ u(50 \leq x \leq 60, y) &= x \times 10^{-4}\text{mm}. \end{aligned}$$

The prescribed displacements are applied on the boundaries of the PD domain at time step zero and the change in displacement at a given point x = y = 20 mm is shown in Figure 4.2. As shown in Figure 4.2, the displacement in the x-direction converges faster than the one in y. We also note that as the grid gets finer the number of iterations required to reach convergence increases. While for grid 1 (61x61), the displacement in x converges with approximately 100 iterations, grid 4 (481x481) it is requires about 500 iterations. Another important comment from Figure 4.2 is that convergence is not very dependent on horizon size.

In Figure 4.3, we present the numerical results for the displacement field. The steady state displacements are compared against the FE solution. We observe that linear profiles are produced overall, as expected. Figures 4.3(a) and 4.3(c) show that the displacements in the x-direction for the two PD grids are close to the FE solution for all values of the horizon. On the other hand, the displacements for the y direction are usually slight different from the FE solution for all grids and values of the horizon (Figures 4.3(b) and 4.3(d)). From the the same figures, we also note that the PD solution for the values of horizon $\delta = 3$ and $\delta = 4$ are closer to the FE solution for both PD

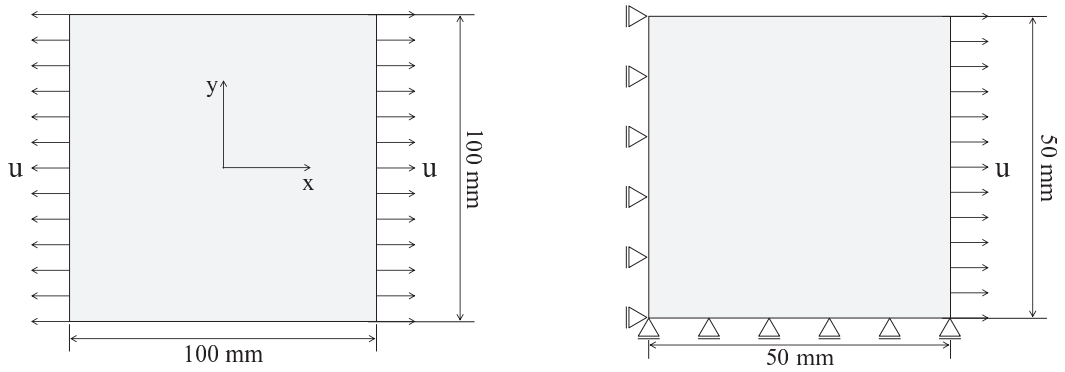

(a) Plate with prescribed displacement $\mathbf{u}$ in x.

(b) FE numerical model.

Figura 4.1: Plate with prescribed displacements in x-direction and the model used in the FE simulation.

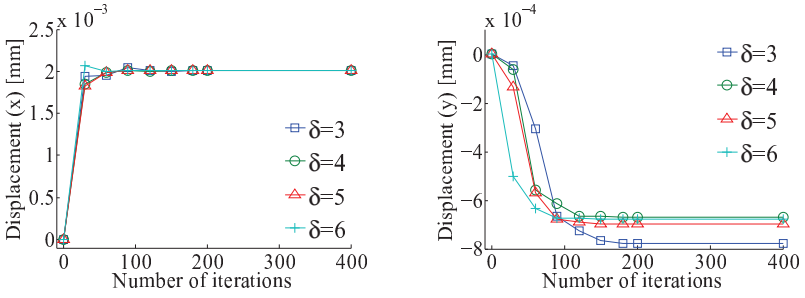

(a) grid: 61x61

(b) grid: 61x61

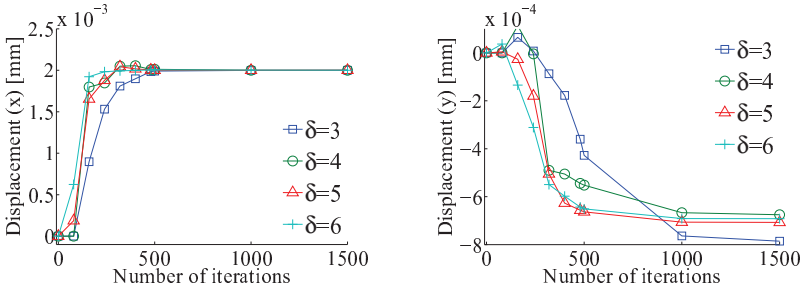

(c) grid: 481x481

(d) grid: 481x481

Figura 4.2: Displacements at the point $x = y = 20$ mm for the case of the plate without hole and prescribed displacements in x-direction. For all grids we vary the horizon from $\delta = 3\Delta$ to $\delta = 6\Delta$.

grids.

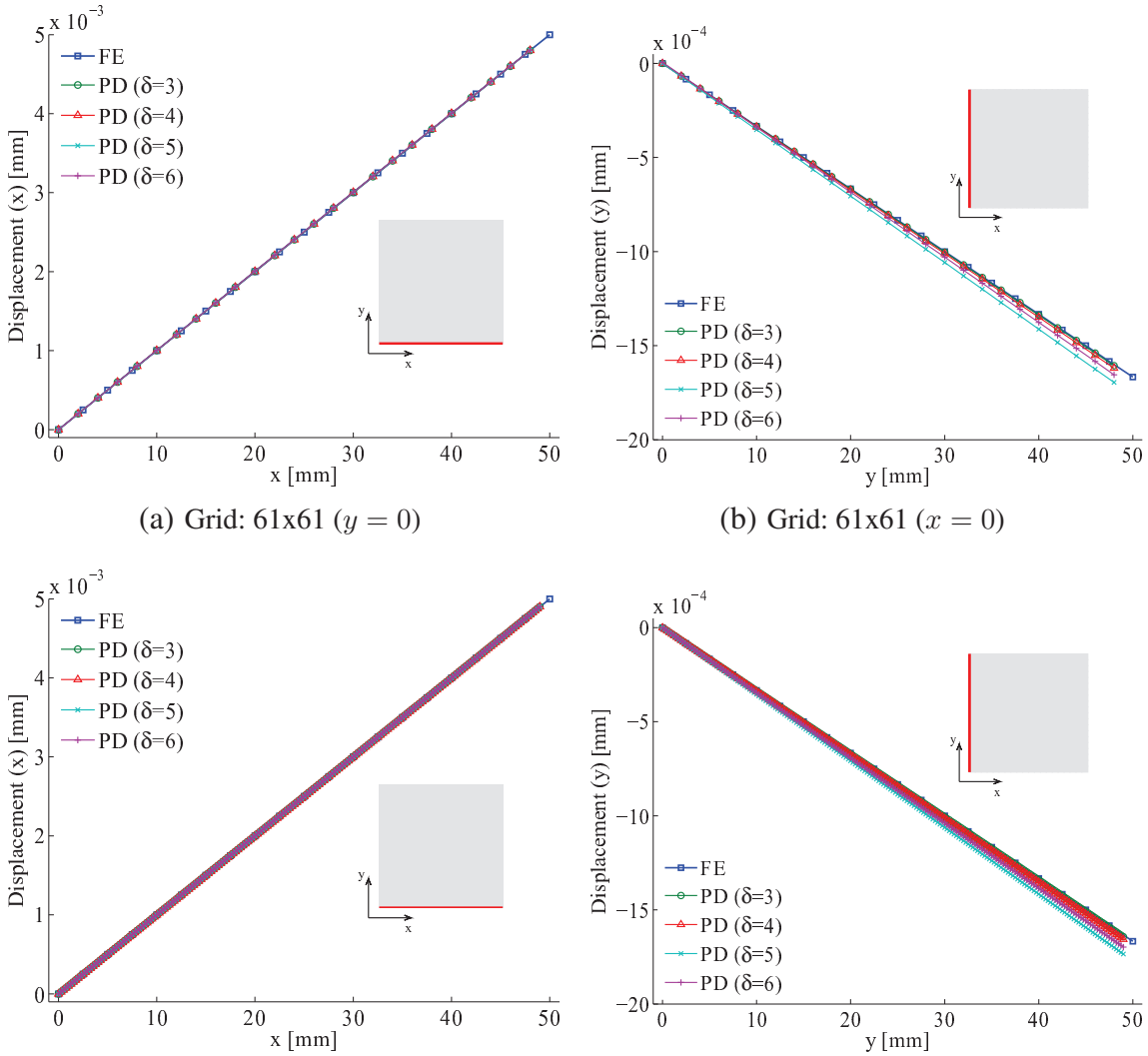

(a) Grid: 61x61 ($y = 0$)

(b) Grid: 61x61 ($x = 0$)

(c) Grid: 481x481 ($y = 0$)

(d) Grid: 481x481 ($x = 0$)

Figura 4.3: Displacement profiles comparison for the case of the plate without hole and prescribed displacements in the x-direction for the grids: 61x61 and 481x481. The extended layers for imposing boundary conditions in the PD model are fixed in 10 mm at each boundary (not shown in the figure). We vary the horizon from $\delta = 3\Delta$ to $\delta = 6\Delta$.

Free surface effect is possibly the main reason for the differences in the y-displacement-direction. Material points near a free surface have some of their interactions lost as compared to those points which are completely surrounded by other material points. Hence, these points experience stiffness loss (KILIC, 2008). Because of this effect, the deformation in the y-direction is not completely uniform and the effective Poisson's ratio for points near the free surfaces is slightly

different from the theoretical predicted value of $1/3$.

The methodology proposed in the beginning of this chapter was used to compute the stress field for the PD simulation. In Figure 4.4, we present stresses for both FE and PD simulations. Figures 4.4(a) and 4.4(c) show that the stresses are more dependent on the horizon size than the displacements in the x-direction. Since the differences in the y-displacement are more pronounced, we observe that the differences in σ_{yy} are also larger (Figures 4.4(b) and 4.4(d)). Free surface effects also justify the fact that for small horizons the PD stress curves get closer to the FE one (Figure 4.4). As the horizon size gets smaller, the number of points that is not completely surrounded by other material points gets lower. Thus, the solution for small values of horizon is closer to the FE result. Furthermore, by Figure 4.4(c), for the best case $(\delta = 3\Delta)$ the difference in the mean stress values between PD and FE is less than 0.5% and for the worst case the difference is not larger than 1.0%.

Besides free surface effects, other sources of inaccuracy should be pointed out. The values of the displacement used to post-process the PD stress field were read from the LAMMPS dump file. The data were recorded in short format (4 digits after the decimal point). We consider that using displacements values in long format (14 to 15 digits after the decimal point) might make the stress distribution a bit more uniform.

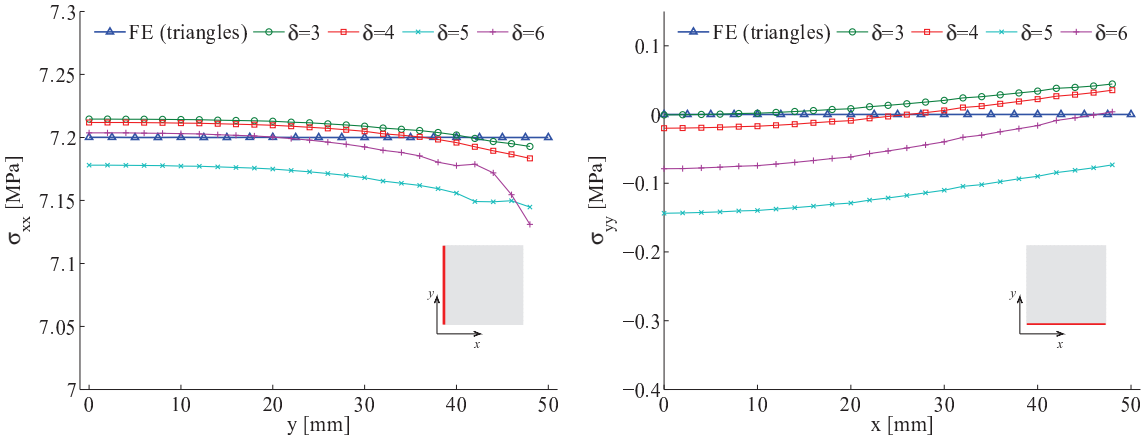

(a) Grid: 61x61 ($x = 0$)

(b) Grid: 61x61 ($y = 0$)

(c) Grid: 481x481 ($x = 0$)

(d) Grid: 481x481 ($y = 0$)

Figura 4.4: Stresses comparison for the case of the plate without hole and prescribed displacements in the x-direction for the grids: 61x61 and 481x481. The extended layers for imposing boundary conditions in the PD model are fixed in 10 mm at each boundary (not shown in the figure). We vary the horizon from $\delta = 3\Delta$ to $\delta = 6\Delta$.

4.2.2 Plate with prescribed displacements in x and y

Consider the plate without external load shown in Figure 4.5 with Dirichlet boundary conditions and prescribed displacements

$$\begin{aligned} u(-50, y) &= -5.0 \times 10^{-3}\text{mm}, \\ u(50, y) &= 5.0 \times 10^{-3}\text{mm}, \\ u(x, -50) &= -5.0 \times 10^{-3}\text{mm} \quad \text{and} \\ u(x, 50) &= 5.0 \times 10^{-3}\text{mm}. \end{aligned}$$

The prescribed displacements on the PD boundaries are as follows

$$\begin{aligned} u(-60 \leq x \leq -50, y) &= x \times 10^{-4}\text{mm}, \\ u(50 \leq x \leq 60, y) &= x \times 10^{-4}\text{mm}, \\ u(x, -60 \leq y \leq -50) &= y \times 10^{-4}\text{mm} \quad \text{and} \\ u(x, 50 \leq y \leq 60) &= y \times 10^{-4}\text{mm}. \end{aligned}$$

The change in displacement at the point x = y = 20 mm is shown in Figure 4.6. As shown in Figure 4.6, for this case, it takes the same number of iterations to x- and y-direction to reach converged results. As we note for the case of Section 4.2.1, the number of iterations required to convergence also increases as the grid is refined. Another comment is that, for this case, with prescribed displacements in both directions, fewer iterations are required to reach converged results when compared to the case of Section 4.2.1.

The main reason to run this case, with prescribed displacements in both directions, is to evaluate the influence of free the surface in the PD simulations. The steady state displacements are

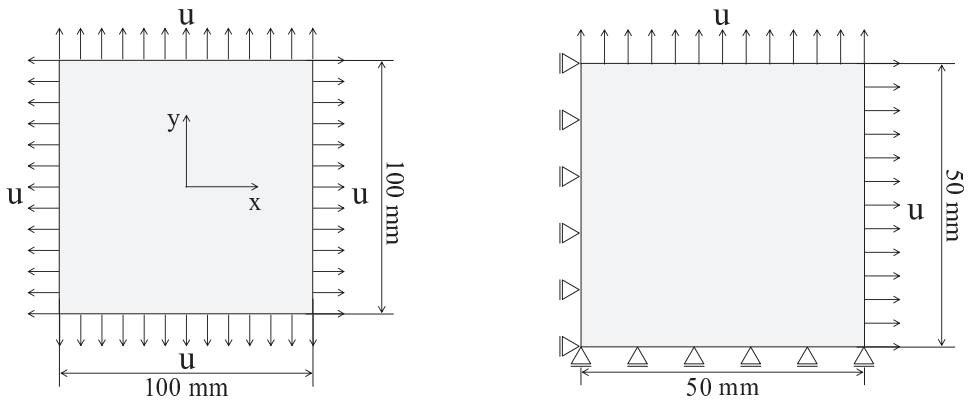

(a) Plate with prescribed displacement $\mathbf{u}$ in x and y.

(b) FE numerical model

Figura 4.5: Plate with prescribed displacements in both x- and y-direction and the model used in the FE simulation.

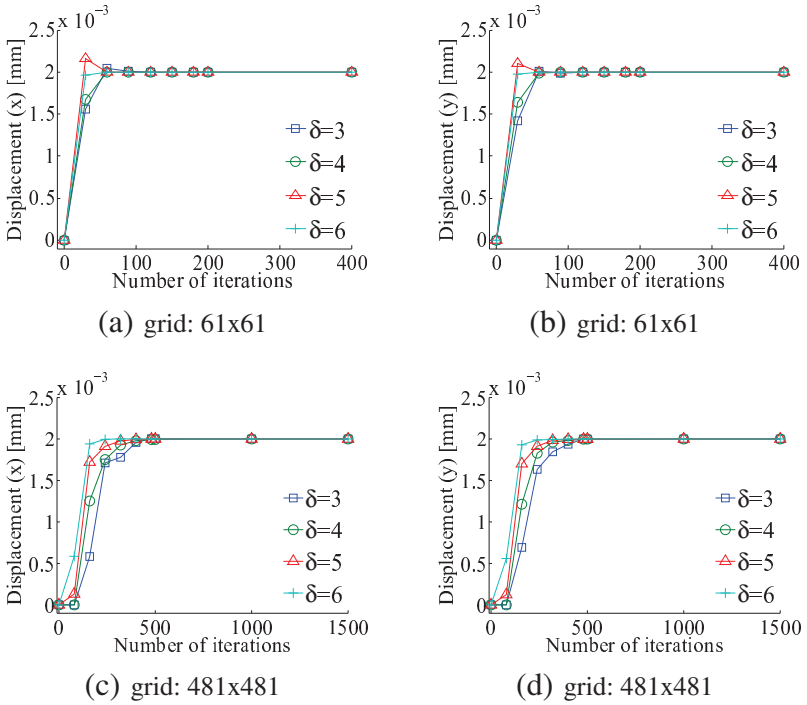

(a) grid: 61x61

(b) grid: 61x61

(c) grid: 481x481

(d) grid: 481x481

Figura 4.6: Displacements at the point $x = y = 20$ mm for the case of the plate without hole and prescribed displacements in both x- and y-direction. For all grids we vary the horizon from $\delta = 3\Delta$ to $\delta = 6\Delta$.

compared against the FE solution. In Figure 4.7, we present the numerical results for the displacement field. We observe that linear profiles are produced in both directions (Figures 4.7(a) and 4.7(c)). The displacements in both x- and y-direction agree very well with the FE solution for all PD grids and values of the horizon. The difference in both displacements and stresses is less than 0.1%. Thus, there is no visible difference between PD and FE solutions (Figures 4.7 and 4.8).

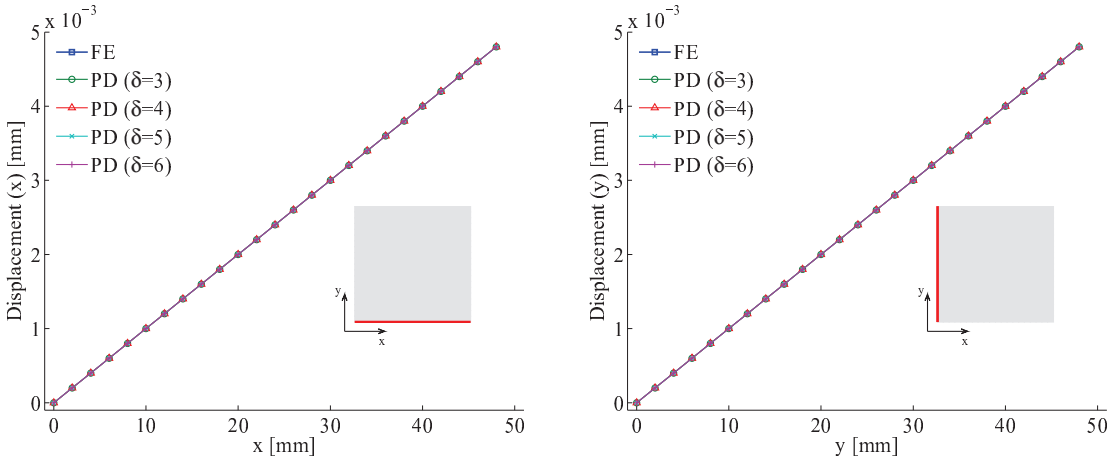

(a) Grid: 61x61 ($y = 0$)

(b) Grid: 61x61 ($x = 0$)

(c) Grid: 481x481 ($y = 0$)

(d) Grid: 481x481 ($x = 0$)

Figura 4.7: Displacement profiles comparison for the case of the plate without hole and prescribed displacements in both x- and y-direction for the grids: 61x61 and 481x481. The extended layers for imposing boundary conditions in the PD model are fixed in 10 mm at each boundary (not shown in the figure). We vary the horizon from $\delta = 3\Delta$ to $\delta = 6\Delta$.

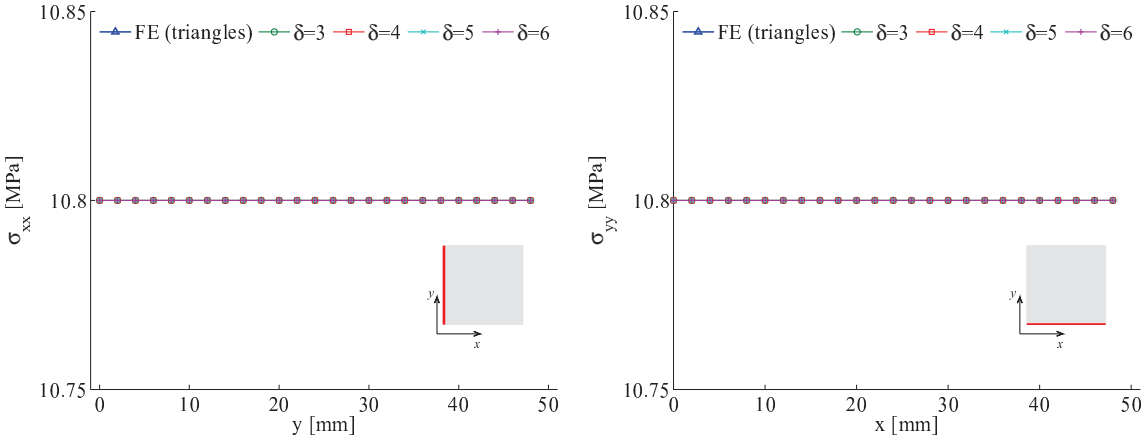

(a) Grid: 61x61 ($x = 0$)

(b) Grid: 61x61 ($y = 0$)

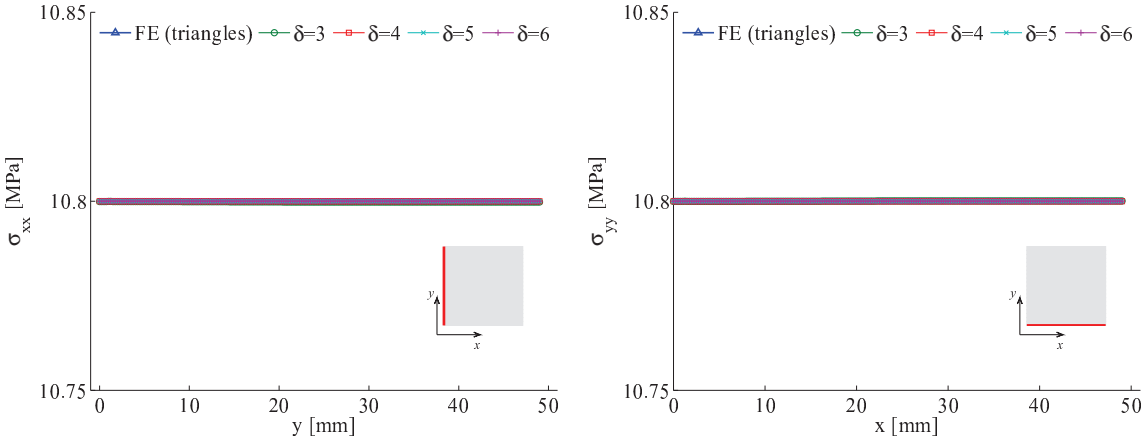

(c) Grid: 481x481 ($x = 0$)

(d) Grid: 481x481 ($y = 0$)

Figura 4.8: Stresses comparison for the case of the plate without hole and prescribed displacements in both x- and y-direction for the grids: 61x61 and 481x481. The extended layers for imposing boundary conditions in the PD model are fixed in 10 mm at each boundary (not shown in the figure). We vary the horizon from $\delta = 3\Delta$ to $\delta = 6\Delta$.

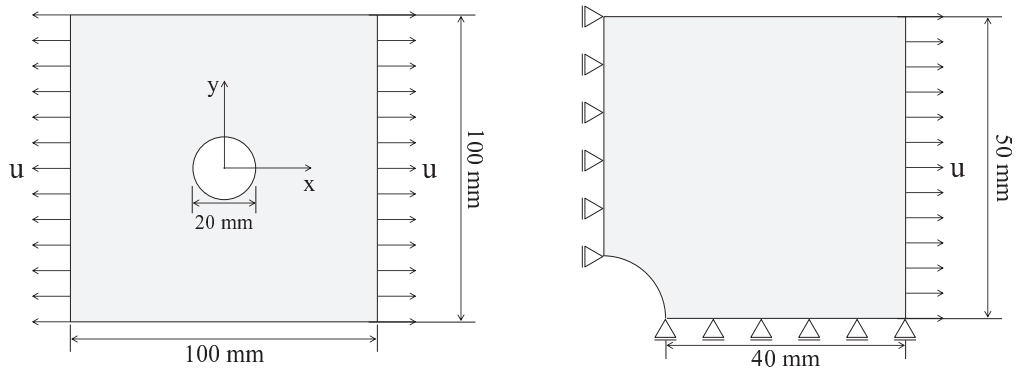

(a) Plate with prescribed displacements $\mathbf{u}$ in x.

(b) FE numerical model.

Figura 4.9: Plate with hole and prescribed displacements in x-direction and the model used in the FE simulation.

4.2.3 Plate with hole and prescribed displacements in x

Consider the plate with hole without external load shown in Figure 4.9 with Dirichlet boundary conditions and prescribed displacements

$$\begin{aligned} u(-50, y) &= -5.0 \times 10^{-3}\text{mm} \quad \text{and} \\ u(50, y) &= 5.0 \times 10^{-3}\text{mm}. \end{aligned}$$

The prescribed displacements on the PD boundaries are as follows

$$\begin{aligned} u(-60 \leq x \leq -50, y) &= x \times 10^{-4}\text{mm} \quad \text{and} \\ u(50 \leq x \leq 60, y) &= x \times 10^{-4}\text{mm}. \end{aligned}$$

The change in displacement at the point $x = y = 20$ mm is shown in Figure 4.10. We note the same behavior of the previous cases where the number of iterations increases as the grid gets finer. We also note that there is no significant difference in the number of iterations required in this case to reach convergence when compared to the case without hole.

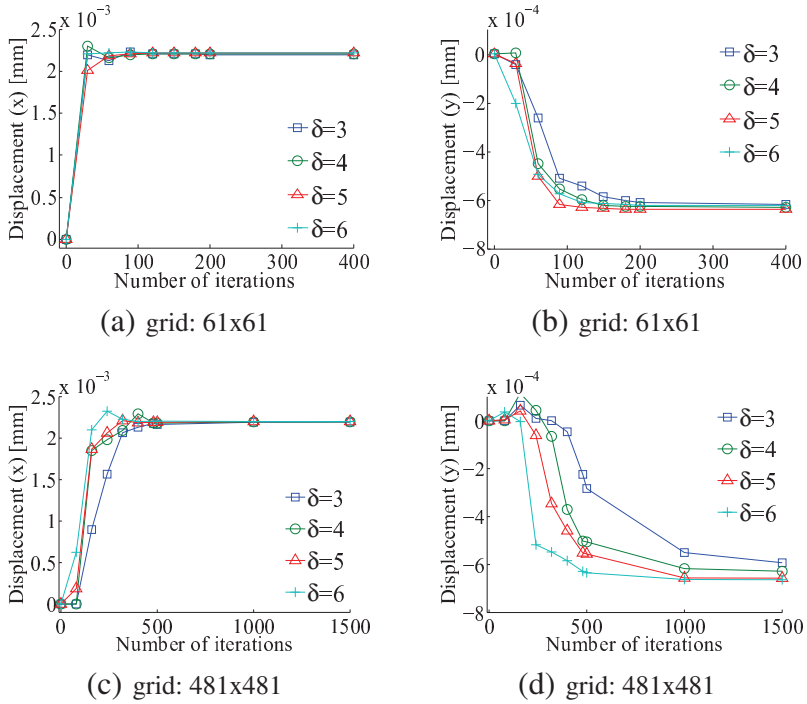

(a) grid: 61x61 (b) grid: 61x61

(c) grid: 481x481 (d) grid: 481x481

Figura 4.10: Displacements at the point $x = y = 20$ mm for the case of the plate with hole and prescribed displacements in x-direction. For all grids we vary the horizon from $\delta = 3\Delta$ to $\delta = 6\Delta$.

The main objective of this case is to check if the PD solution is able to capture the non-linear displacement and stress profiles. The solution for this problem using the FEM is presented in Figure 4.11.

In Figures 4.12 and 4.13, we present the displacement field in the x- and y-direction for the PD simulation computed with the two PD grids. Serving as a reference to the PD solutions, the FE solution is also plotted in the figures. Overall the displacement fields shown in Figures 4.12(a) to 4.12(h) and 4.13(a) to 4.13(h) qualitatively follow the FE solution. We observe that, as for the plate without hole, the displacement profiles for x-direction are quite close to the FE solution. Furthermore, some results in the y-direction follow very close the FE solution

In order to check the accuracy of the methodology used to compute the PD stresses, we applied the same scheme to the FE solution of this problem, i.e., we perform a Delaunay triangulation on the quadrilateral mesh and compute stresses using the triangle shape functions. The result is

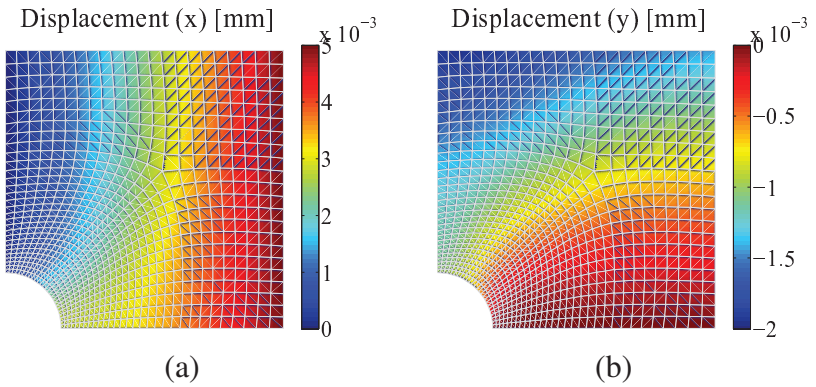

Figura 4.11: Displacement profile for the plate with prescribed displacements in x-direction obtained with the FE approximation.

shown in the Appendix C. According to the results shown in Figure C.1, the triangular mesh recovers quite well the stress field with no significant difference. However, the number of elements of the triangular mesh is twice the number of quadrilateral elements. As explained in the introduction of this chapter, the stress is computed at the integration point of the triangular element and then the nodal values are evaluated by a smoothing procedure. Since the smoothing procedure using the triangular mesh involves twice the number of operations, the result for triangles is a bit less accurate when compared to the stress values computed with quadrilaterals. This fact explains the small differences observed between the two curves in the graphs shown in Figures C.1(e) and C.1(f).

At this point some technical limitations should be highlighted. As commented before, only structured (evenly-spaced) grids in both directions (x and y) can be used in the PD implementation in LAMMPS. For a structured grid, hole cannot be accurately represented. It means that the geometric models for FE and discretized PD are slightly different. hole become square shaped as the grid gets coarser. Because of this, it is difficult to discuss convergence, since it is not possible to identify whether the PD solution gets close to the FE solution, because the mesh is finer or because the geometry is better represented. More importantly, this is not a limitation of the PD theory, but a problem with the manner in which the PD equation was discretized.

Another source of errors in the stress estimation is due to the triangulation itself. The trian-

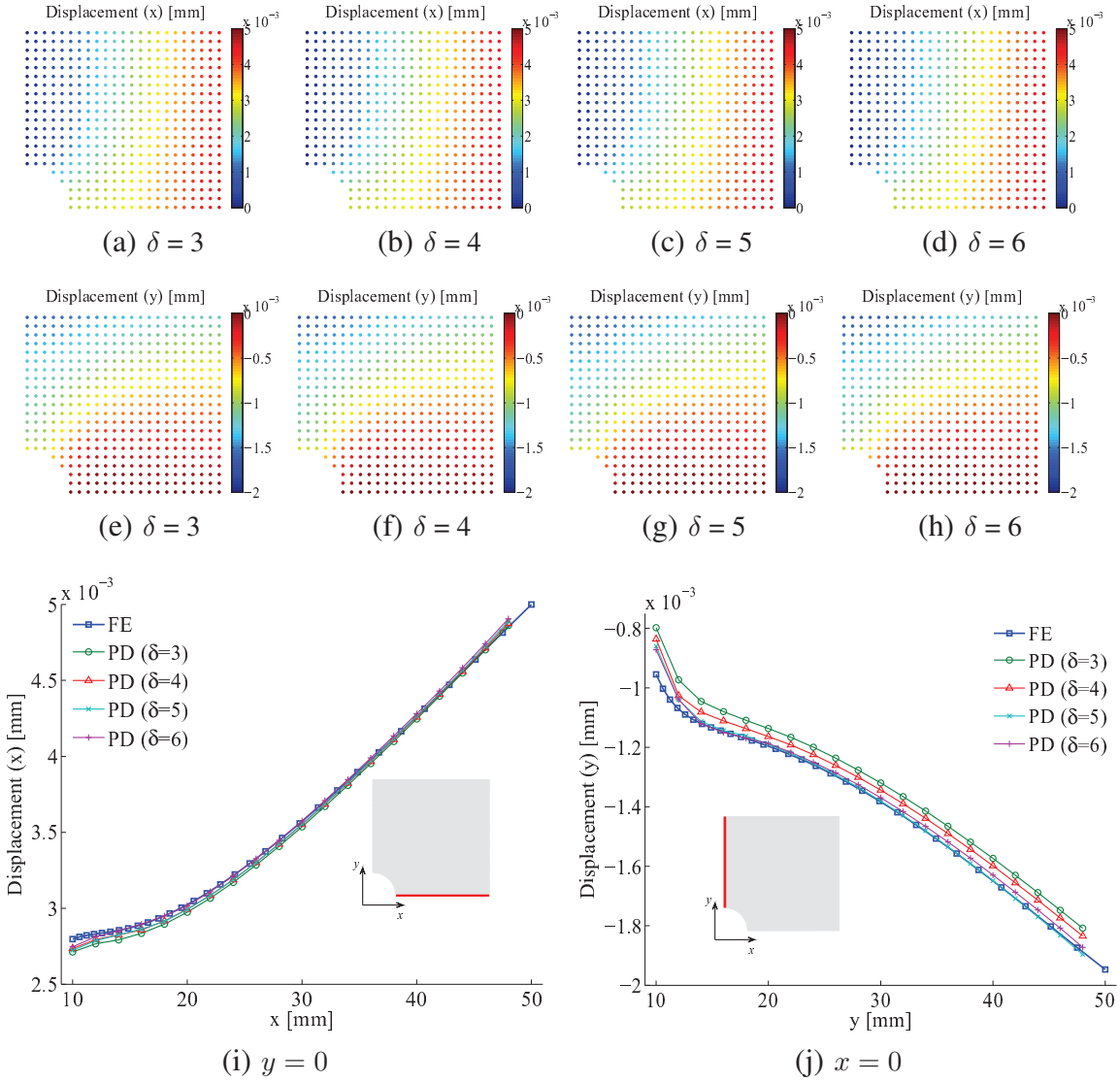

Figura 4.12: Displacement distribution for the case of the plate with hole and prescribed displacements in x-direction computed with the 61x61 grid. The extended layers for imposing boundary conditions in the PD model are fixed in 10 mm at each boundary (not shown in the figure). We vary the horizon from $\delta = 3\Delta$ to $\delta = 6\Delta$. In (i) and (j) the displacements in x and y are compared with the FE solution.

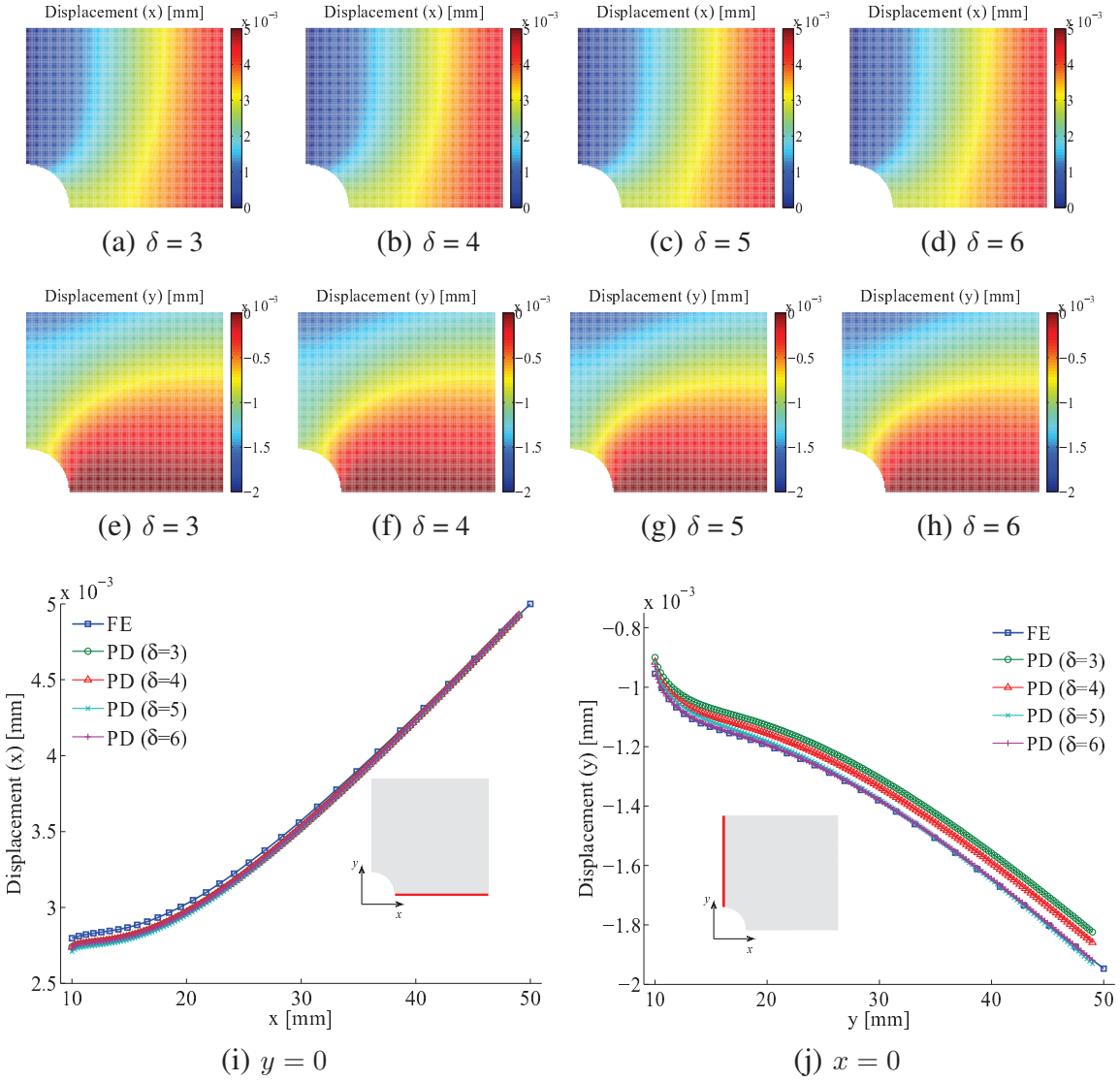

Figura 4.13: Displacement distribution for the case of the plate with hole and prescribed displacements in x-direction computed with the 481x481 grid. The extended layers for imposing boundary conditions in the PD model are fixed in 10 mm at each boundary (not shown in the figure). We vary the horizon from $\delta = 3\Delta$ to $\delta = 6\Delta$. In (i) and (j) the displacements in x and y are compared with the FE solution.

gulation follows the evenly-spaced PD nodes and not the geometry. A triangular mesh following the geometry might be more efficient. However, we are focused on estimating the stresses only. As mentioned before, the stress field is not required in the PD theory since cracks propagate autonomously with the breakage of the bonds between material points.

Figures 4.14 and 4.15 show the stresses computed for the PD simulations. We can note that as the grid is refined the PD model is able to capture quite well the increase in tension at the boundary of the hole. Moreover, note that, even thought the PD model is able to capture the stress field near the hole, near the boundaries of the PD domain the difference, when compared to the FE solution, is higher. We shall point out two reasons. The first is the free surface effect that was already covered. And the second is the fact that for this problem under consideration the displacement profile on the boundaries is not completely uniform as it was imposed.

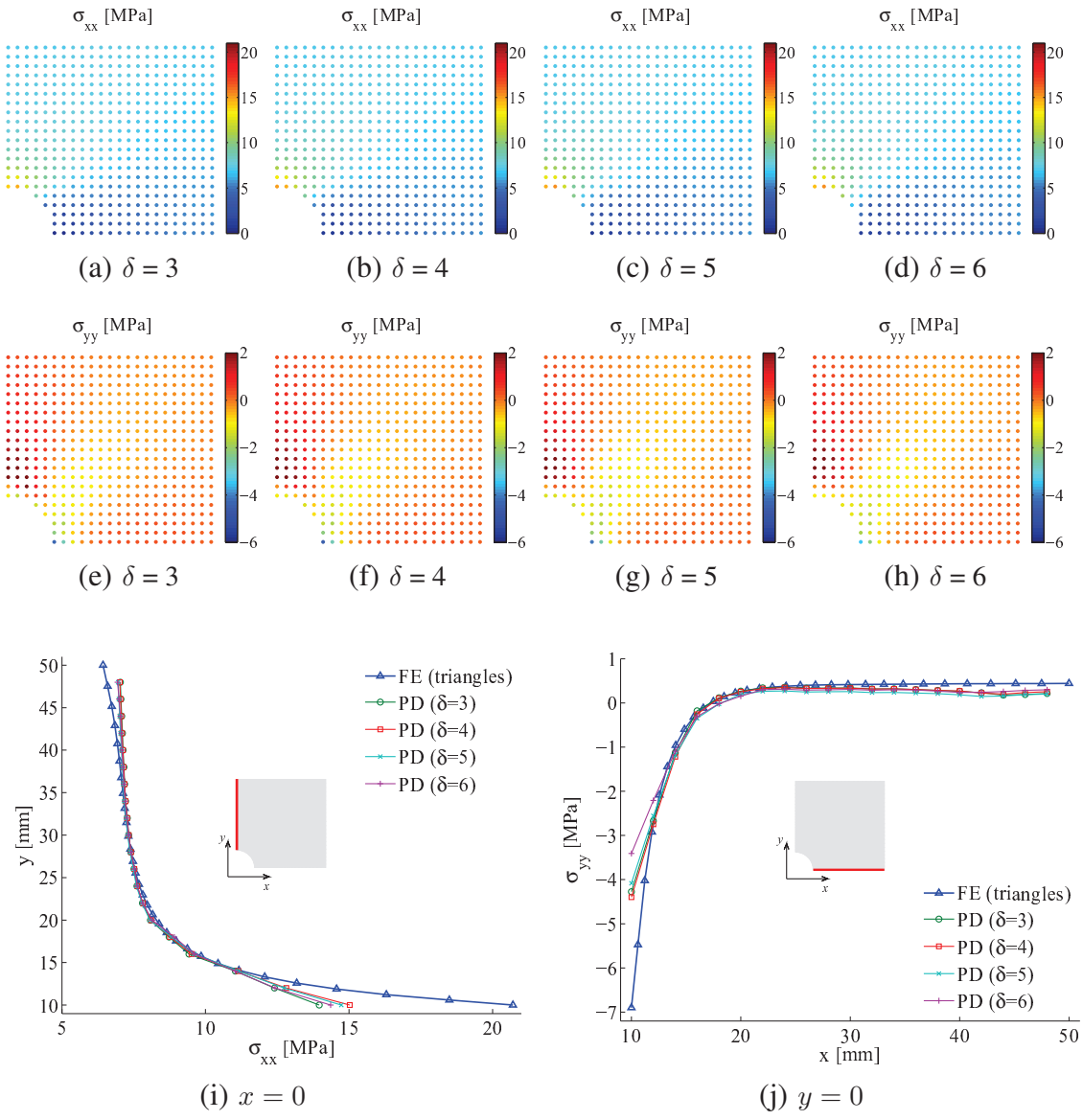

Figura 4.14: PD stresses for the case of the plate with hole and prescribed displacements in x-direction computed with the 61x61 grid. The extended layers for imposing boundary conditions in the PD model are fixed in 10 mm at each boundary (not shown in the figure). We vary the horizon from $\delta = 3\Delta$ to $\delta = 6\Delta$. In (i) and (j) σ_{xx} and σ_{yy} are compared with the FE solution.

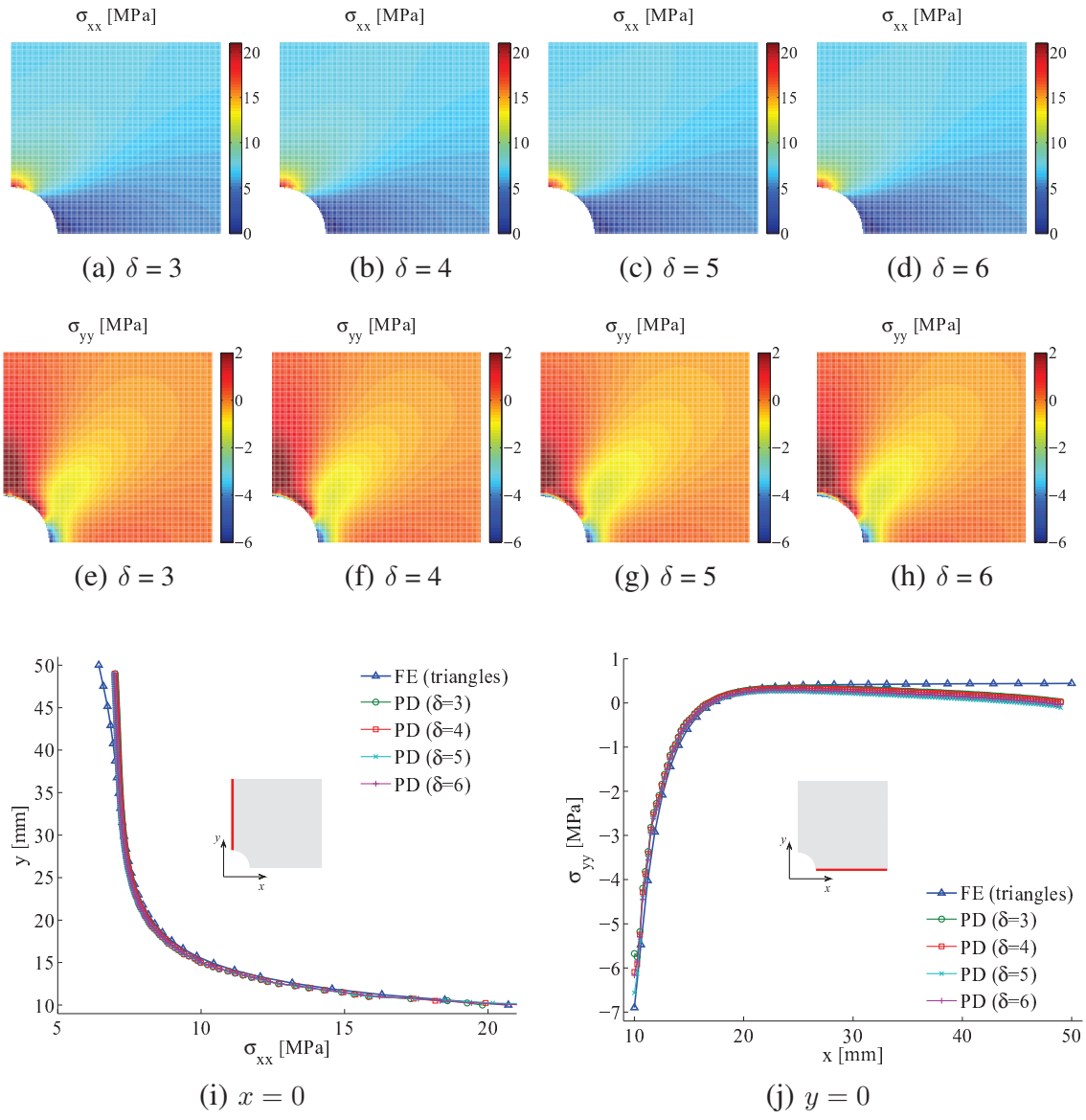

Figura 4.15: PD stresses for the case of the plate with hole and prescribed displacements in x-direction computed with the 481x481 grid. The extended layers for imposing boundary conditions in the PD model are fixed in 10 mm at each boundary (not shown in the figure). We vary the horizon from $\delta = 3\Delta$ to $\delta = 6\Delta$. In (i) and (j) σ_{xx} and σ_{yy} are compared with the FE solution.

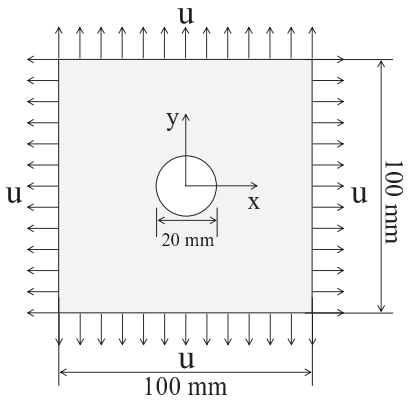

(a) Plate with prescribed displacement $\mathbf{u}$ in x and y.

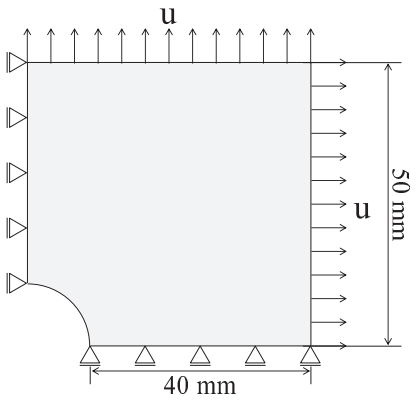

(b) FE numerical model.

Figura 4.16: Plate with hole and prescribed displacements in both x- and y-direction and the model used in the FE simulation.

4.2.4 Plate with hole and prescribed displacements in x and y

Consider the plate with hole without external load shown in Figure 4.16 with Dirichlet boundary conditions and prescribed displacements

$$\begin{aligned} u(-50, y) &= -5.0 \times 10^{-3}\text{mm}, \\ u(50, y) &= 5.0 \times 10^{-3}\text{mm}, \\ u(x, -50) &= -5.0 \times 10^{-3}\text{mm} \quad \text{and} \\ u(x, 50) &= 5.0 \times 10^{-3}\text{mm}. \end{aligned}$$

The prescribed displacements on the PD boundaries are as follows

$$\begin{aligned} u(-60 \leq x \leq -50, y) &= x \times 10^{-4}\text{mm}, \\ u(50 \leq x \leq 60, y) &= x \times 10^{-4}\text{mm}, \\ u(x, -60 \leq y \leq -50) &= y \times 10^{-4}\text{mm} \quad \text{and} \\ u(x, 50 \leq y \leq 60) &= y \times 10^{-4}\text{mm}. \end{aligned}$$

The changes in displacement at the point $x = y = 20$ mm is shown in Figure 4.17. We note the same behavior of the previous cases in the number of iterations according to the grid, i.e., more iterations is required for finer grids. Again, as it was observed for the case without hole, the problem with prescribed displacements in two directions converges much faster than when displacement is prescribed just in x-direction.

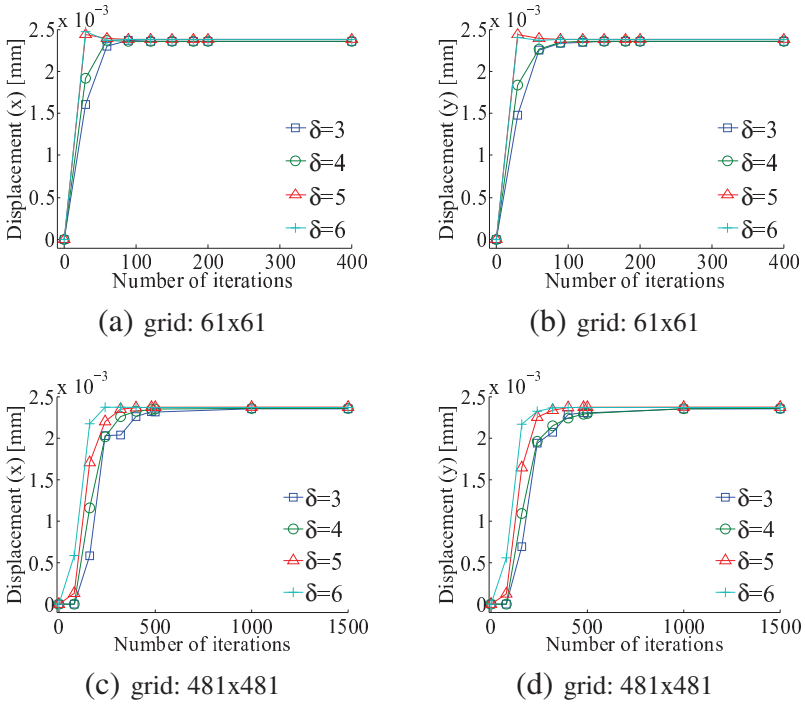

(a) grid: 61x61 (b) grid: 61x61

(c) grid: 481x481 (d) grid: 481x481

Figura 4.17: Displacements at the point $x = y = 20$ mm for the case of the plate with hole and prescribed displacements in both x- and y-direction. For all grids we vary the horizon from $\delta = 3\Delta$ to $\delta = 6\Delta$.

The main objective for solving this problem is to study the PD solution for non-linear displacement profiles in the absence of errors on the boundaries. Figure 4.18 shows the solution for this problem using the FEM.

In Figures 4.19 and 4.20, we show the displacement field in x- and y-direction for both PD and FE simulations. The PD displacement fields shown in Figures 4.19(a) to 4.19(h) and 4.20(a) to 4.20(h) are in good agreement with those obtained with FE simulation. Overall the PD simulations were able to very successfully capture the non-linear behavior of the displacement of the problem.

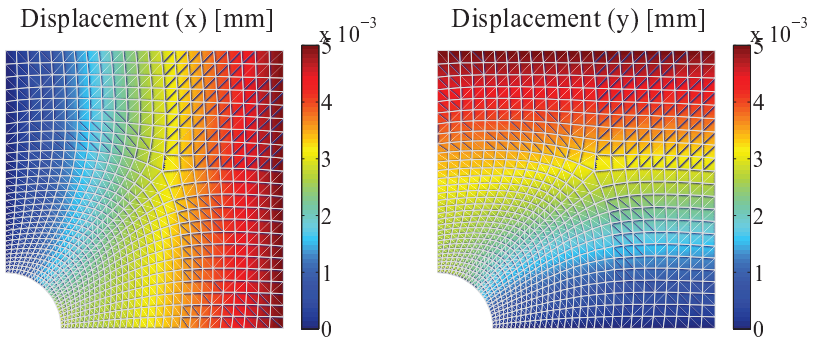

(a) (b)

Figura 4.18: Displacement profile for the plate with hole and prescribed displacements in both x- and y-direction obtained with the FE approximation.

Figures 4.21 and 4.22 show the PD stress fields. In Figures 4.21(i) and 4.22(i), the PD solution is compared against the FE solution. The results for the stress field confirms the good agreement already observed for the displacements. note that there is no differences in the solution for σ_{xx} and σ_{yy}.

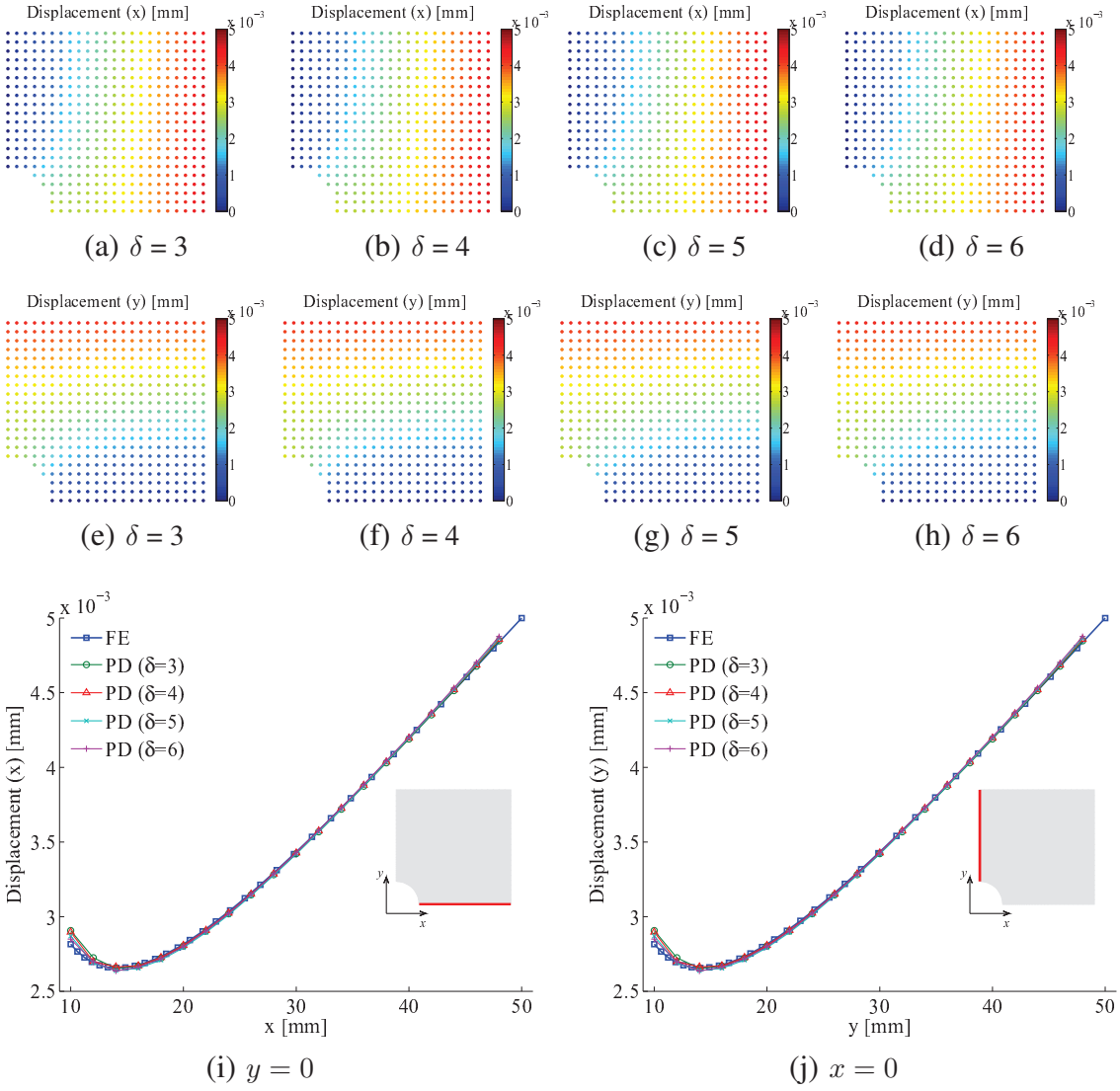

Figura 4.19: Displacement distribution for the case of the plate with hole and prescribed displacements in both x- and y-direction computed with the 61x61 grid. The extended layers for imposing boundary conditions in the PD model are fixed in 10 mm at each boundary (not shown in the figure). We vary the horizon from $\delta = 3\Delta$ to $\delta = 6\Delta$. In (i) and (j) the displacements in x and y are compared with the FE solution.

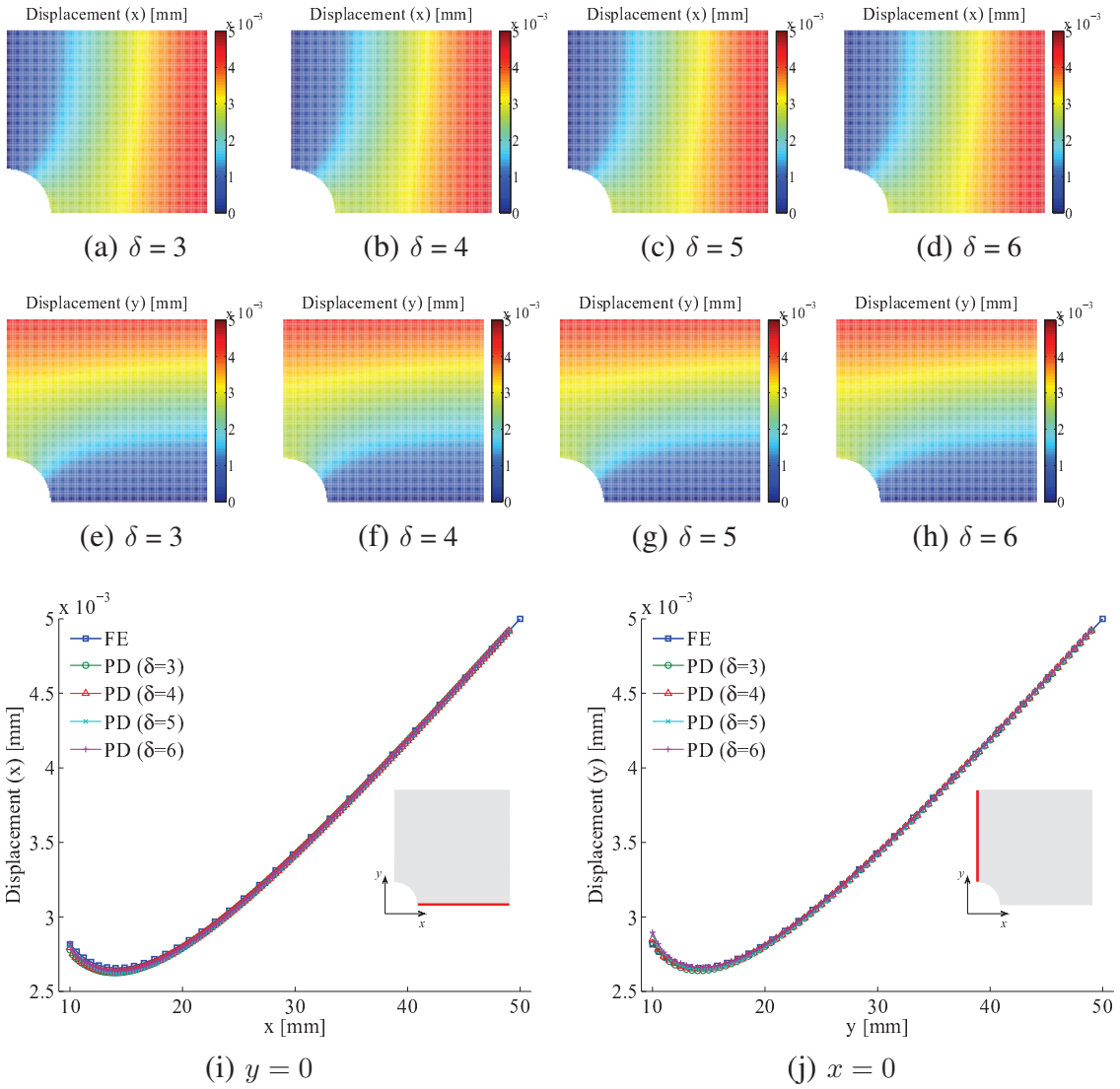

Figura 4.20: Displacement distribution for the case of the plate with hole and prescribed displacements in both x- and y-direction computed with the 481x481 grid. The extended layers for imposing boundary conditions in the PD model are fixed in 10 mm at each boundary (not shown in the figure). We vary the horizon from $\delta = 3\Delta$ to $\delta = 6\Delta$. In (i) and (j) the displacements in x and y are compared with the FE solution.

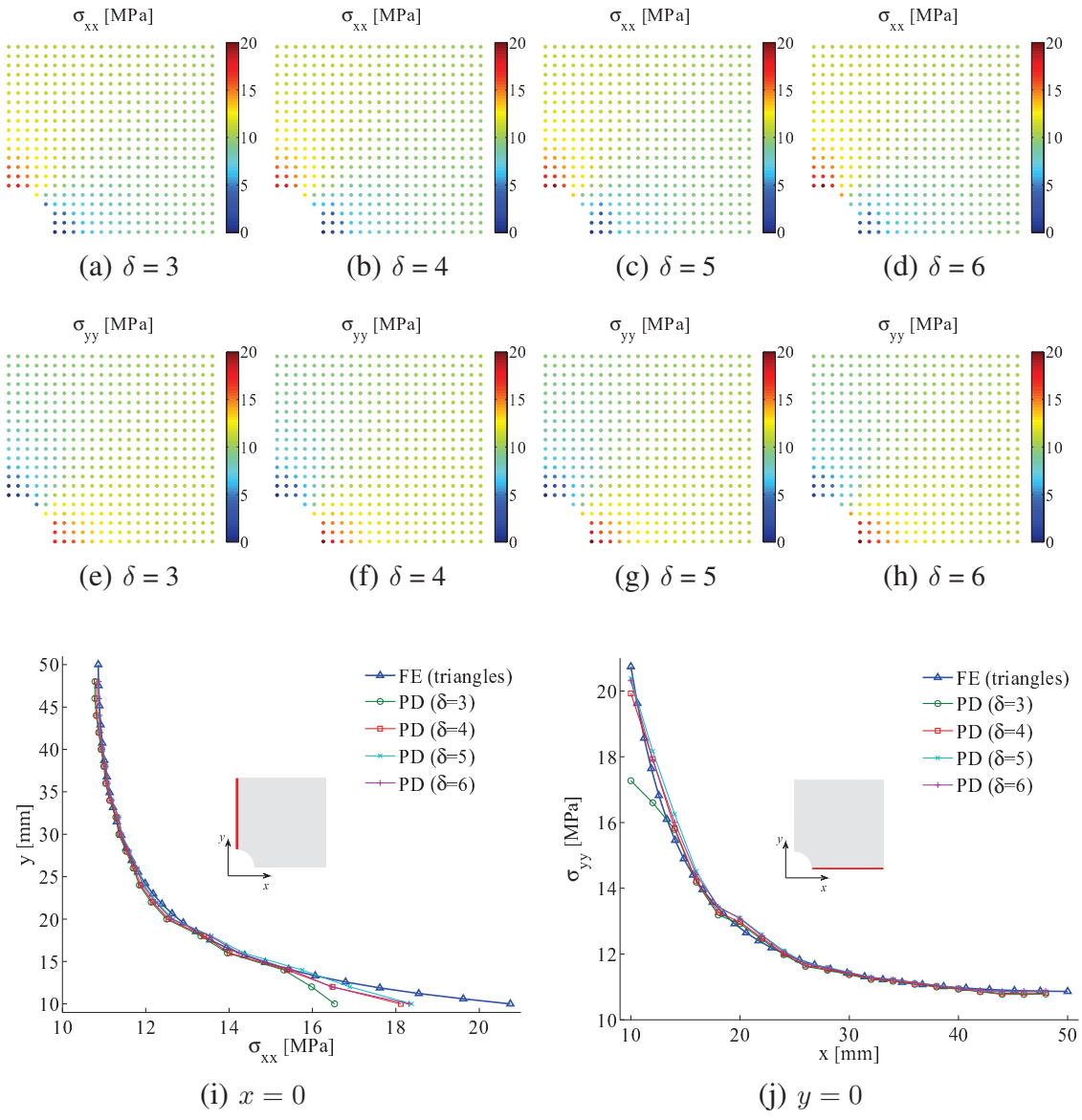

Figura 4.21: PD stresses for the case of the plate with hole and prescribed displacements in both x- and y-direction computed with the 61x61 grid. The extended layers for imposing boundary conditions in the PD model are fixed in 10 mm at each boundary (not shown in the figure). We vary the horizon from $\delta = 3\Delta$ to $\delta = 6\Delta$. In (i) and (j) σ_{xx} and σ_{yy} are compared with the FE solution.

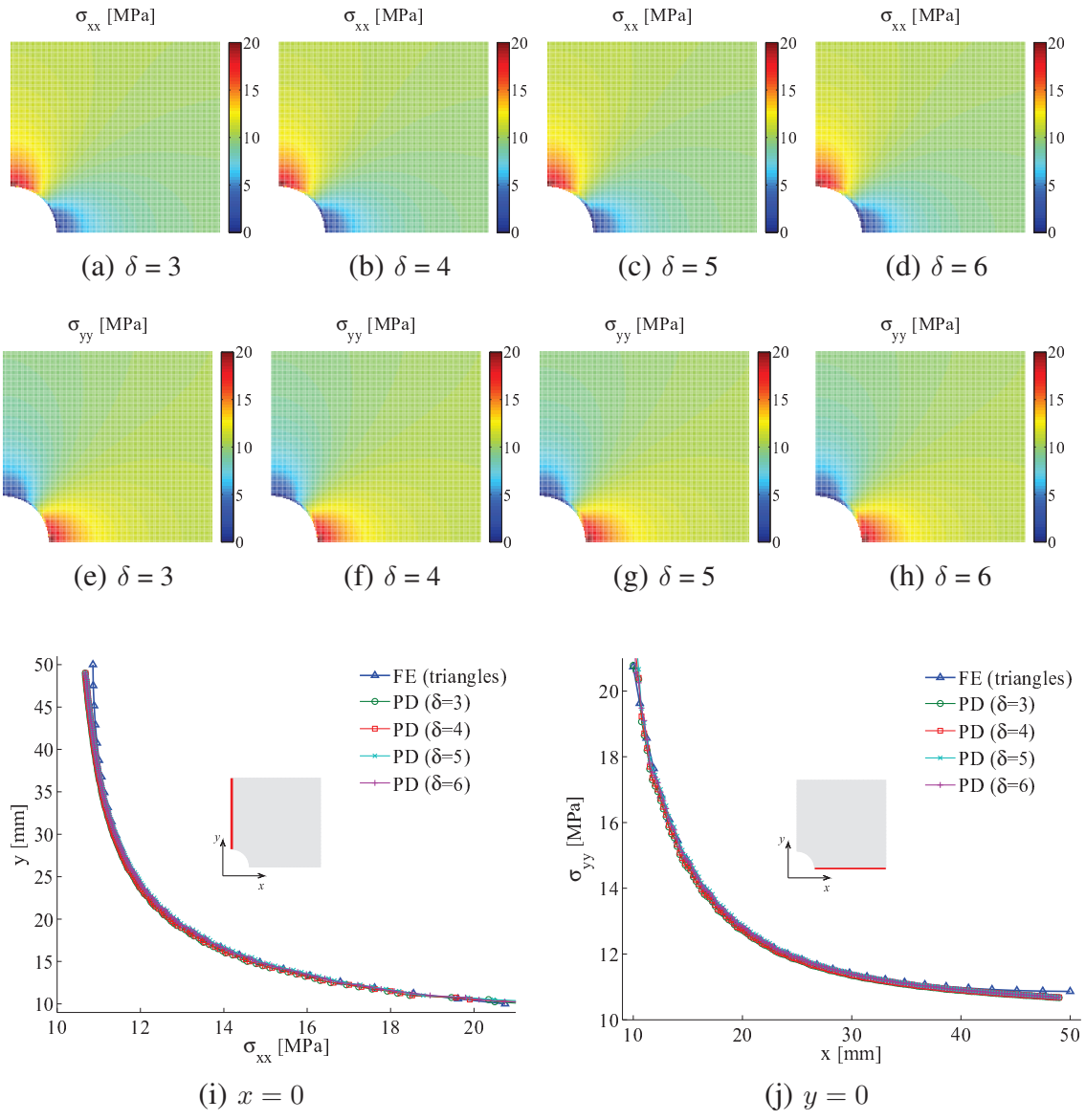

Figura 4.22: PD stresses for the case of the plate with hole and prescribed displacements in both x- and y-direction computed with the 481x481 grid. The extended layers for imposing boundary conditions in the PD model are fixed in 10 mm at each boundary (not shown in the figure). We vary the horizon from $\delta = 3\Delta$ to $\delta = 6\Delta$. In (i) and (j) σ_{xx} and σ_{yy} are compared with the FE solution.

4.3 Remarks

In this chapter, we solved two-dimensional plane stress problems using the PD theory. We adopted the DRM with kinetic damping to simulate the quasi-static loading condition of the problems. The static solution, which is the steady-state part of the transient response of the system, was compared against the FE results. We proposed a methodology to compute the stresses from the PD results and compared with the FE solution. We considered plates with or without hole and prescribed displacements in one and two directions. The effects of grid refinement and the PD horizon were analyzed.

According to the Figures 4.2, 4.6, 4.10 and 4.17, the number of iterations for the DRM to reach converged results increases as the grid gets finer. We also note that the number of iterations did not significantly changed for the cases with or without hole. Regarding to the influence of the horizon size, we did not note a very pronounced difference for small and large values. However, solving for large horizons is more computationally expensive.

The results for both plates with or without hole and prescribed displacements in x- and y-direction are in very good agreement with the FE solution. The models were able to capture the displacement and stress fields with no visible differences when compared to the results from the FEM. The differences between PD and FE are smaller than 0.5%. However, we noted more pronounced differences for the cases with prescribed displacements in only one-direction. As explained in Sections 4.2.1 and 4.2.3, the loss of stiffness of the points near the boundaries is possibly the main reason.

Finally, we shall highlight the importance of correctly applying prescribed displacements in the PD simulations. As it was explained in Chapter 3, Section 3.4, the boundary conditions must be non-locally applied and the size of the extended boundary layers must be at least of one horizon size. In this chapter, this condition is ensured for all horizons that we run by using extended layers

of size 10 mm.

5 COUPLING PERIDYNAMICS AND CLASSICAL ELASTICITY

In this chapter, we present the methodology used for coupling the PD theory and classical continuum mechanics. We propose a scheme via two independent programs. We use LAMMPS for solving the discretized PD domain and a generic FE code for the classical elasticity part. The formulation proposed in (PARKS *et al.*, 2008a), for connecting one-dimensional atomistic-to-continuum, was extended to the PD-to-classical elasticity case in two-dimensions. In the iterative process of the coupled simulation, updated coordinates from one domain are used as boundary conditions to the other. At each FE step, we use the DRM with kinetic damping to obtain the steady-state solution to the PD equations. A wrapper program that links both programs was developed. This approach takes advantage of the fact that LAMMPS provides access to its internal variables without having to change the code (FRANTZDALE *et al.*, 2010). Even though this kind of implementation can cause an overhead in terms of the simulation time, it avoids changes in the existing codes. The output files containing the simulation results are written in $.vtk$ format that can be visualized on open-source visualization applications such as PARAVIEW (www.paraview.org).

In Section 5.1 we introduce the equations of the isoparametric mapping. Then, the alternating Schwarz method and the multiscale wrapper program are presented in Section 5.2. Finally, two numerical experiments are performed in Sections 5.3 and 5.4. In the first experiment, a plate in tension is used to show the convergence of the coupled scheme. In the second, a plate with hole is used to show the promising capabilities of the coupled PD-FE system for predicting damage formation and crack propagation.

5.1 Isoparametric mapping

In this work we consider FE meshes of linear quadrilateral elements. The same type of isoparametric mapping can be applied to any kind of elements in one, two or three dimensions.

The coupling is based on domain decomposition techniques with an overlapping region where both PD and classical continuum subregions coexist. To couple those subregions, the Cartesian coordinates of the PD points embedded in the finite element are mapped onto the standard element. Since the PD grid is generally desired to be finer than the FE one, in the overlapping region it is necessary to interpolate the displacements of the vertices of the finite element to PD points embedded in the element.

The quadrilateral element is defined over the standard domain Γ (Figure 5.1). The mapping is done by the shape functions of the element which are defined in the standard element Γ. The functions $\mathbf{x}(\boldsymbol{\xi})$ that maps Γ onto $\Omega^{(e)}$, for the 4-node quadrilateral element, are given by

$$\mathbf{x}(\boldsymbol{\xi}) = \sum_{i=1}^{4} N_i(\boldsymbol{\xi})\mathbf{x}^i, \tag{5.1}$$

or, in component form,

$$x(\xi,\eta) = \sum_{i=1}^{4} N_i(\xi,\eta)x^i, \tag{5.2}$$

$$y(\xi,\eta) = \sum_{i=1}^{4} N_i(\xi,\eta)y^i, \tag{5.3}$$

where $\mathbf{x}^i = (x^i, y^i)$ are the vertex coordinates.

The bi-linear quadrilateral element has the following shape functions:

$$\begin{aligned} N_1(\xi,\eta) &= \tfrac{1}{4}(1-\xi)(1-\eta), \\ N_2(\xi,\eta) &= \tfrac{1}{4}(1+\xi)(1-\eta), \\ N_3(\xi,\eta) &= \tfrac{1}{4}(1+\xi)(1+\eta), \\ N_4(\xi,\eta) &= \tfrac{1}{4}(1+\xi)(1+\eta). \end{aligned} \tag{5.4}$$

The embedded PD points for all elements in the overlapping region are determined when the simulation is set. We than solve the FE problem and use the updated coordinates of the nodes

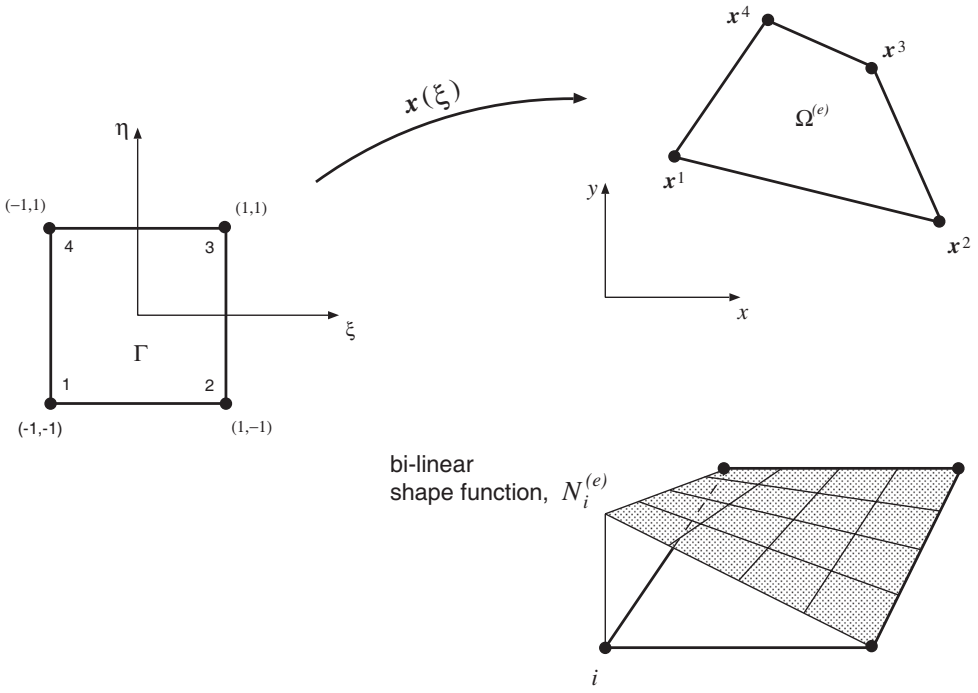

Figura 5.1: Bi-linear quadrilateral (DE SOUZA NETO *et al.*, 2011).

as prescribed positions to the PD points. When the PD grid is finer than the FE one, the FE shape functions are used to interpolate the displacements of the four nodes of the element to the embedded PD points.

5.2 Coupling LAMMPS to a finite element code

The simplest way to simulate a multiscale model using single-scale components is to invoke them independently as stand-alone applications from a multiscale wrapper program (FRANTZDALE *et al.*, 2010). LAMMPS is designed to allow it to be coupled to other codes. Once LAMMPS is built as a library, the interface with LAMMPS can be done either via C, C++, Fortran, or Python. The `run` command in LAMMPS has options that allow it to be invoked with minimal overhead (no setup or clean-up) if multiple short runs is required (PLIMPTON, 1995, PLIMPTON, 2013). This is our case where LAMMPS is driven by another program and it is called several times until

convergence is reached. LAMMPS provides a package to facilitate the interfacing process with examples of wrapper programs in C and C++. We chose C++ because it is the language that our FE library is implemented in.

5.2.1 Alternating Schwarz method and the multiscale wrapper program

The developed wrapper program to link and call both LAMMPS and the FE library is based on the templates available in the package "couple" provided with LAMMPS. At the moment we have the serial version of the wrapper program only. This fact reduces our computational capabilities to simulating large problems. Yet it is enough for studying different coupling approaches.

We apply the alternating Schwarz method for connecting PD and FE. In (PARKS *et al.*, 2008a), the authors applied the same technique for coupling FE and MD. The main limitation of this approach is that its convergence is usually slow. However, the computational infrastructure developed during this work make it possible that other strategies to be implemented with a few changes in the codes. The alternating Schwarz algorithm reads:

1. Initialize PD and FE grids.
2. **while** not converged **do**
3. Fix positions of FE nodes according to positions of PD points.
4. Solve for displacements of unconstrained FE nodes (static problem).
5. Fix positions of PD points according to positions of FE nodes.
6. Solve for displacements of unconstrained PD points (using DRM).
7. **end while**

As explained before the coupling procedure is straightforward. First the wrapper program initializes an instance of LAMMPS given the input file. The coordinates of the PD points are then used by the FE library to identify the points in the overlapping zone. For each element belonging to the overlapping zone the embedded PD points are stored. There is no limitation in the number of PD points embedded in an element. A mapping function in the FE library maps the coordinates of each embedded PD point in the global reference system to the standard element domain (Figure 5.1). Thus, for each element in the overlapping region, the program searches for the PD points inside that element and maps those points to the standard element, as explained in the Section 5.1.

The wrapper program uses the PD points positions as boundary conditions on the FE nodes. The red squares in Figure 5.2(b) indicate the FE nodes that have prescribed displacement depending on the position of the PD points. At the first time step the prescribed displacement on those nodes is zero and we solve the FE problem. The wrapper program uses the updated coordinates of the FE nodes in the overlapping region to computed the new coordinates of the PD points in that region. The PD points with blue circles in Figure 5.2(b) are the points where the updated coordinates are prescribed. Those points are fixed in the new position and LAMMPS then is called to solve for the unconstrained PD points. The multiscale wrapper wait for the LAMMPS job to complete and continue on with the acquired displacements. This process is repeated until convergence is reached.

5.3 Test problem 1 - plate under uniaxial tension

The problem shown in Figure 5.2(a) was used to test the implementation. The plate was discretized in such a way that we have a PD region in the center of the domain and a FE mesh surrounding it. There is an overlapping zone where both PD and classical elasticity equations are solved. Figure 5.2(b) shows the plate discretized into FE elements and PD points.

Figure 5.2(b) also highlights the PD points that receive the displacements from the FE solution (blue circles) and the FE nodes that receive the displacements from the PD solver (red squares).

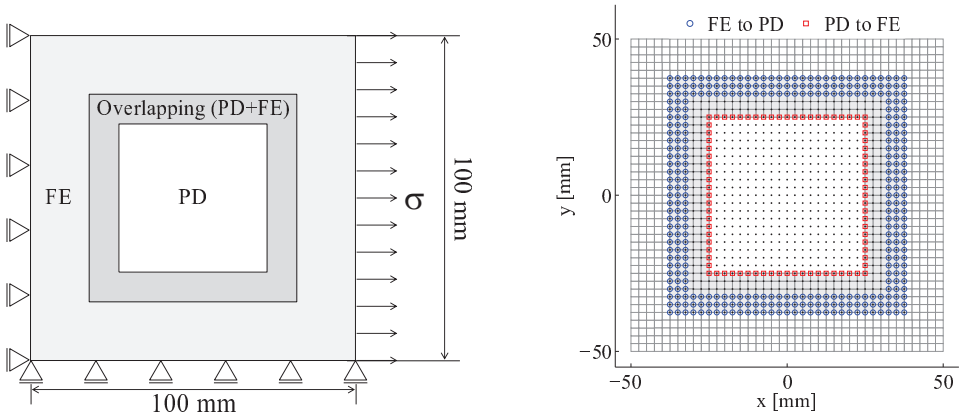

(a) Plate loaded in tension (b) Numerical model

Figura 5.2: Plate under uniaxial tension with Dirichlet boundary conditions and the numerical model used in the coupled FE/PD simulation. In (a) we detail the FE, PD and the region of overlapping between the two regions. In (b) the problem is discretized into quadrilateral elements and PD nodes. The nodes that exchange boundary conditions are also shown in (b).

5.3.1 Numerical experiments

Numerical experiments were performed to study the convergence of the coupled scheme. Three FE meshes with overlapping regions of three different sizes were used. Table 5.1 gives the details of the FE meshes used. We refer to the size of overlapping region according to the number of element layers beginning from the inner part of the domain. The number of layers used was four, five and six. Figure 5.3 shows all meshes with all three different sizes of the overlapping region.

For the PD part we consider three different cases. According to the way that the PD region is discretized we have 4, 9 and 36 PD embedded points in each element of the overlapping region. The cases are shown in Figure 5.4. The PD horizon used is $\delta = 3$.

We have 27 experiments in total. Table 5.2 summarizes the parameters for all tested cases. The table details the number of PD points in the overlapping region for all tested cases.

Material properties for both FE and PD domains are: elastic modulus 72.0 GPa and Poisson's

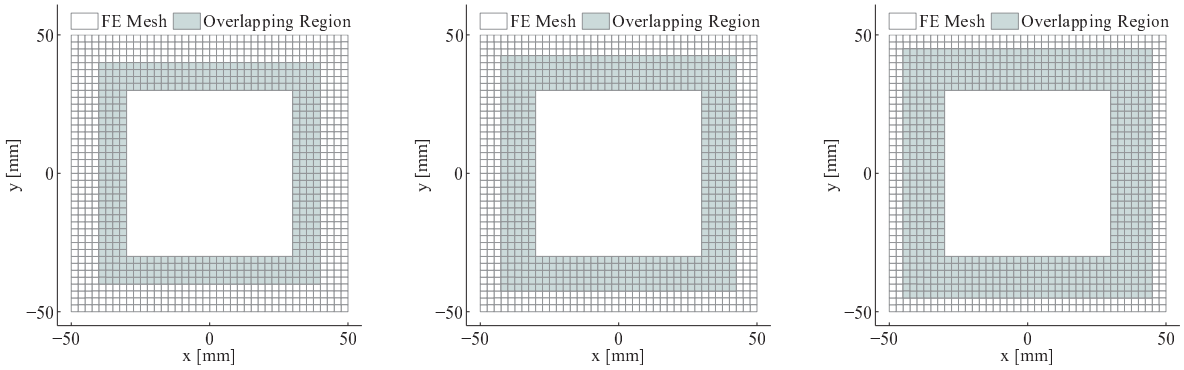

(a) Mesh 1 (4 layers). (b) Mesh 1 (5 layers). (c) Mesh 1 (6 layers).

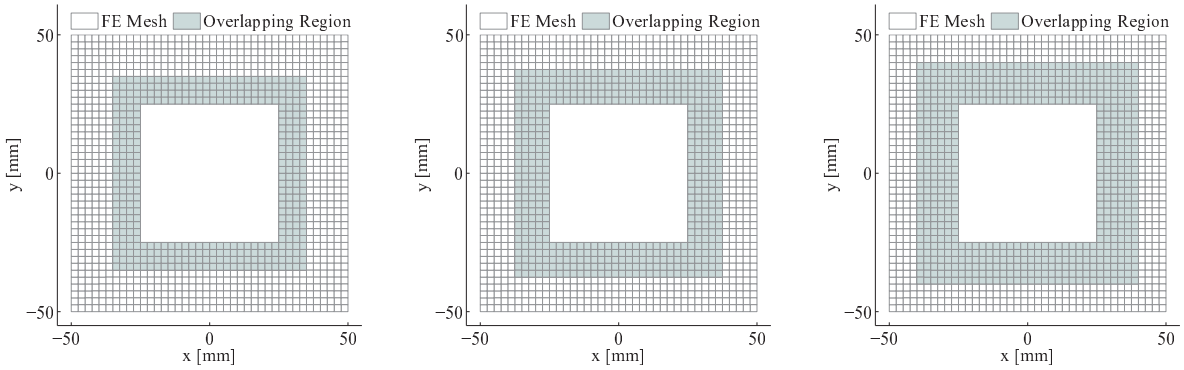

(d) Mesh 2 (4 layers). (e) Mesh 2 (5 layers). (f) Mesh 2 (6 layers).

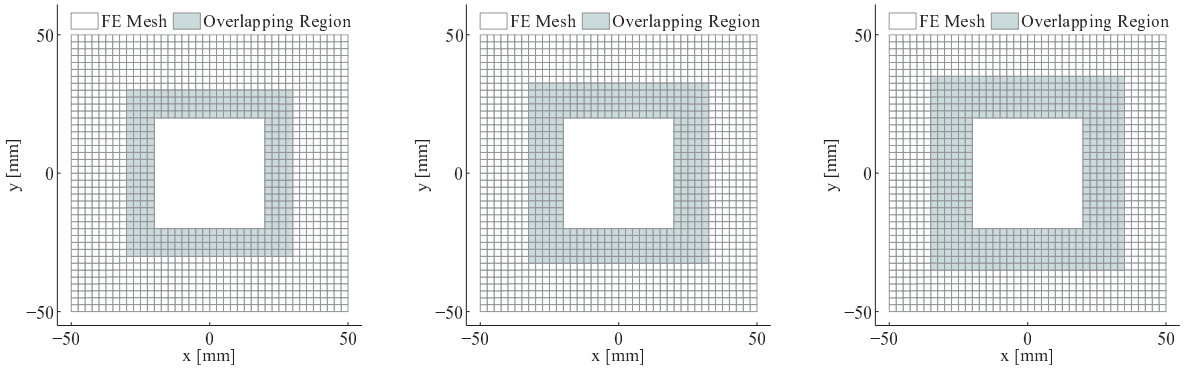

(g) Mesh 3 (4 layers). (h) Mesh 3 (5 layers). (i) Mesh 3 (6 layers).

Figura 5.3: FE meshes used in the coupled PD/FE simulations. The colored elements represent the overlapping region (Table 5.1 details the number of elements in each mesh).

Tabela 5.1: Parameters of the FE meshes for the numerical experiments of the coupled FE/PD simulation. The table shows the number of elements in the overlapping region according to the size of the region.

FE Mesh	No. of Elements	No. of Nodes	Size of the Overlapping Region (Layers)	No. of Elements in the Overlapping Region
1	1024	1152	4	448
			5	580
			6	720
2	1200	1320	4	384
			5	500
			6	624
3	1344	1456	4	320
			5	420
			6	528

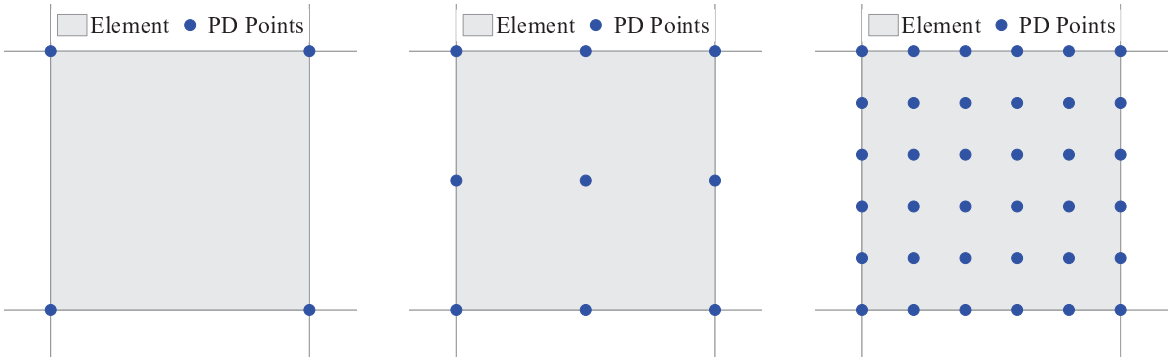

(a) 4 embedded points. (b) 9 embedded points. (c) 36 embedded points.

Figura 5.4: Detail of the PD embedded nodes in the element for the three considered schemes.

Tabela 5.2: Parameters of the PD grids for the numerical experiments of the coupled PD/FE simulation (for each FE mesh shown in Table 5.1 and Figure 5.3).

FE Mesh	Size of Overlapping Region (No. of Element layers)	PD Region [mm]	No. PD Points in each direction	No. PD Points (Total)	No. PD Points (Over-lapping Region)	No. PD Points (FE to PD Region)	No. PD Points (PD to FE Region)	No. PD Embedded Points
Mesh 1 (1024 Elements)	4	[-40.0 40.0]	33 x 33	1,089	560	360	96	4
			65 x 65	4,225	2,016	1,200	192	9
			161 x 161	25,921	11,760	6,600	480	36
	5	[-42.5 42.5]	35 x 35	1,225	696	384	96	4
			69 x 69	4,761	2,552	1,280	192	9
			171 x 171	29,241	15,080	7,040	480	36
	6	[-45.0 45.0]	37 x 37	1,369	840	408	96	4
			73 x 73	5,329	3,120	1,360	192	9
			181 x 181	32,761	18,600	7,480	480	36
Mesh 2 (1200 Elements)	4	[-35.0 35.0]	29 x 29	841	480	312	80	4
			57 x 57	3,249	1,728	1,040	160	9
			141 x 141	19,881	10,080	5,720	400	36
	5	[-37.5 37.5]	31 x 31	961	600	336	80	4
			61 x 61	3,721	2,200	1,120	160	9
			151 x 151	22,801	13,000	6,160	400	36
	6	[-40.0 40.0]	33 x 33	1,089	728	360	80	4
			65 x 65	4,225	2,704	1,200	160	9
			161 x 161	25,921	16,120	6,600	400	36
Mesh 3 (1344 Elements)	4	[-30.0 30.0]	25 x 25	625	400	264	64	4
			49 x 49	2,401	1,440	880	128	9
			121 x 121	14,641	8,400	4,840	320	36
	5	[-32.5 32.5]	27 x 27	729	504	288	64	4
			53 x 53	2,809	1,848	960	128	9
			131 x 131	17,161	10,920	5,280	320	36
	6	[-35.0 35.0]	29 x 29	841	616	312	64	4
			57 x 57	3,249	2, 288	1,040	128	9
			141 x 141	19,881	13,640	5,720	320	36

ratio 1/3. As it was explained in Section 5.2.1, we solve a FE static problem and then call LAMMPS to solve the PD problem using DRM. Based on the results from Chapter 4, after each solution of the FE static problem, we call LAMMPS to solve the PD problem and use 100 dynamic relaxation steps before apply the updated coordinates of the PD points to the FE nodes. In the following, we solve the FE static problem 100 times which results in 10,000 dynamic relaxation steps.

5.3.2 Results

In Figure 5.5 we show the displacement profile for the case with FE mesh 2 (1200 elements), with overlapping region of 5 layers and PD grid 61x61 for different iteration steps. This case results in 9 embedded PD points in each element (see Table 5.2). The displacement profiles are linear as expected (we observed a similar behavior for all 27 cases and based on that the other displacement profiles are not show). In the overlapping region the displacement from FE and PD matches well, in other words, there is no discontinuity in the displacement field between the domains.

No convergence criterion was implemented for this example. As it was said before, we ran 100 FE steps and for each step we let the PD solver to iterate 100 times. For each PD step we computed the Euclidean norm of the displacement vector. In Figure 5.6 we show the difference in the norms between two consecutive time steps.

From Figure 5.6 the worst case is the one having the smallest overlapping region with the lowest number of finite elements. On the other hand, the convergence gets better as the FE mesh as well as the size of the overlapping region increase. We can also notice that the convergence ratio is influenced by two different situations: the size of the overlapping region and the number of PD points in the finite element.

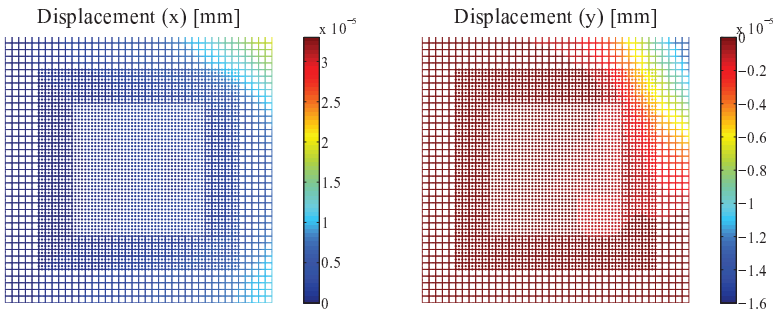

(a) FE step 1

(b) FE step 1

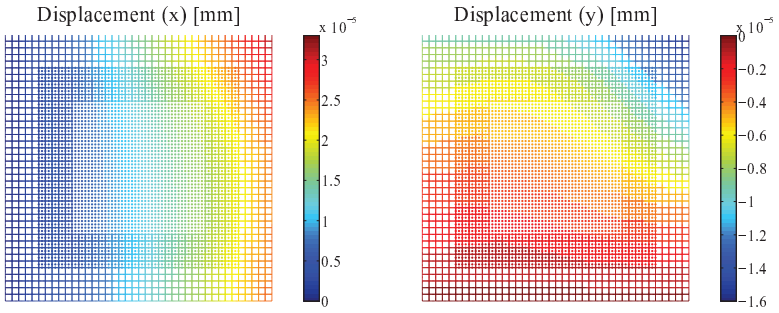

(c) FE step 15

(d) FE step 15

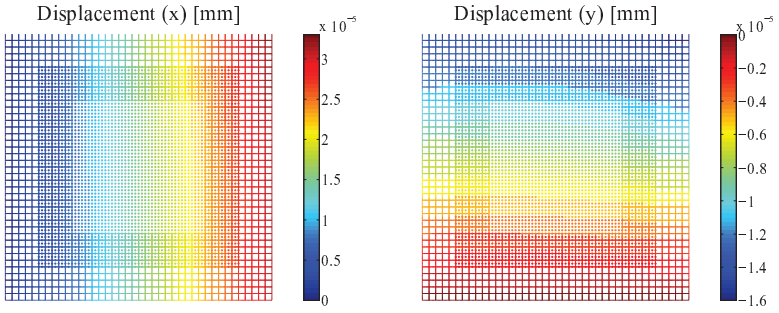

(e) FE step 35

(f) FE step 35

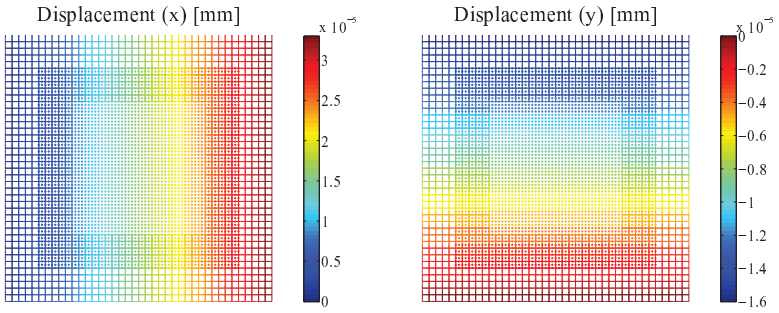

(g) FE step 75

(h) FE step 75

Figura 5.5: Displacement distribution for the case of the plate under uniaxial tension using FE Mesh 2 (1200 elements) with a overlapping region of 5 layers using PD grid (61 x 61); see Table 5.2.

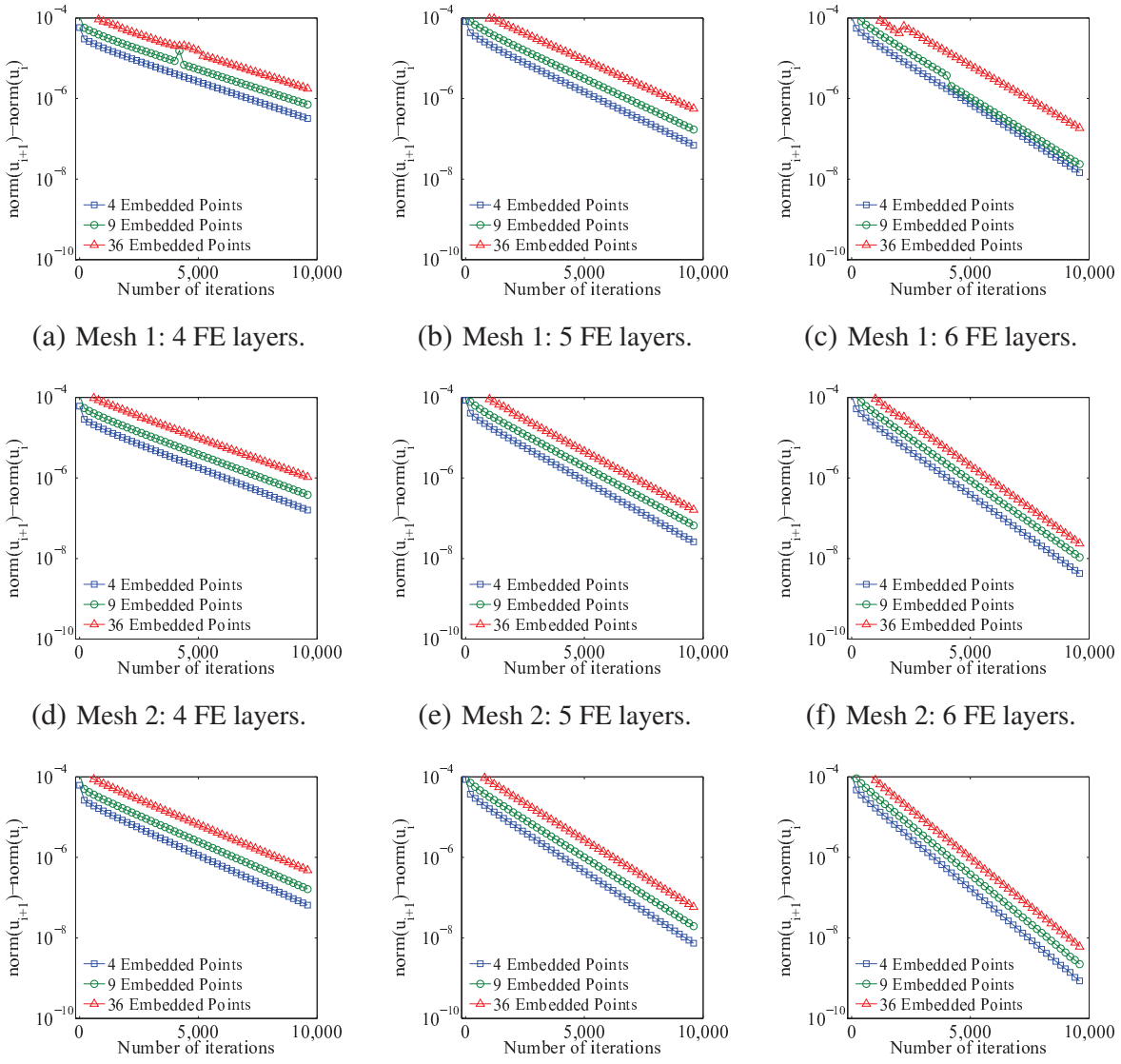

(a) Mesh 1: 4 FE layers. (b) Mesh 1: 5 FE layers. (c) Mesh 1: 6 FE layers.

(d) Mesh 2: 4 FE layers. (e) Mesh 2: 5 FE layers. (f) Mesh 2: 6 FE layers.

(g) Mesh 3: 4 FE layers. (h) Mesh 3: 5 FE layers. (i) Mesh 3: 6 FE layers.

Figura 5.6: Difference in the Euclidean norm between two consecutive steps for the PD domain in the PD/FE solution of the plate under uniaxial tension.

5.4 Test problem 2 - Brittle fracture in a plate loaded in tension

Consider the plate with hole shown in Figure 5.7 loaded in tension by a traction σ whithout any displacement constraints. We define a PD region in the center of the domain and a FE mesh surrounding it. In the overlapping zone, both PD and classical elasticity equations are solved. In order to circumvent premature failure due to high local displacement gradients, damage is allowed only in the PD region of size 25mmx25mm delimited by the dashed line. We use the FE Mesh 1 (1024 elements) with five layers of overlapping (Figure 5.3(b)). The PD grids were chosen such that 9 and 36 points were embedded in the elements; see Table 5.2 for more details.

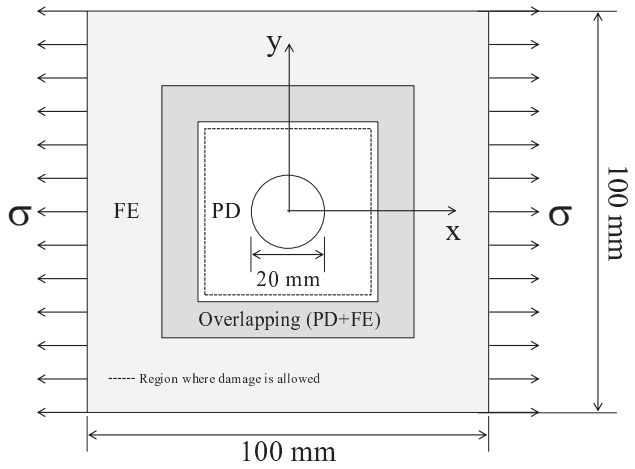

Figura 5.7: Plate with hole under uniaxial tension used in the coupled FE/PD simulation with damage. It is shown the details of the FE, PD and the region of overlapping between the two regions. Damage is allowed in the PD region delimited by the dashed line.

In Chapter 4, the validity of the PD predictions for a plate with hole were established in the absence of failure and the steady-state displacements were compared against the FE solutions. In this section, the plate with hole is investigated for failure prediction. Most experiments involving failure are performed under quasi-static conditions (KILIC, 2008). The loading rate might significantly affect the failure patterns since the dynamic problems locally reach higher displacement gradients than under quasi-static conditions because of the traveling elastic waves.

As it is shown in (SILLING AND ASKARI, 2005), the critical stretch for bond failure, s_0, can be related to the energy release rate G_0 and is given by

$$s_0 = \sqrt{\frac{10G_0}{\pi c_{2,\delta}\delta^5}}, \tag{5.5}$$

where δ is the horizon and the constant $c_{2,\delta}$ is defined in Equation (3.10) by $c_{2,\delta} = \frac{72K}{5\pi\delta^3}$. The energy release rate is the work required to completely separate the two halves of a body across the fracture surface. For this, it is necessary breaking all the bonds that are initially connected in the opposite halves. The parameters used in the simulation were: elastic modulus = 72.0 GPa, Poisson's ratio = 1/3 and G_0 = 135.0 J/m^2.

Figures 5.8 and 5.9 show the displacement profiles and the resulting damage pattern for the two simulations performed in this section. As expected, the cracks initiate at the hole near high deformation areas. The cracks then propagate towards the edges of the plate as shown in Figures 5.8(g) to 5.8(i) and 5.9(g) to 5.9(i).

We note that the damage patterns for the two tested cases in this section are slightly different. While for the case with 9 embedded PD points we observe a straight line from the hole towards the edge of the domain, for the case with 36 embedded points there are two parallel lines towards the edge. A reason for this result is possibility the difference in the geometry representation of the two PD grids. Figure 5.10 shows a zoom in the region of the hole for the two grids. For some reason, the small difference in the geometry of the hole resulting from the two grids might make the damage patterns a bit different.

5.5 Remarks

In this chapter, we presented the methodology used for coupling the PD theory and continuum mechanics. The MD program LAMMPS from Sandia National Laboratories was used for solving

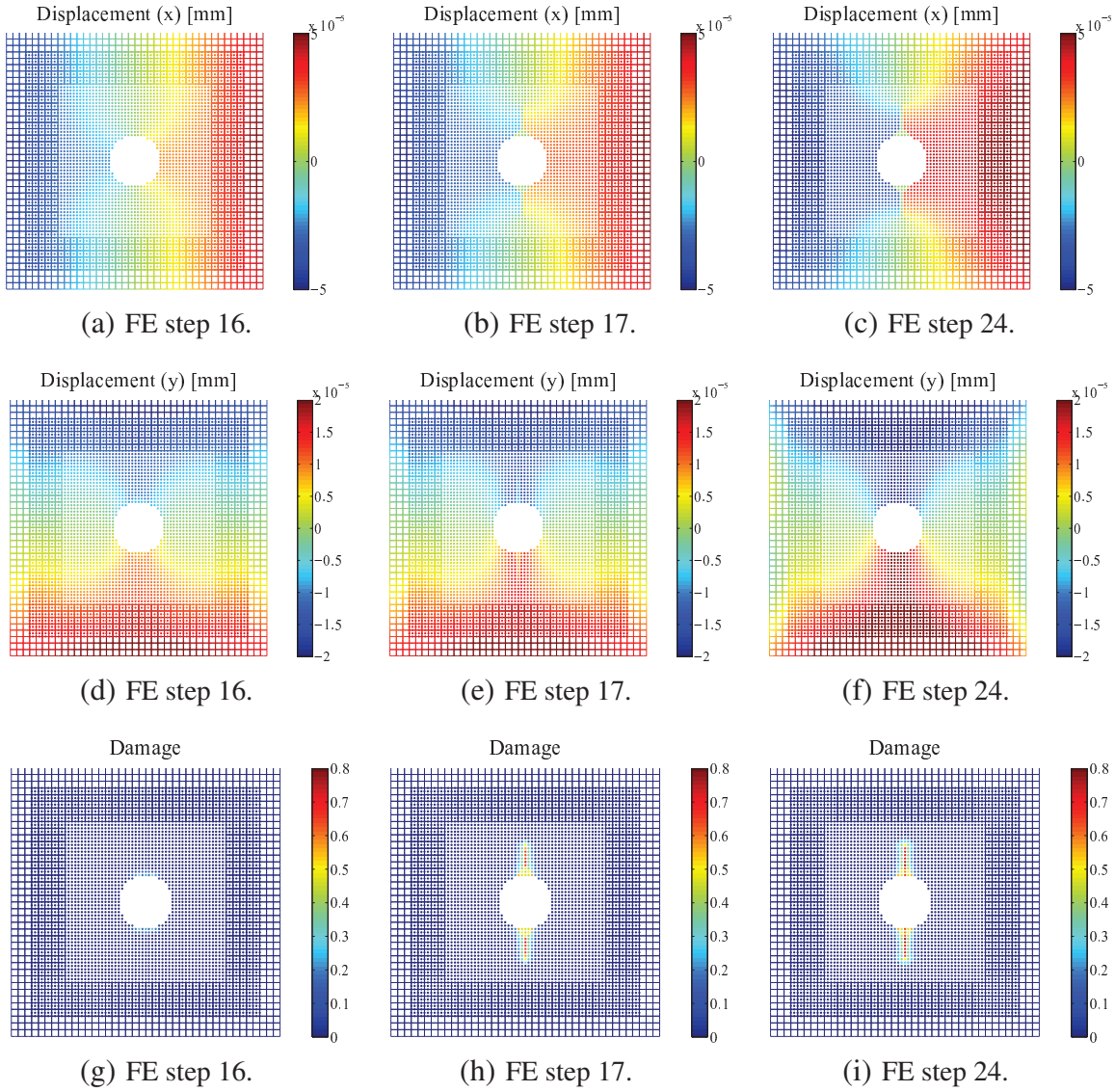

(a) FE step 16. (b) FE step 17. (c) FE step 24.

(d) FE step 16. (e) FE step 17. (f) FE step 24.

(g) FE step 16. (h) FE step 17. (i) FE step 24.

Figura 5.8: Results for the plate with hole with damage allowed in the PD region. FE Mesh 1 (1024 elements) with a overlapping region of 5 layers was used. The PD discretization results in 9 points embedded in the FE elements of the overlapping region. In (a) to (f) are shown the displacements in x- and y-direction. The damage maps are shown in (g) to (i).

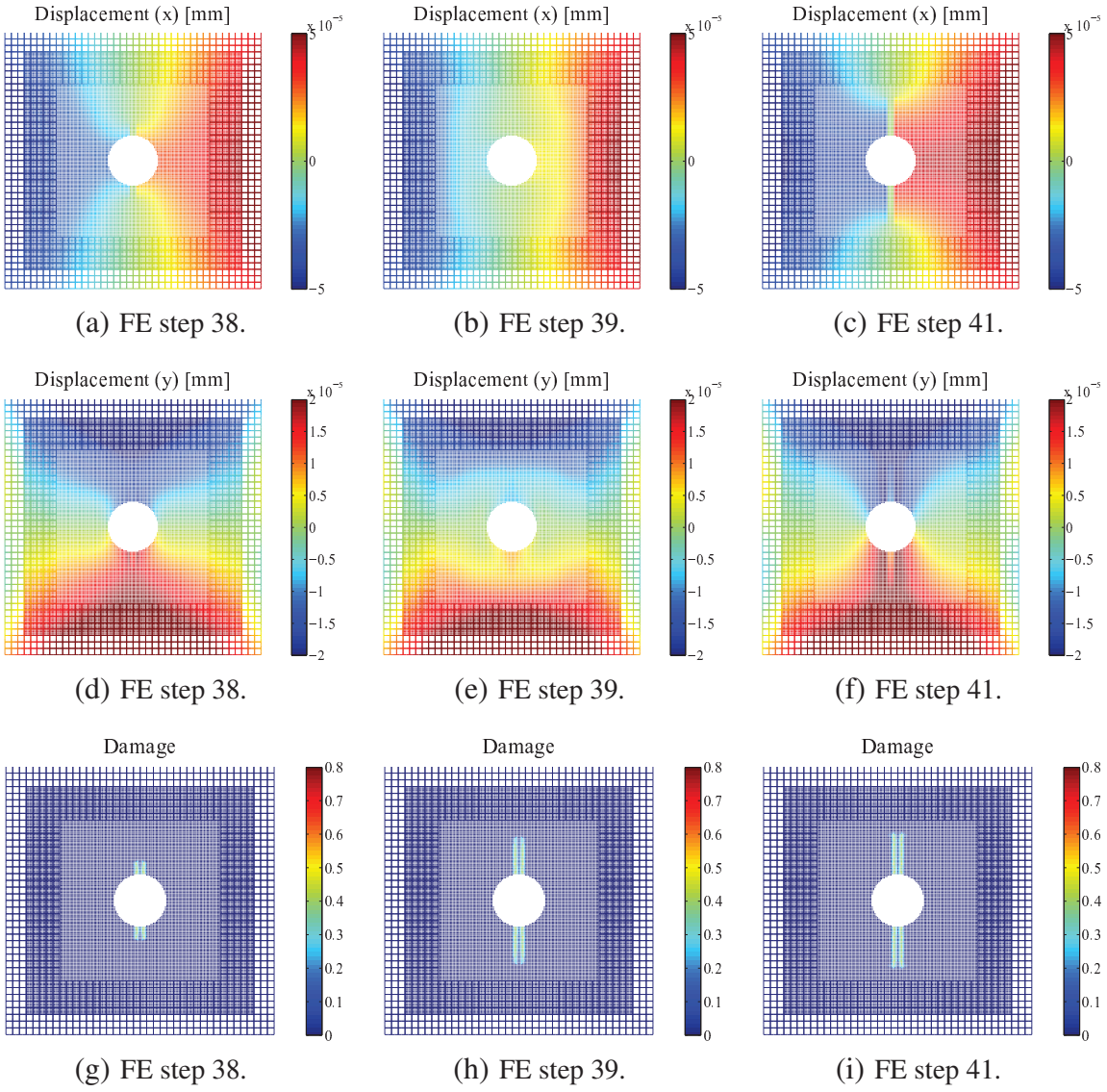

(a) FE step 38. (b) FE step 39. (c) FE step 41.

(d) FE step 38. (e) FE step 39. (f) FE step 41.

(g) FE step 38. (h) FE step 39. (i) FE step 41.

Figura 5.9: Results for the plate with hole with damage allowed in the PD region. FE Mesh 1 (1024 elements) with a overlapping region of 5 layers was used. The PD discretization results in 36 points embedded in the FE elements of the overlapping region. In (a) to (f) are shown the displacements in x- and y-direction. The damage maps are shown in (g) to (i).

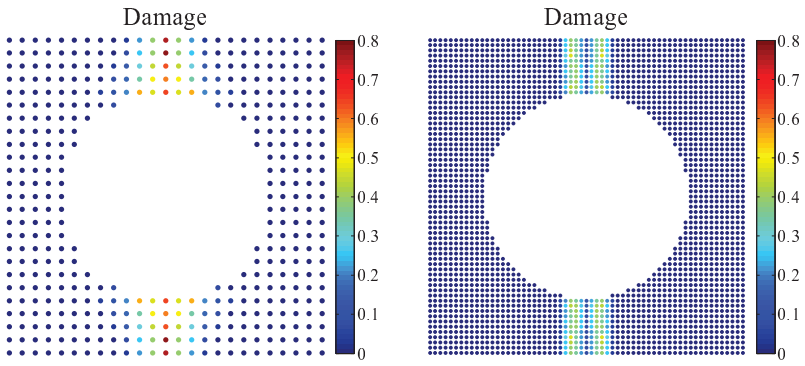

(a) 9 embedded PD points. (b) 36 embedded PD points.

Figura 5.10: Zoom in the region surrounding the hole.

the discretized PD domain and a generic FE code for the continuum part. A wrapper program that links both programs was developed. A plate was used to test the implementation and brittle fracture was predicted using a plate with hole was used.

Different FE meshes and PD grids were used resulting in schemes with 4, 9 and 36 PD embedded points in each element of the overlapping region. We observed that the convergence gets better as the FE mesh as well as the size of the overlapping region increase. We also noted that the number of PD points embedded in the finite element also plays a role in the convergence process. However, this is possibly an effect of grid refinement which increases the number of iterations to reach convergence, and not the fact of having more nodes inside the element.

Finally, a plate with hole was used for failure prediction using the coupled approach PD/FE. As expected, the cracks initiate near the hole in the high deformation areas.

6 FINAL REMARKS AND FUTURE WORK

We presented a study of some aspects of the discretized peridynamic theory focusing on the details that we consider important for multiscale simulation of engineering problems using peridynamics and finite elements.

First the peridynamic theory in one dimension was studied in details focusing on the application of Dirichlet boundary conditions. Then, two-dimensional plane stress problems in plates with and without hole were considered. We proposed a methodology to post-processing the peridynamic results in order to estimate stresses in the material. Moreover, the dynamic relaxation method with kinetic damping was used to obtain the steady-state solutions of the peridynamic equations. The simulations indicated good agreement between the peridynamic and finite element static solutions.

Although the peridynamic theory is effective for damage prediction, it is computationally more expensive to solve the discretized peridynamic equations than the finite element ones. Hence, we coupled these methods aiming to using peridynamics where damage is expected and the classical continuum mechanics in the remaining areas. We developed a wrapper program to couple the molecular dynamics program LAMMPS to a finite element library. We used the expression in terms of the critical energy release rate, derived in (SILLING AND ASKARI, 2005), for determining the critical bond stretch. Thus, the coupled scheme peridynamics/finite element was used to predict damage in a plate with hole under tension load. The pattern of the cracking agreed with the expected results.

Peridynamics is a very active research area which still requires more development. One of the limitations is the number of materials models available. However, different models have recently been proposed in the literature such as a new constitutive model for a linearly elastic material (AGUIAR AND FOSDICK, 2013) and a also viscoelastic models (WECKNER *et al.*, 2013). The coupling of the theory to other traditional numerical methods has also been theme of recent publi-

cations (WILDMAN AND GAZONAS, 2013a; WILDMAN AND GAZONAS, 2013b). Sandia National Laboratories developed, and released in the end of last year, a new peridynamic software capable of using finite element meshes for generating peridynamic models (PARKS *et al.*, 2012). Our research group at Unicamp has interest in different aspects of the theory including:

- Development of new peridynamic material models especially hyperelastic materials capable to reproduce the mechanical behavior of traditional models of classical continuum mechanics;
- Application of different techniques to the coupling of the peridynamics to traditional numerical methods such as the finite element methods;
- High performance computing applied to peridynamics and finite elements;
- Application of the peridynamics to the study of cracking in brittle and ductile materials as well as tearing of hyperelastic materials.

Finally, peridynamics is a promising theory that is formulated using integral equations and the derivatives of the displacements do not appear in the formulation. Hence, the peridynamic equations are valid even in regions of displacement discontinuities. In contrast to material response in the classical continuum mechanics, the response function may also includes material failure. Thus, the cracks can initiate and propagate at multiple regions with arbitrary paths. However, the theory is recent and requires more development.

A APPENDIX A. LAMMPS INPUT FILES

A.1 Plates with prescribed displacements in x

```
## Two-dimensional PD model: plate with prescribed displacement in x
# MATERIAL PROPERTIES
variable myDensity equal 2440               # Density of the Material
variable myE equal 72e9                     # Elastic modulus
variable myP equal (1.0/3.0)                # Poisson's ratio
variable myK equal ${myE}/(3*(1-2*${myP}))  # Bulk modulus
variable pi equal 3.14159265358979323846    # constant, but define it as a variable here
# MESH (GRID)
variable npts equal 50          # PD No. of points in each direction
variable h equal (1.0/${npts})  # PD grid spacing
variable delta equal 3.05*${h}  # Peridynamic horizon
# LAMMPS PARAMETERS
dimension   2d
units       si
boundary    s s p
atom_style  peri
atom_modify map array
variable    myskin equal 2.0*${h}
neighbor    ${myskin} bin
lattice     sq ${h}
# GEOMETRY DEFINITION
variable X1 equal 0.601
variable X2 equal 0.601
variable X3 equal ${h}
variable myxmin equal -${X1}
variable myxmax equal ${X2}
variable myymin equal -${X1}
variable myymax equal ${X2}
variable myzmin equal 0.0
variable myzmax equal ${X3}
region Plate block &
${myxmin} ${myxmax} ${myymin} ${myymax} ${myzmin} ${myzmax} &
units box
create_box 3 Plate
# CREATE ATOMS
create_atoms 1 region Plate
# DEFINE REGIONS FOR IMPOSING BC
variable    t11x equal (${myxmax}-(1+(0.1/${h})))*${h})
region      RgBCR block &
            ${t11x} ${myxmax} -INF INF -INF INF &
units box
region      RgBCL block &
            -${myxmax} -${t11x} -INF INF -INF INF &
units box
set region RgBCR type 2
set region RgBCL type 3
# PERIDYNAMICS
pair_style      peri/pmb_dr
variable        mydelta equal (${delta}+(${delta}/1000.0))
variable        myc equal ((72.0*${myK})/(5.0*${pi}*(${delta}^3)))
pair_coeff      * * ${myc} ${mydelta} 1000 0.250
# GROUPS
group GrPlate region Plate
group GrBCR region RgBCR
group GrBCL region RgBCL
group GrBulk subtract GrPlate GrBCR GrBCL
# SETS
set group       all density ${myDensity}
variable        myVolume equal ($h)^2
```

```
set group       all volume ${myVolume}
# DEFINE CYLINDER (Take the next two lines off for the case without the hole)
region cyld_in cylinder z 0 0 0.098 0 0 units box
delete_atoms region cyld_in compress no
# TIME INTEGRATION
fix         Fnve all nve_dr
variable    mystep index 1.0
timestep    ${mystep}
# DEFINE COMPUTES
compute C2 all displace/atom # Compute displacement for each particle
# RESULTS
thermo  10
dump    1 all custom 10 dump_file id type x y z c_C2[1] c_C2[2]
run     1
# PRESCRIBED DISPLACEMENTS
variable DispMin equal (-${X1}*0.000100)
variable DispMax equal (${X2}*0.000100)
displace_atoms GrBCR ramp x ${DispMin} ${DispMax} x -${X1} ${X2} units box
displace_atoms GrBCL ramp x ${DispMin} ${DispMax} x -${X1} ${X2} units box
displace_atoms all move NULL NULL 0.0 units box
# SET FORCE TO ZERO
fix FxAll all setforce NULL NULL 0.0
fix FxBC1 GrBCR setforce 0.0 NULL 0.0
fix FxBC2 GrBCL setforce 0.0 NULL 0.0
run 1000
```

A.2 Plates with prescribed displacements in x and y

```
## Two-dimensional PD model: plate with prescribed displacement in x and y
# MATERIAL PROPERTIES
variable myDensity equal 2440              # Density of the Material
variable myE equal 72e9                    # Elastic modulus
variable myP equal (1.0/3.0)               # Poisson's ratio
variable myK equal ${myE}/(3*(1-2*${myP}))  # Bulk modulus
variable pi equal 3.14159265358979323846    # constant, but define it as a variable here
# MESH (GRID)
variable npts equal 50          # PD No. of points in each direction
variable h equal (1.0/${npts})  # PD grid spacing
variable delta equal 3.05*${h}  # Peridynamic horizon
# LAMMPS PARAMETERS
dimension   2d
units       si
boundary    s s p
atom_style  peri
atom_modify map array
variable    myskin equal 2.0*${h}
neighbor    ${myskin} bin
lattice     sq ${h}
# GEOMETRY DEFINITION
variable X1 equal 0.601
variable X2 equal 0.601
variable X3 equal ${h}
variable myxmin equal -${X1}
variable myxmax equal ${X2}
variable myymin equal -${X1}
variable myymax equal ${X2}
variable myzmin equal 0.0
variable myzmax equal ${X3}
region Plate block &
${myxmin} ${myxmax} ${myymin} ${myymax} ${myzmin} ${myzmax} &
units box
create_box 5 Plate
# CREATE ATOMS
create_atoms 1 region Plate
# DEFINE REGIONS FOR IMPOSING BC
variable    t11x equal (${myxmax}-(1+(0.1/${h}))*${h})
region      RgBCR block &
            ${t11x} ${myxmax} -INF INF -INF INF &
units box
region      RgBCL block &
            -${myxmax} -${t11x} -INF INF -INF INF &
units box
region      RgBCU block &
            -INF INF ${t11x} ${myymax} -INF INF &
units box
region      RgBCB block &
            -INF INF -${myymax} -${t11x} -INF INF &
units box
set region RgBCR type 2
set region RgBCL type 3
set region RgBCU type 4
set region RgBCB type 5
# PERIDYNAMICS
pair_style      peri/pmb_dr
variable        mydelta equal (${delta}+(${delta}/1000.0))
variable        myc equal ((72.0*${myK})/(5.0*${pi}*(${delta}^3)))
pair_coeff      * * ${myc} ${mydelta} 1000 0.250
```

```
# GROUPS
group GrPlate region Plate
group GrBCR region RgBCR
group GrBCL region RgBCL
group GrBCU region RgBCU
group GrBCB region RgBCB
group GrBulk subtract GrPlate GrBCR GrBCL GrBCU GrBCB
# SETS
set group       all density ${myDensity}
variable        myVolume equal ($h)^2
set group       all volume ${myVolume}
# DEFINE CYLINDER (Take the next two lines off for the case without the hole)
region cyld_in cylinder z 0 0 0.098 0 0 units box
delete_atoms region cyld_in compress no
# TIME INTEGRATION
fix         Fnve all nve_dr
variable    mystep index 1.0
timestep    ${mystep}
# DEFINE COMPUTES
compute C2 all displace/atom # Compute displacement for each particle
# RESULTS
thermo  10
dump    1 all custom 10 dump_file id type x y z c_C2[1] c_C2[2]
run     1
# PRESCRIBED DISPLACEMENTS
variable DispMin equal (-${X1}*0.000100)
variable DispMax equal (${X2}*0.000100)
displace_atoms GrBCR ramp x ${DispMin} ${DispMax} x -${X1} ${X2} units box
displace_atoms GrBCL ramp x ${DispMin} ${DispMax} x -${X1} ${X2} units box
displace_atoms GrBCU ramp y ${DispMin} ${DispMax} y -${X1} ${X2} units box
displace_atoms GrBCB ramp y ${DispMin} ${DispMax} y -${X1} ${X2} units box
displace_atoms all move NULL NULL 0.0 units box
# SET FORCE TO ZERO
fix FxAll all setforce NULL NULL 0.0
fix FxBC1 GrBCR setforce 0.0 NULL 0.0
fix FxBC2 GrBCL setforce 0.0 NULL 0.0
fix FxBC3 GrBCU setforce NULL 0.0 0.0
fix FxBC4 GrBCB setforce NULL 0.0 0.0
run 1000
```

B APPENDIX B. NUMERICAL SOLUTION METHOD

B.1 Plate with prescribed displacements in x

Figures B.1 and B.3 show the displacements and stresses for the plate with Dirichlet boundary conditions and prescribed displacements in the x-direction for the PD grids: 121x121, 241x241 and 601x601.

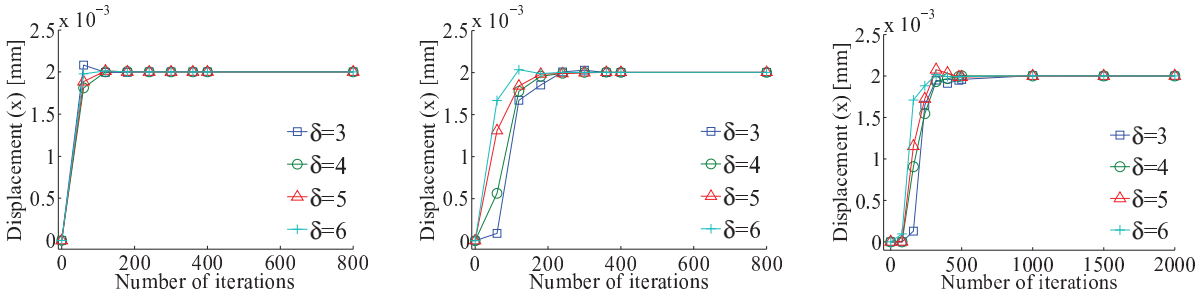

(a) Grid: 121x121 (b) Grid: 241x241 (c) Grid: 601x601

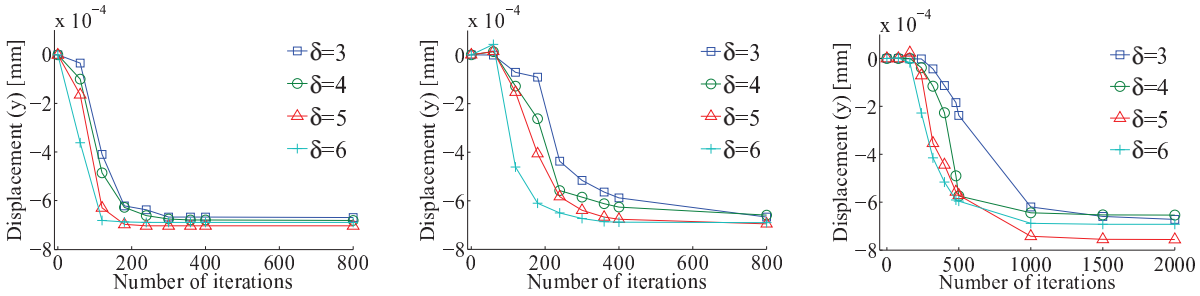

(d) Grid: 121x121 (e) Grid: 241x241 (f) Grid: 601x601

Figura B.1: Displacements at the point $x = y = 20$ mm for the case of the plate without hole and prescribed displacements in x-direction. For all grids we vary the horizon from $\delta = 3\Delta$ to $\delta = 6\Delta$.

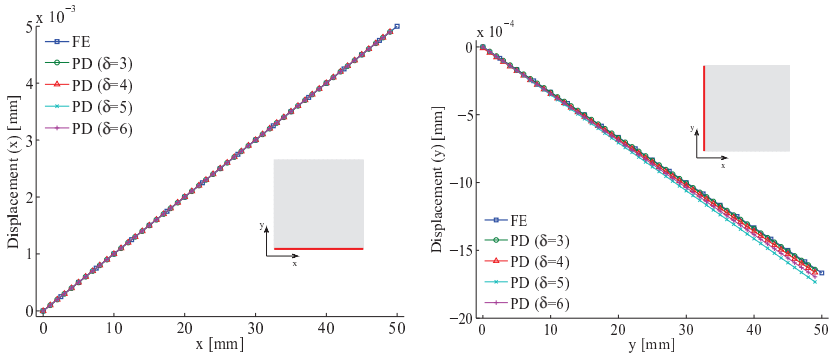

(a) Grid: 121x121 ($y = 0$) (b) Grid: 121x121 ($x = 0$)

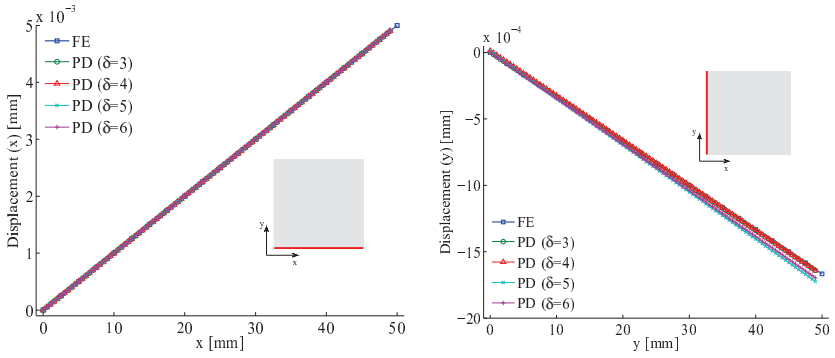

(c) Grid: 241x241 ($y = 0$) (d) Grid: 241x241 ($x = 0$)

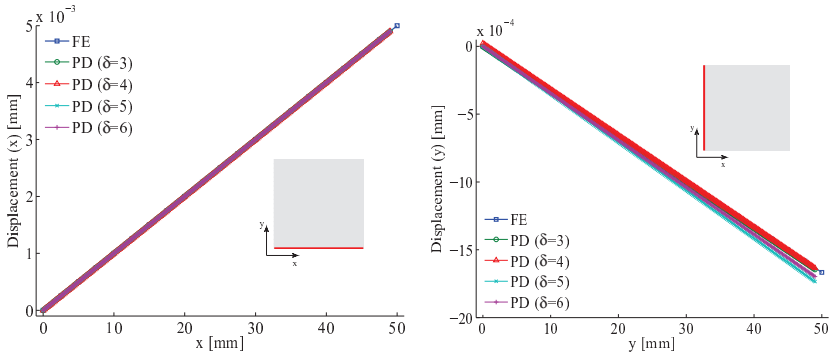

(e) Grid: 601x601 ($y = 0$) (f) Grid: 601x601 ($x = 0$)

Figura B.2: Displacement profiles comparison for the case of the plate without hole and prescribed displacements in the x-direction for the grids: 121x121, 241x241 and 601x601. The extended layers for imposing boundary conditions in the PD model are fixed in 10 mm at each boundary (not shown in the figure). We vary the horizon from $\delta = 3\Delta$ to $\delta = 6\Delta$.

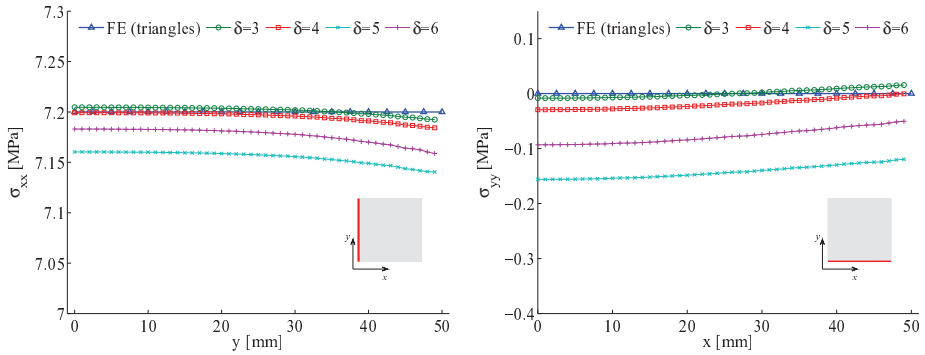

(a) Grid: 121x121 ($x = 0$)

(b) Grid: 121x121 ($y = 0$)

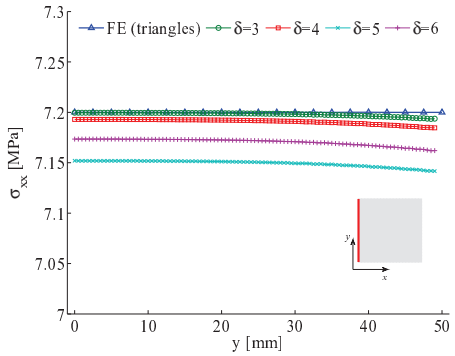

(c) Grid: 241x241 ($x = 0$)

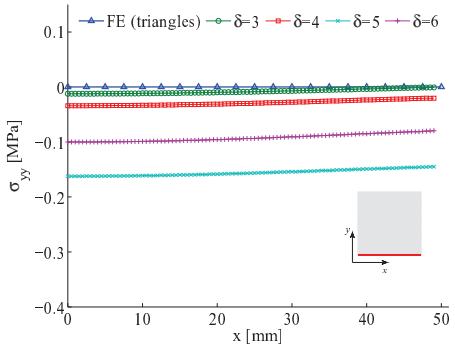

(d) Grid: 241x241 ($y = 0$)

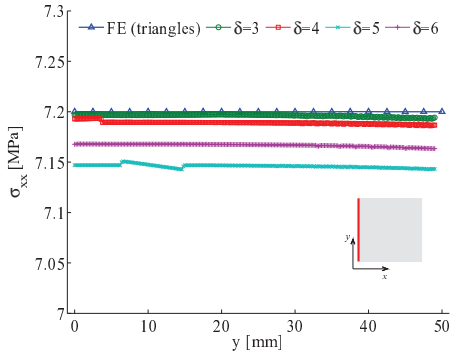

(e) Grid: 601x601 ($x = 0$)

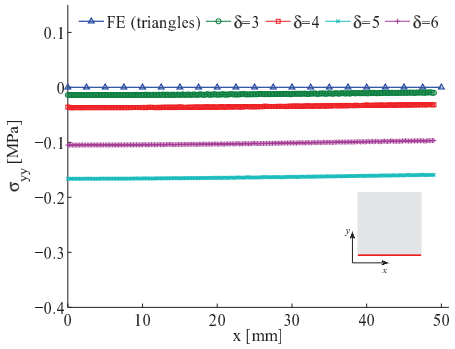

(f) Grid: 601x601 ($y = 0$)

Figura B.3: Stresses comparison for the case of the plate without hole and prescribed displacements in the x-direction for the grids: 121x121, 241x241 and 601x601. The extended layers for imposing boundary conditions in the PD model are fixed in 10 mm at each boundary (not shown in the figure). We vary the horizon from $\delta = 3\Delta$ to $\delta = 6\Delta$.

B.2 Plate with prescribed displacements in x and y

Figures B.4 and B.6 show the displacements and stresses for the plate with Dirichlet boundary conditions and prescribed displacements in both x- and y-direction for the PD grids: 121x121, 241x241 and 601x601.

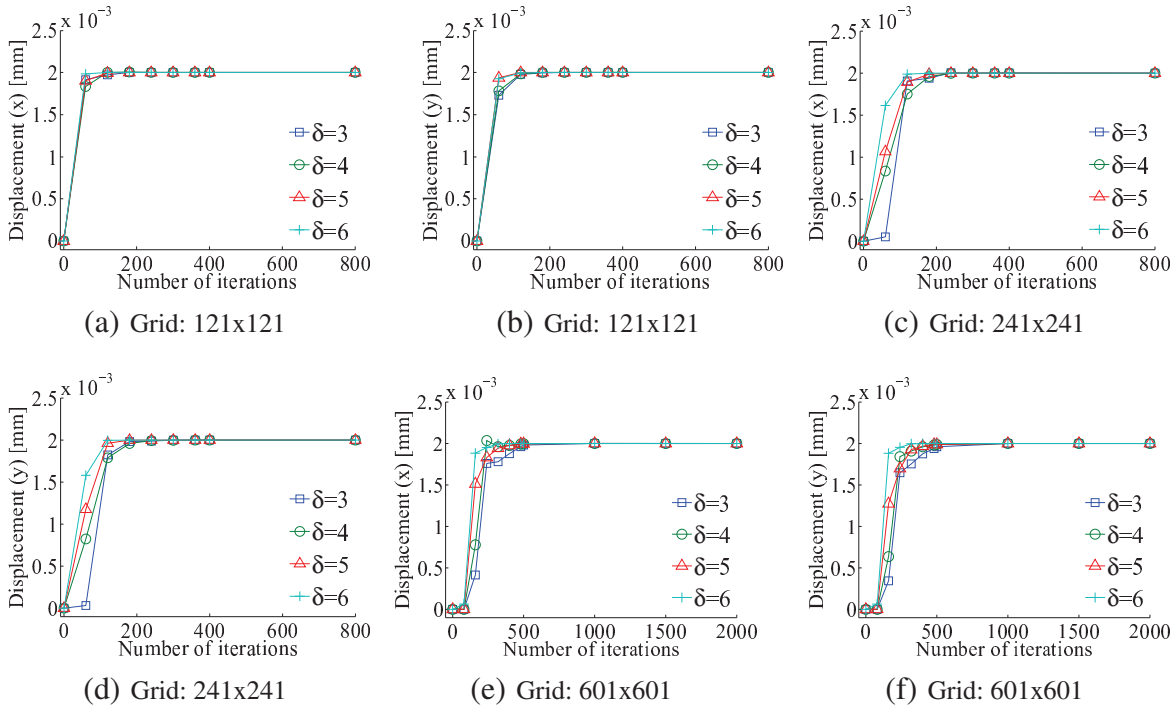

(a) Grid: 121x121 (b) Grid: 121x121 (c) Grid: 241x241

(d) Grid: 241x241 (e) Grid: 601x601 (f) Grid: 601x601

Figura B.4: Displacements at the point $x = y = 20$ mm for the case of the plate without hole and prescribed displacements in both x- and y-direction. For all grids we vary the horizon from $\delta = 3\Delta$ to $\delta = 6\Delta$.

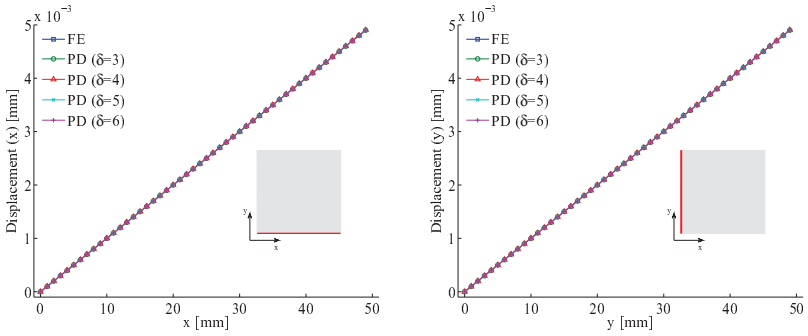

(a) Grid: 121x121 ($y = 0$)

(b) Grid: 121x121 ($x = 0$)

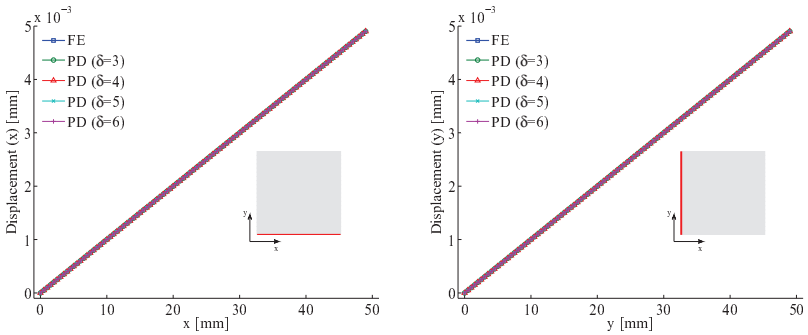

(c) Grid: 241x241 ($y = 0$)

(d) Grid: 241x241 ($x = 0$)

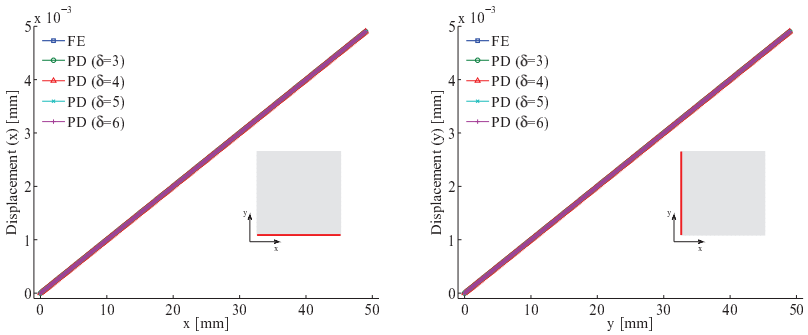

(e) Grid: 601x601 ($y = 0$)

(f) Grid: 601x601 ($x = 0$)

Figura B.5: Displacement profiles comparison for the case of the plate without hole and prescribed displacements in both x- and y-direction for the grids: 121x121, 241x241 and 601x601. The extended layers for imposing boundary conditions in the PD model are fixed in 10 mm at each boundary (not shown in the figure). We vary the horizon from $\delta = 3\Delta$ to $\delta = 6\Delta$.

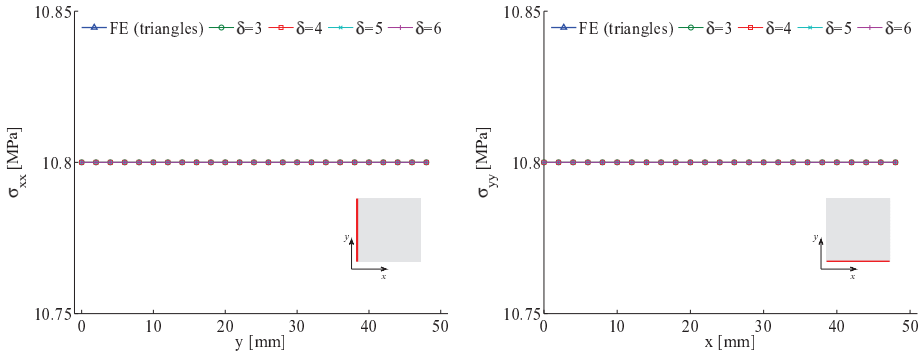

(a) Grid: 121x121 ($x = 0$) (b) Grid: 121x121 ($y = 0$)

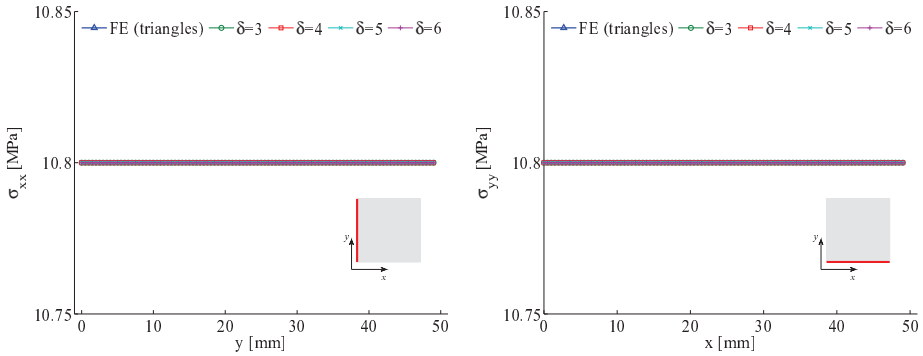

(c) Grid: 241x241 ($x = 0$) (d) Grid: 241x241 ($y = 0$)

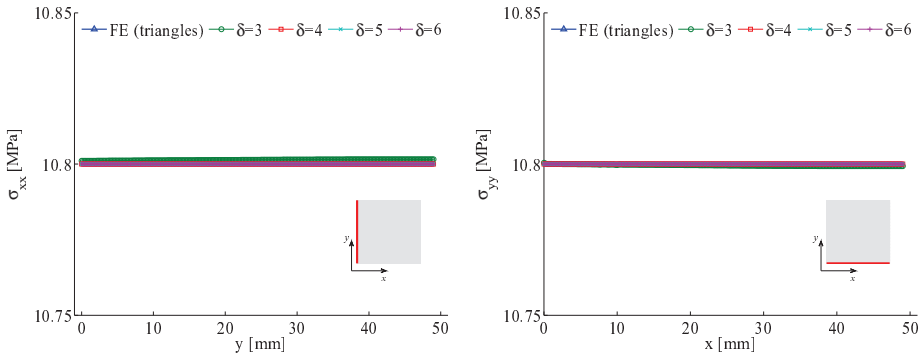

(e) Grid: 601x601 ($x = 0$) (f) Grid: 601x601 ($y = 0$)

Figura B.6: Stresses comparison for the case of the plate without hole and prescribed displacements in both x- and y-direction for the grids: 121x121, 241x241 and 601x601. The extended layers for imposing boundary conditions in the PD model are fixed in 10 mm at each boundary (not shown in the figure). We vary the horizon from $\delta = 3\Delta$ to $\delta = 6\Delta$.

B.3 Plate with hole with prescribed displacements in x

Figures B.7 to B.13 show the displacements and stresses for the plate with hole with Dirichlet boundary conditions and prescribed displacements in the x-direction for the PD grids: 121x121, 241x241 and 601x601.

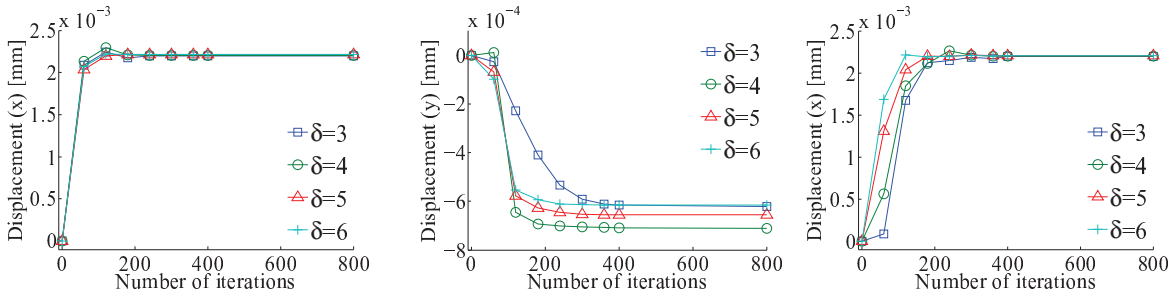

(a) Grid: 121x121

(b) Grid: 121x121

(c) Grid: 241x241

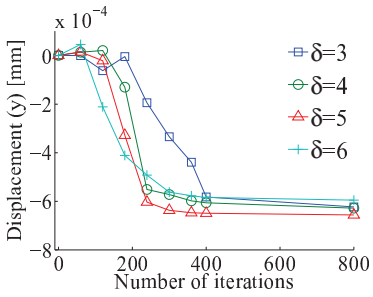

(d) Grid: 241x241

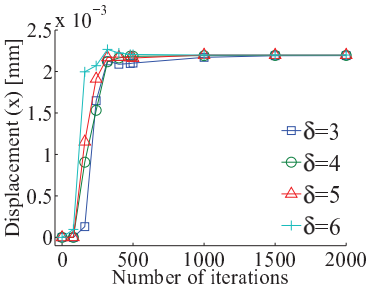

(e) Grid: 601x601

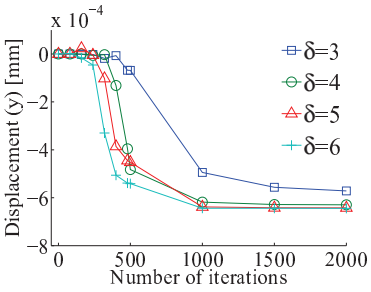

(f) Grid: 601x601

Figura B.7: Displacements at the point $x = y = 20$ mm for the case of the plate with the hole with prescribed displacements in x-direction. For all grids we vary the horizon from $\delta = 3\Delta$ to $\delta = 6\Delta$.

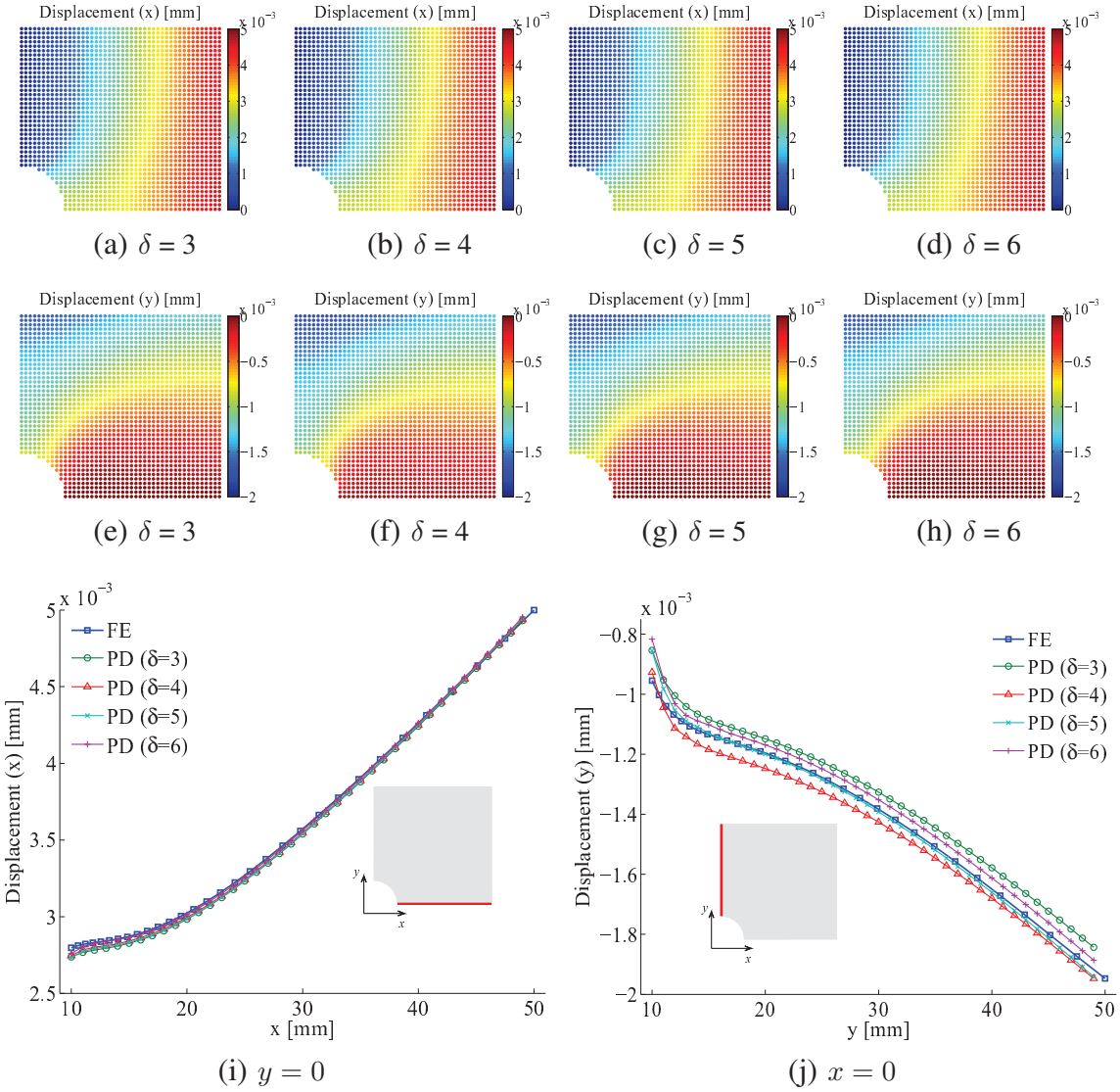

Figura B.8: Displacement distribution for the case of the plate with hole with prescribed displacements in x-direction computed with the 121x121 grid; The extended layers for imposing boundary conditions in the PD model are fixed in 10 mm at each boundary (not shown in the figure). We vary the horizon from $\delta = 3\Delta$ to $\delta = 6\Delta$. In (i) and (j) the displacements in x and y are compared with the FE solution.

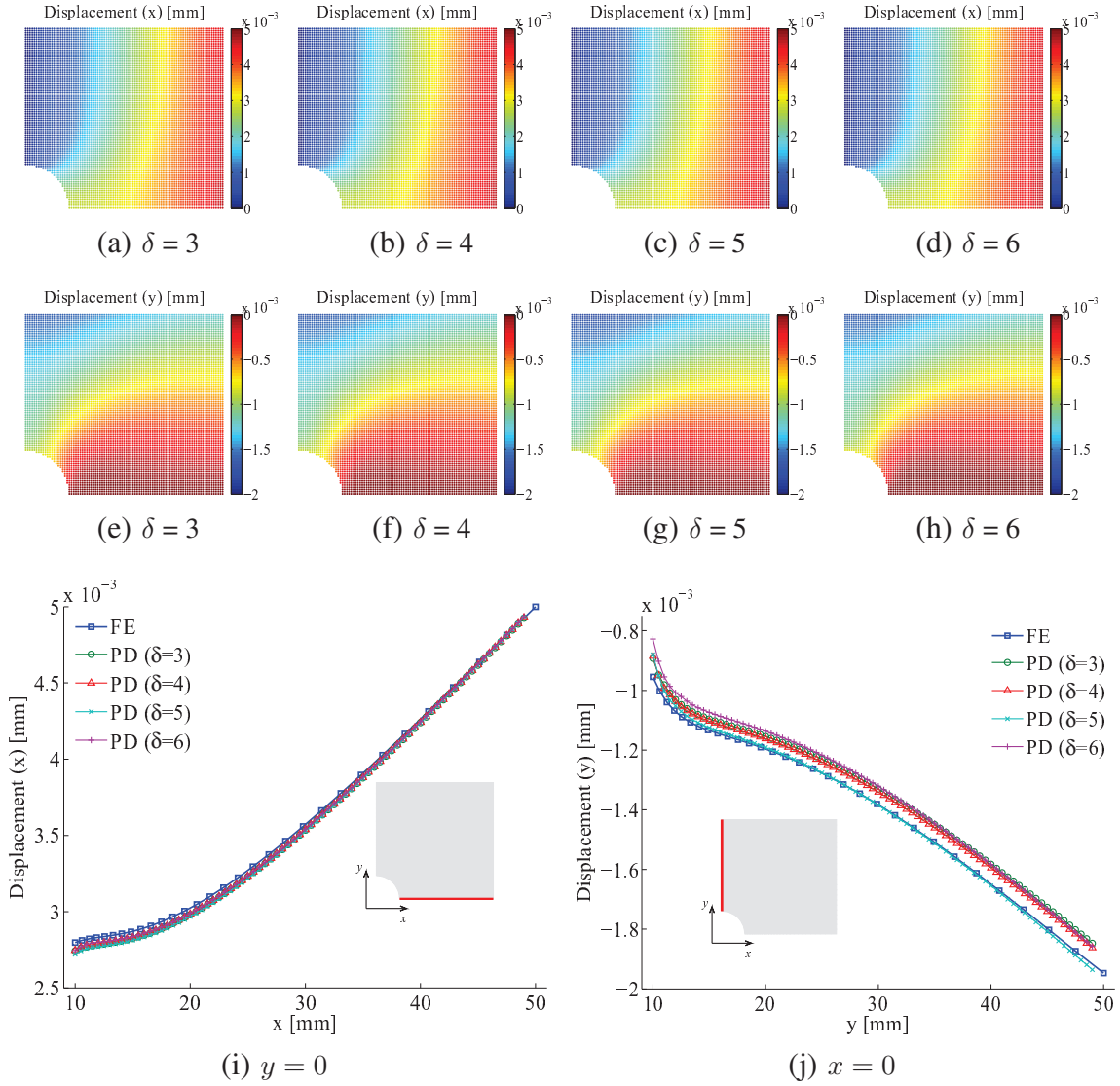

Figura B.9: Displacement distribution for the case of the plate with hole with prescribed displacements in x-direction computed with the 241x241 grid; The extended layers for imposing boundary conditions in the PD model are fixed in 10 mm at each boundary (not shown in the figure). We vary the horizon from $\delta = 3\Delta$ to $\delta = 6\Delta$. In (i) and (j) the displacements in x and y are compared with the FE solution.

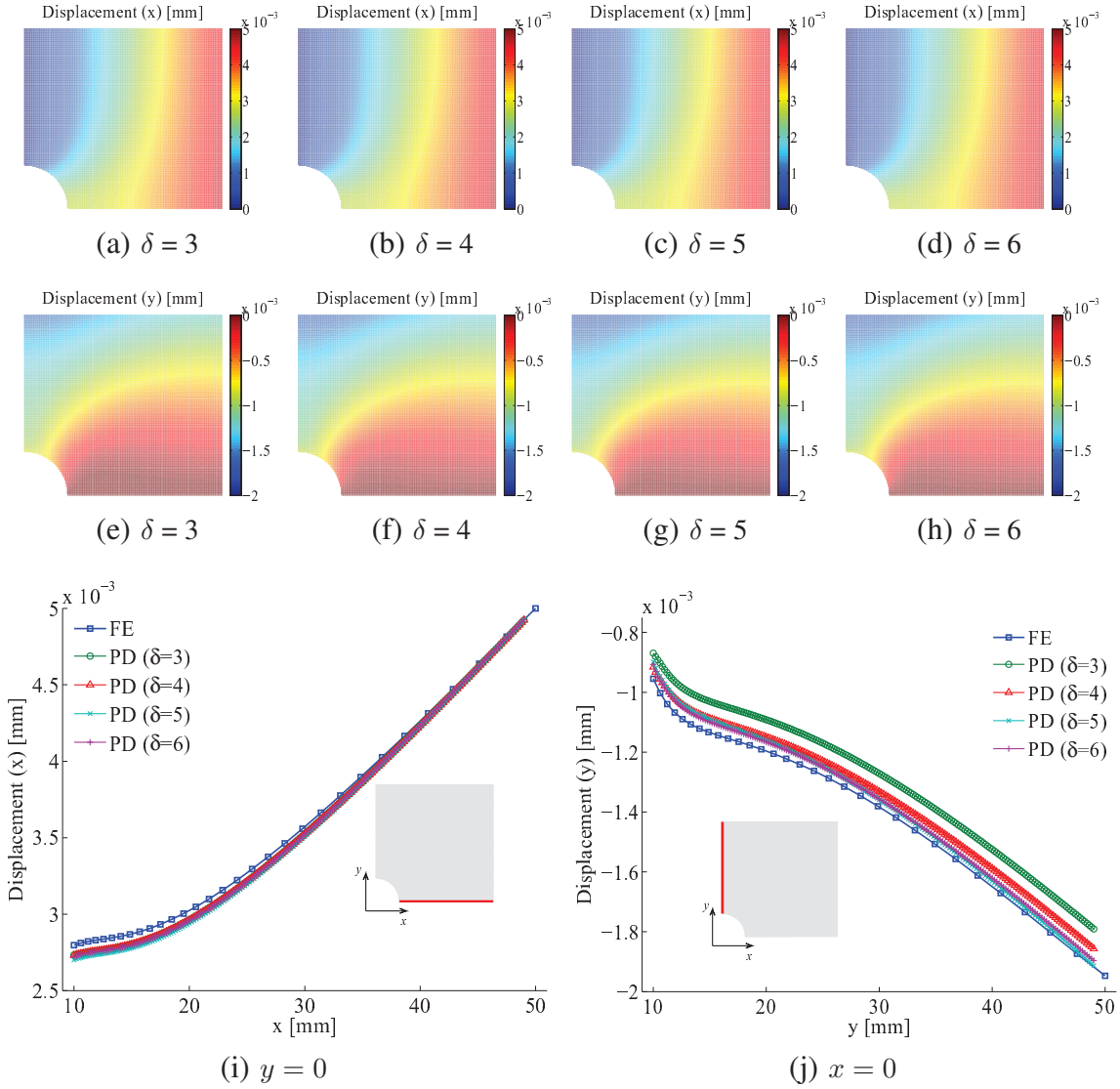

Figura B.10: Displacement distribution for the case of the plate with hole with prescribed displacements in x-direction computed with the 601x601 grid; The extended layers for imposing boundary conditions in the PD model are fixed in 10 mm at each boundary (not shown in the figure). We vary the horizon from $\delta = 3\Delta$ to $\delta = 6\Delta$. In (i) and (j) the displacements in x and y are compared with the FE solution.

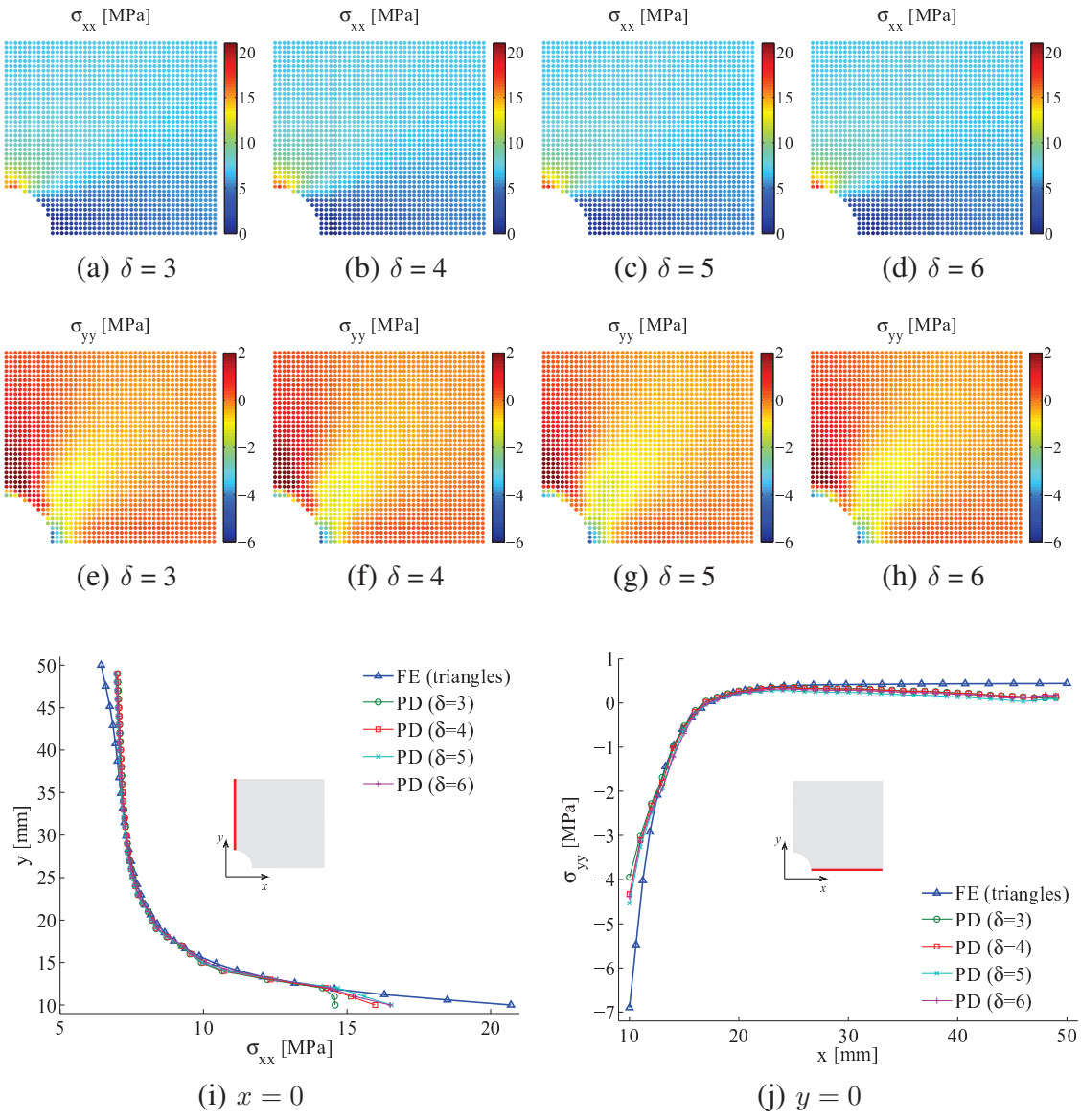

Figura B.11: PD stresses for the case of the plate with hole with prescribed displacements in x-direction computed with the 121x121 grid; The extended layers for imposing boundary conditions in the PD model are fixed in 10 mm at each boundary (not shown in the figure). We vary the horizon from $\delta = 3\Delta$ to $\delta = 6\Delta$. In (i) and (j) σ_{xx} and σ_{yy} are compared with the FE solution.

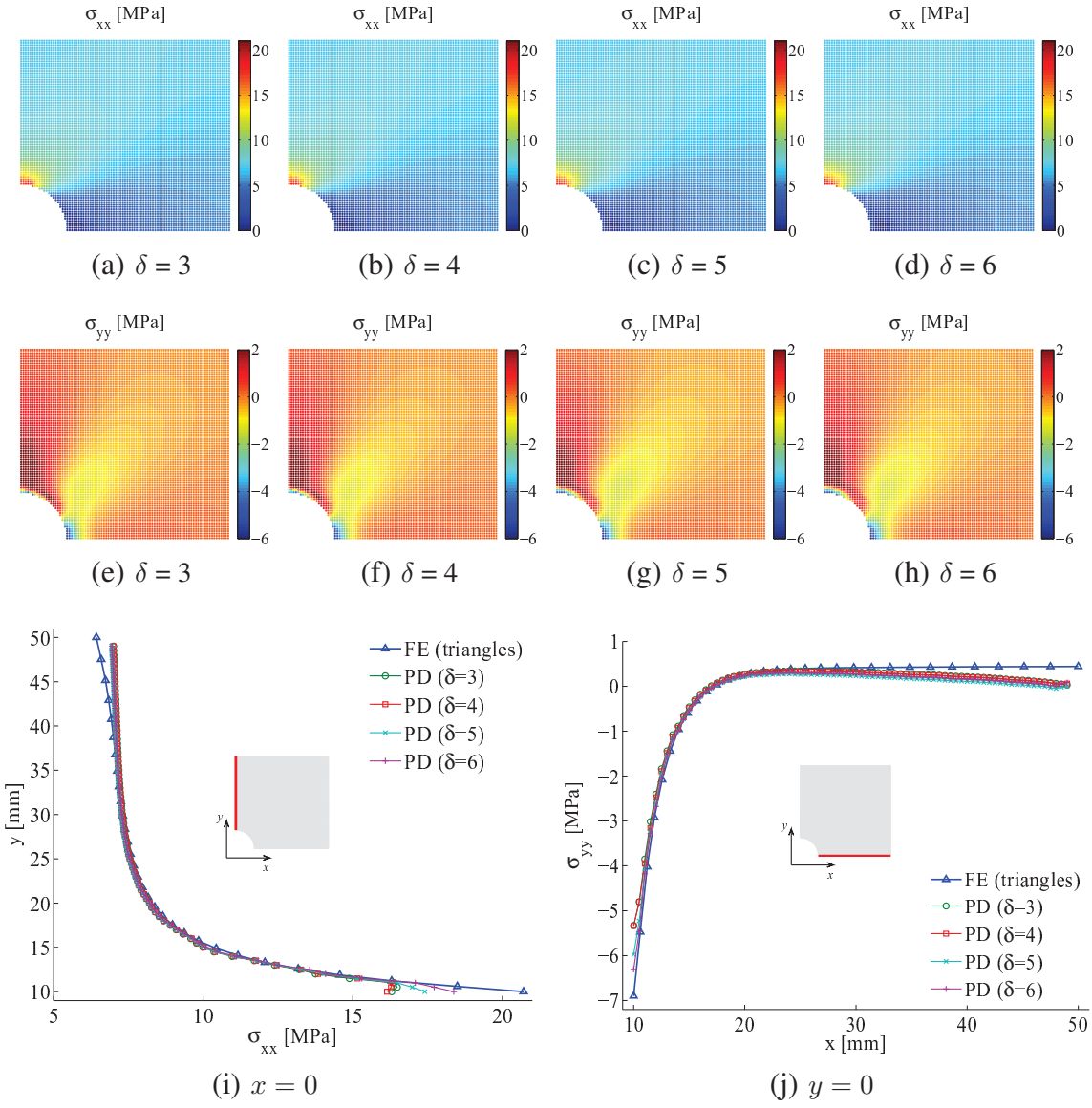

Figura B.12: PD stresses for the case of the plate with hole with prescribed displacements in x-direction computed with the 241x241 grid; The extended layers for imposing boundary conditions in the PD model are fixed in 10 mm at each boundary (not shown in the figure). We vary the horizon from $\delta = 3\Delta$ to $\delta = 6\Delta$. In (i) and (j) σ_{xx} and σ_{yy} are compared with the FE solution.

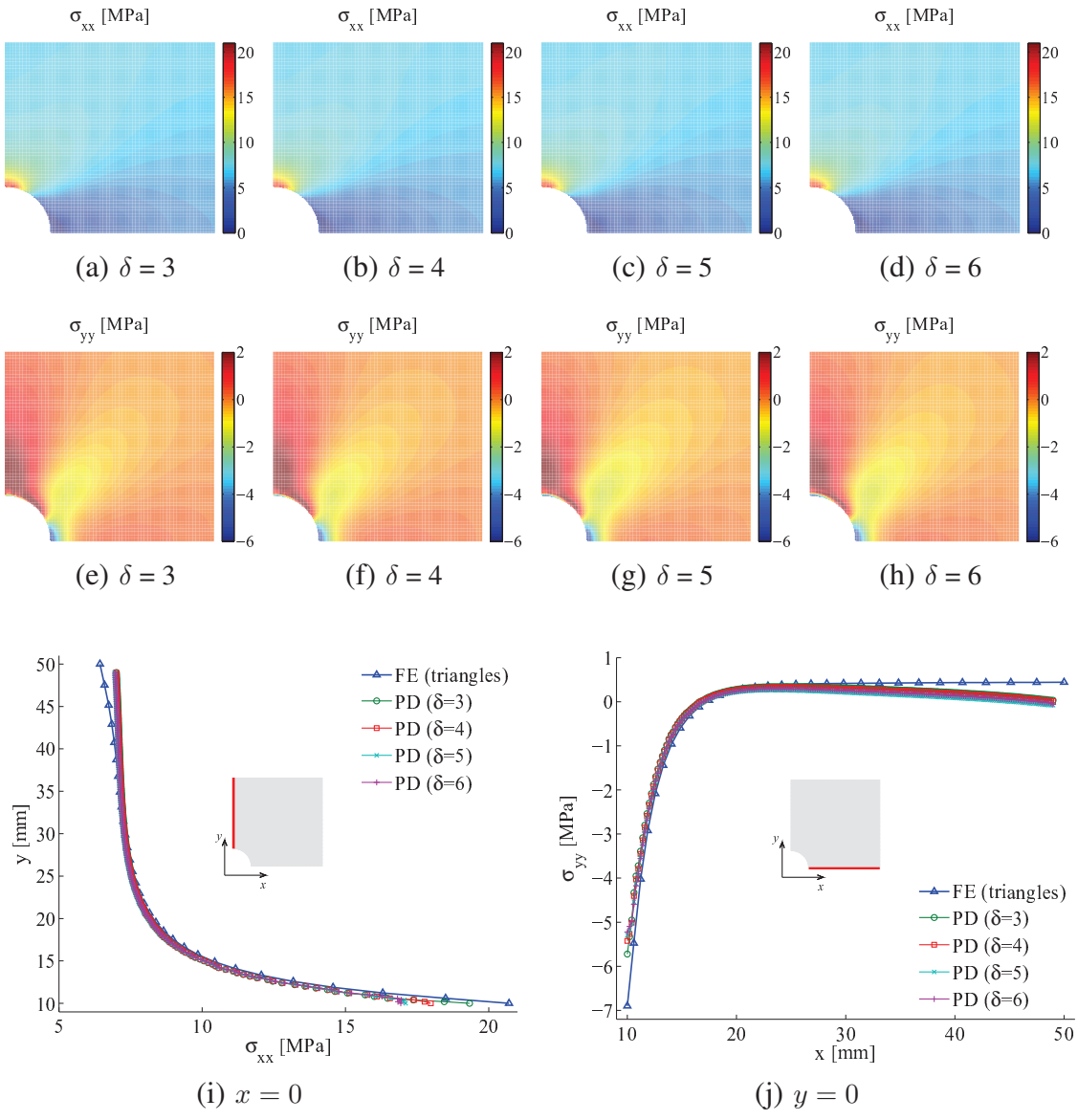

Figura B.13: PD stresses for the case of the plate with hole with prescribed displacements in x-direction computed with the 601x601 grid; The extended layers for imposing boundary conditions in the PD model are fixed in 10 mm at each boundary (not shown in the figure). We vary the horizon from $\delta = 3\Delta$ to $\delta = 6\Delta$. In (i) and (j) σ_{xx} and σ_{yy} are compared with the FE solution.

B.4 Plate with hole with prescribed displacements in x and y

Figures B.14 to B.20 show the displacements and stresses for the plate with hole with Dirichlet boundary conditions and prescribed displacements in both x- and y-direction for the PD grids: 121x121, 241x241 and 601x601.

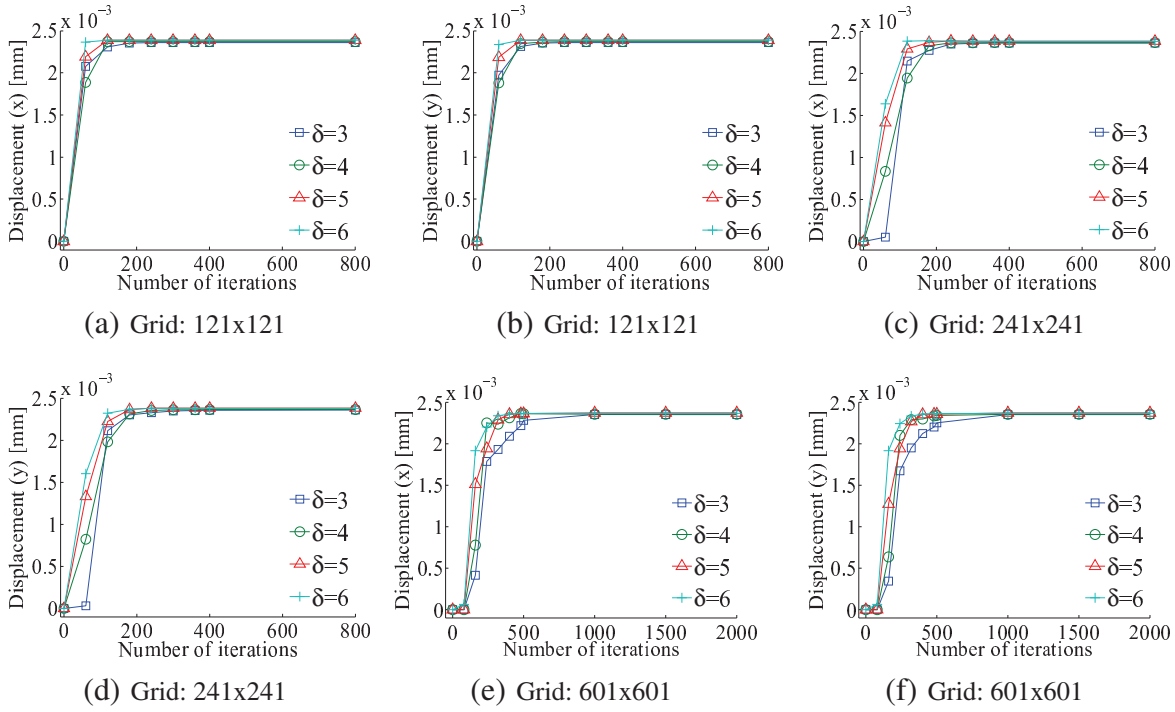

(a) Grid: 121x121 (b) Grid: 121x121 (c) Grid: 241x241

(d) Grid: 241x241 (e) Grid: 601x601 (f) Grid: 601x601

Figura B.14: Displacements at the point $x = y = 20$ mm for the case of the plate with the hole with prescribed displacements in both x- and y-direction. For all grids we vary the horizon from $\delta = 3\Delta$ to $\delta = 6\Delta$.

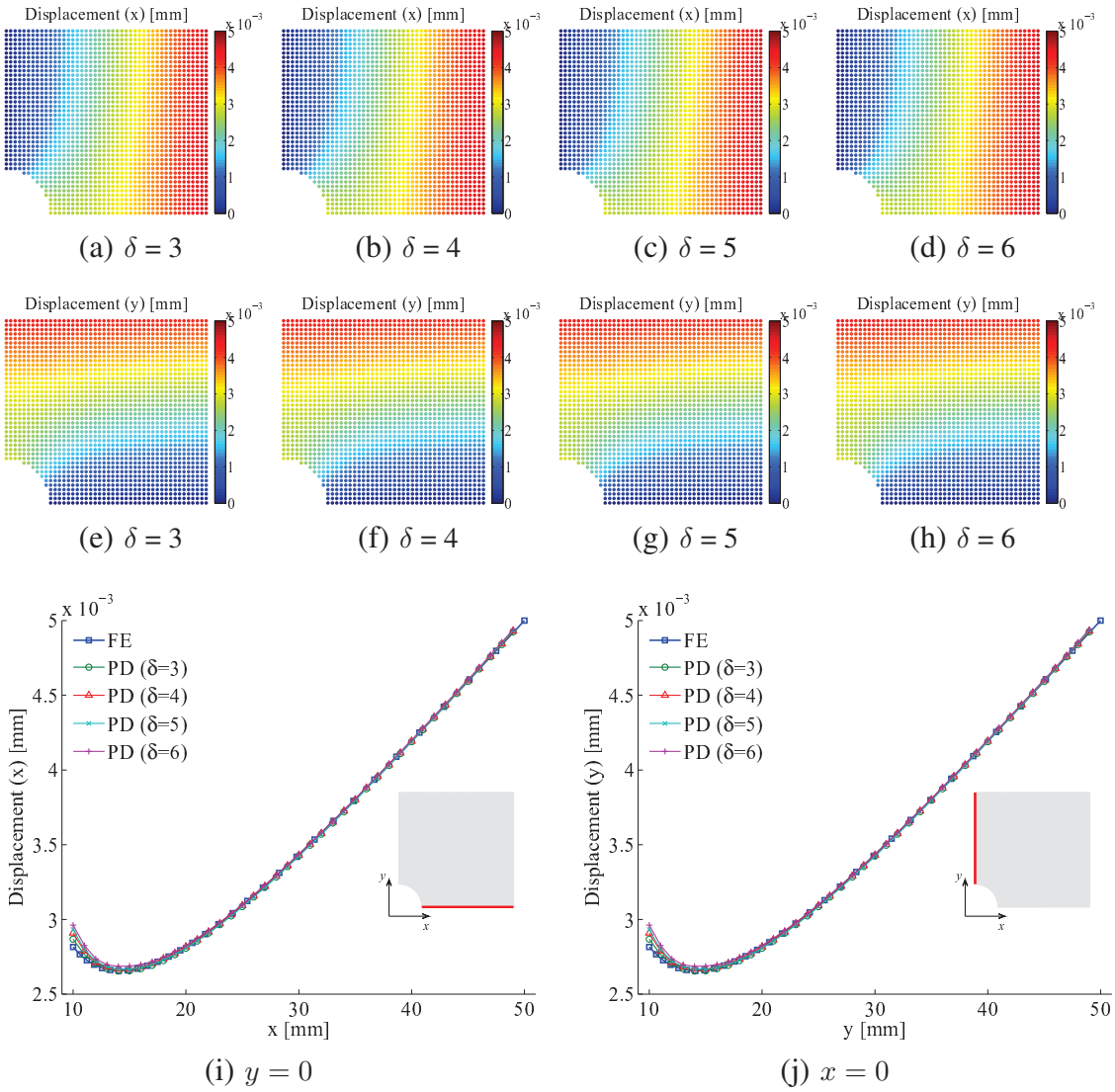

Figura B.15: Displacement distribution for the case of the plate with hole with prescribed displacements in both x- and y-direction computed with the 121x121 grid; The extended layers for imposing boundary conditions in the PD model are fixed in 10 mm at each boundary (not shown in the figure). We vary the horizon from $\delta = 3\Delta$ to $\delta = 6\Delta$. In (i) and (j) the displacements in x and y are compared with the FE solution.

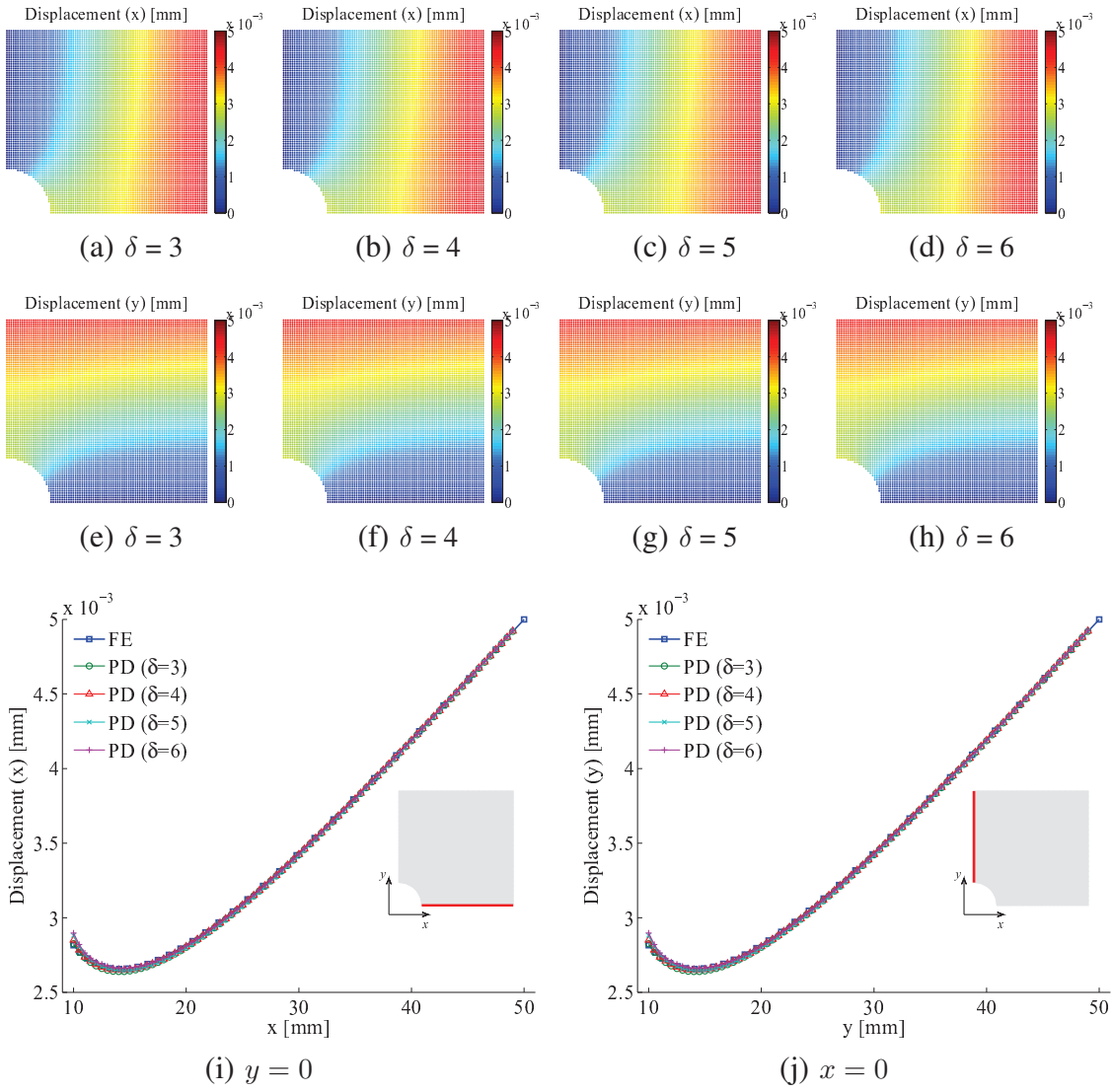

Figura B.16: Displacement distribution for the case of the plate with hole with prescribed displacements in both x- and y-direction computed with the 241x241 grid; The extended layers for imposing boundary conditions in the PD model are fixed in 10 mm at each boundary (not shown in the figure). We vary the horizon from $\delta = 3\Delta$ to $\delta = 6\Delta$. In (i) and (j) the displacements in x and y are compared with the FE solution.

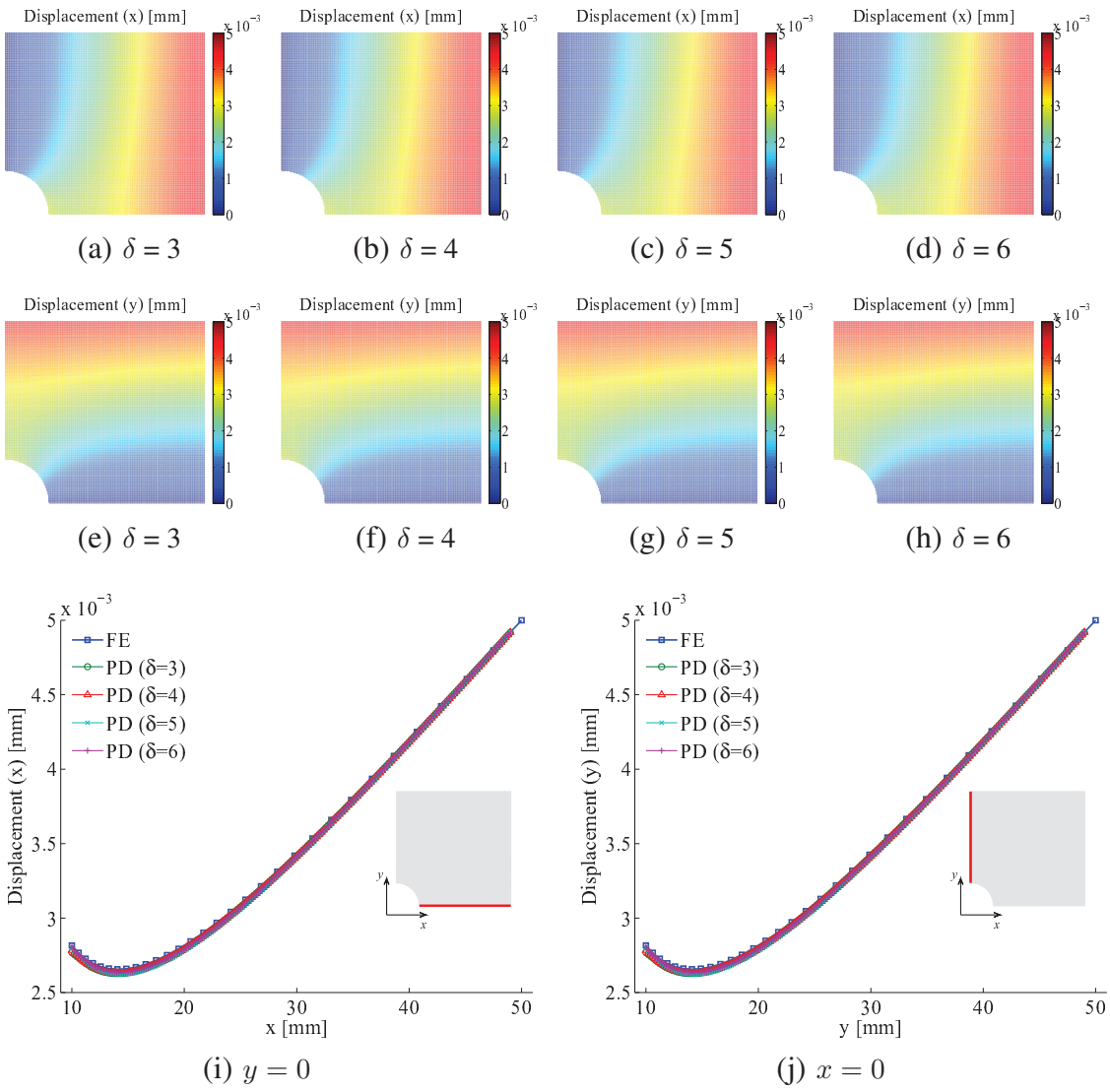

Figura B.17: Displacement distribution for the case of the plate with hole with prescribed displacements in both x- and y-direction computed with the 601x601 grid; The extended layers for imposing boundary conditions in the PD model are fixed in 10 mm at each boundary (not shown in the figure). We vary the horizon from $\delta = 3\Delta$ to $\delta = 6\Delta$. In (i) and (j) the displacements in x and y are compared with the FE solution.

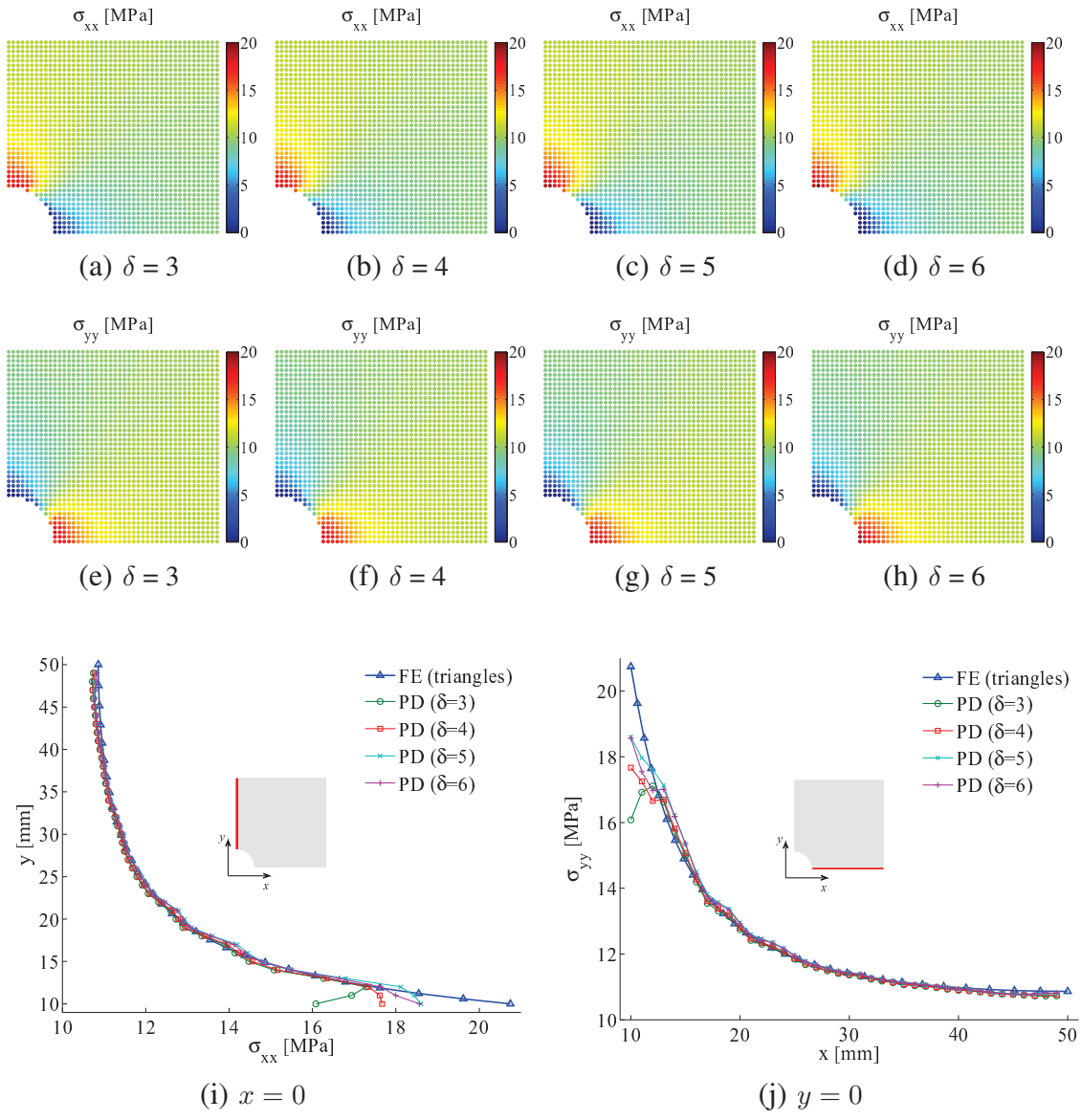

Figura B.18: PD stresses for the case of the plate with hole with prescribed displacements in both x- and y-direction computed with the 121x121 grid; The extended layers for imposing boundary conditions in the PD model are fixed in 10 mm at each boundary (not shown in the figure). We vary the horizon from $\delta = 3\Delta$ to $\delta = 6\Delta$. In (i) and (j) σ_{xx} and σ_{yy} are compared with the FE solution.

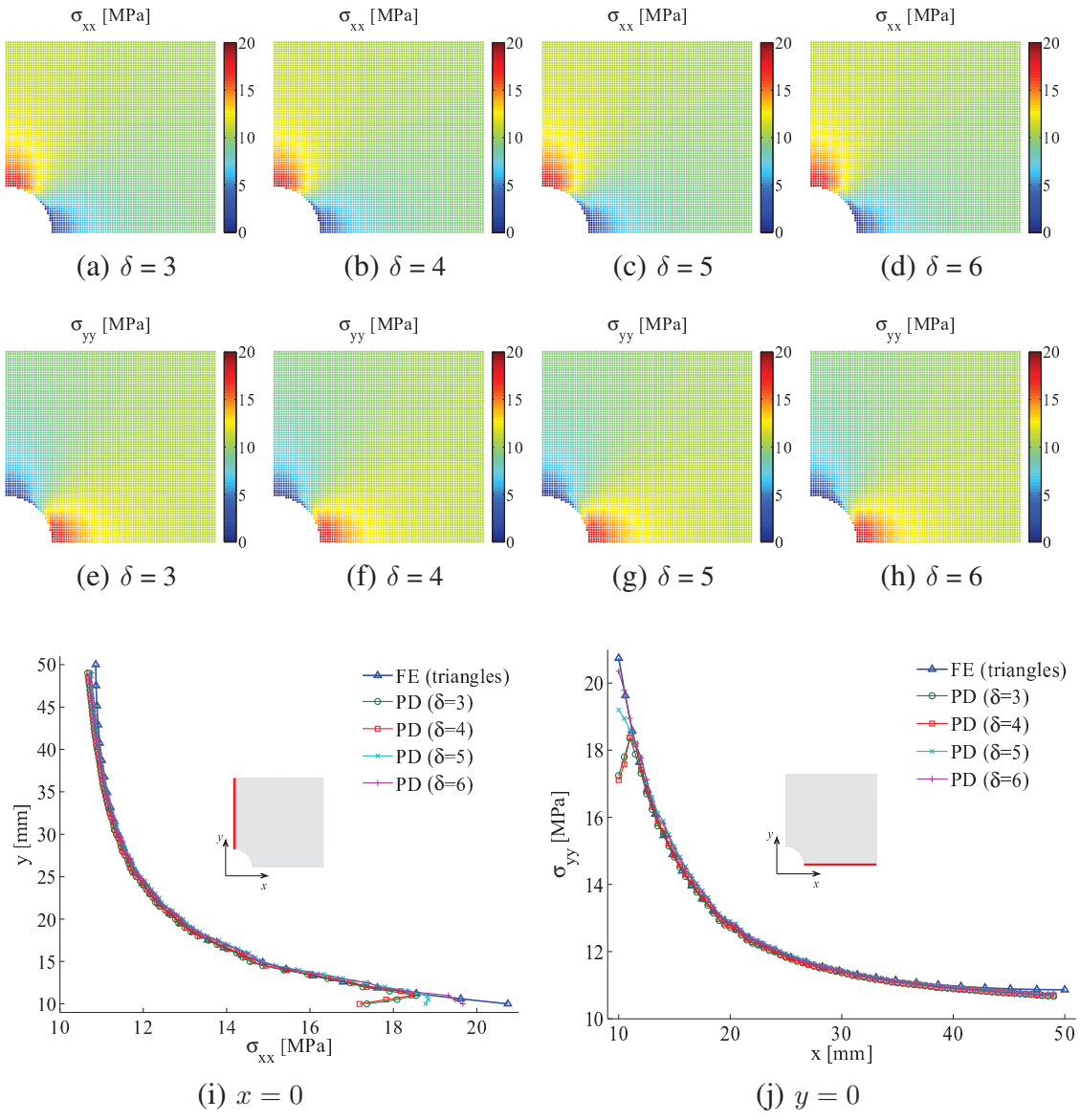

Figura B.19: PD stresses for the case of the plate with hole with prescribed displacements in both x- and y-direction computed with the 241x241 grid; The extended layers for imposing boundary conditions in the PD model are fixed in 10 mm at each boundary (not shown in the figure). We vary the horizon from $\delta = 3\Delta$ to $\delta = 6\Delta$. In (i) and (j) σ_{xx} and σ_{yy} are compared with the FE solution.

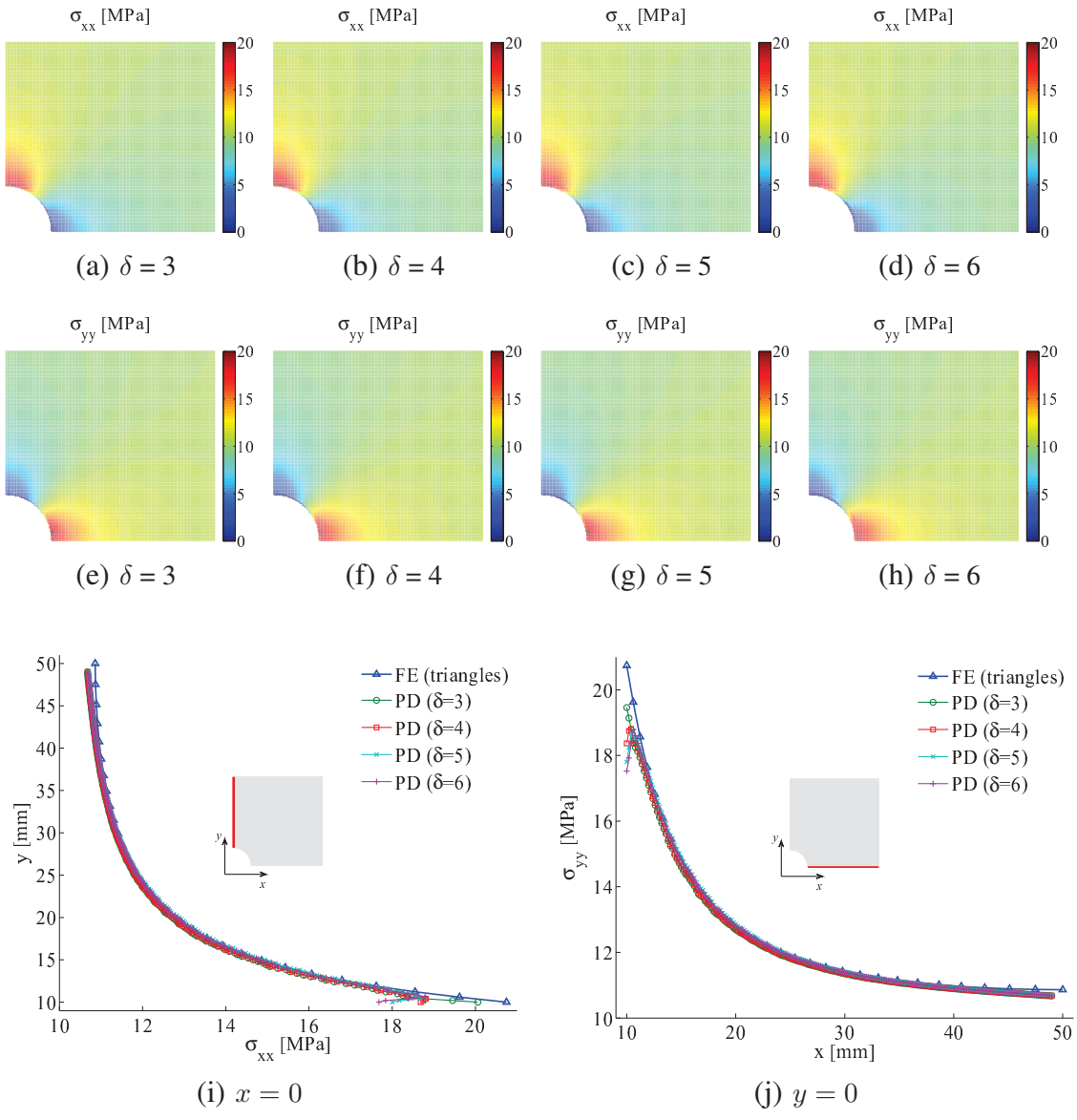

Figura B.20: PD stresses for the case of the plate with hole with prescribed displacements in both x- and y-direction computed with the 601x601 grid; The extended layers for imposing boundary conditions in the PD model are fixed in 10 mm at each boundary (not shown in the figure). We vary the horizon from $\delta = 3\Delta$ to $\delta = 6\Delta$. In (i) and (j) σ_{xx} and σ_{yy} are compared with the FE solution.

C APPENDIX C. POST-PROCESSING THE FE SOLUTION

We calculate the stresses for the FE solution of the problem of Section 4.2.3 using a triangular mesh obtained by a Delaunay triangulation on the FE quadrilateral mesh. This procedure results in a triangular mesh with 1722 elements and 927 nodes. In Figure C.1 we notice that the computed stresses using quadrilateral and triangular meshes agrees quite well.

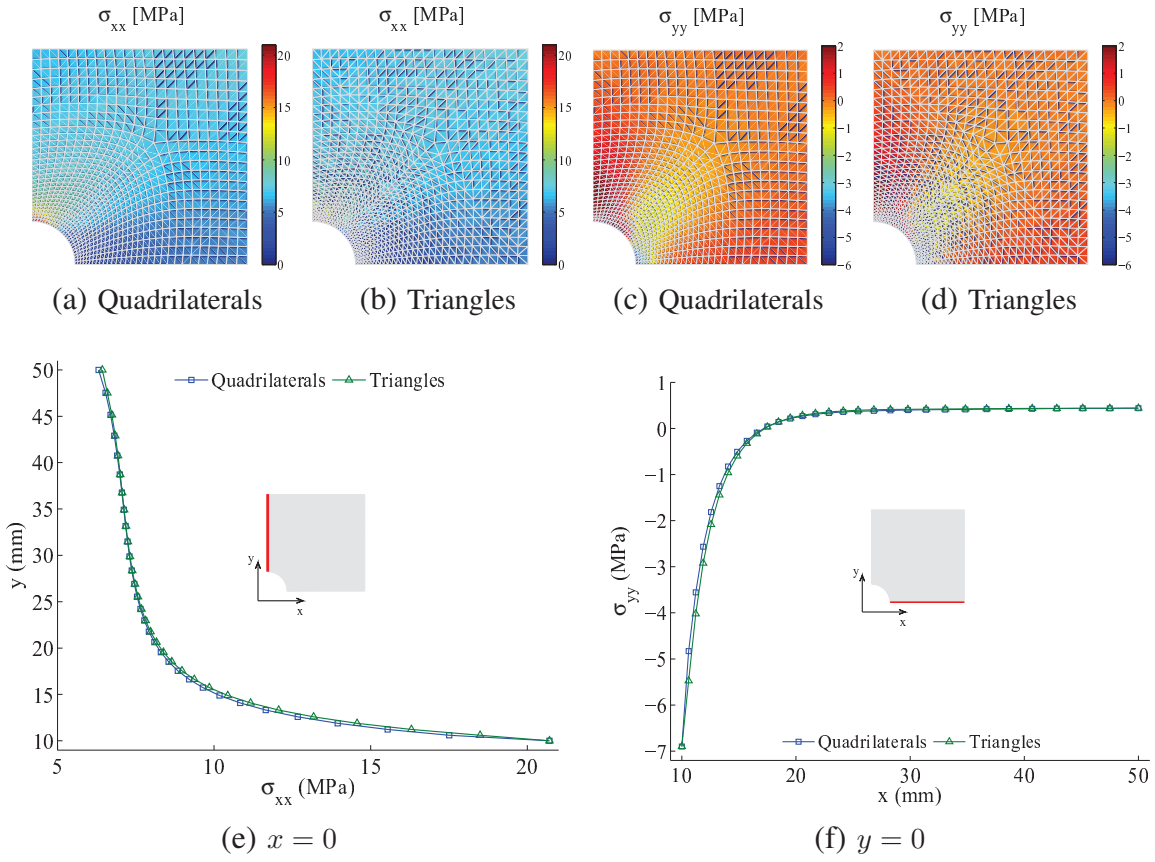

(a) Quadrilaterals (b) Triangles (c) Quadrilaterals (d) Triangles

(e) $x = 0$ (f) $y = 0$

Figura C.1: Stress field using two different meshes for post-processing. The solution was obtained using the quadrilateral mesh shown. Using this quadrilateral mesh, a mesh of triangles was generated and used to compute the stress field. The two plotted curves show that the stress field computed with the triangular mesh is very close to the one using the quadrilateral (the same mesh used for resolving the problem).

REFERENCES

ABRAHAM, F.F.; BROUGHTON, J.Q.; BERNSTEIN, N. and KAXIRAS, E. Spanning the continuum to quantum length scales in a dynamic simulation of brittle fracture. **EPL (Europhysics Letters)**, v. 44, n. 6, 783, 1998.

AGUIAR, A.R. and FOSDICK, R. A constitutive model for a linearly elastic peridynamic body. **Mathematics and Mechanics of Solids**, 2013.

AGWAI, A.; GUVEN, I. and MADENCI, E. Damage prediction for electronic package drop test using finite element method and peridynamic theory. In **Electronic Components and Technology Conference, 2009. ECTC 2009. 59th**, pp. 565–569. May 2009.

ASKARI, E.; BOBARU, F.; LEHOUCQ, R.B.; PARKS, M.L.; SILLING, S.A. and WECKNER, O. Peridynamics for multiscale materials modeling. **Journal of Physics: Conference Series**, v. 125, n. 1, 012078, 2008.

BADIA, S.; NOBILE, F. and VERGARA, C. Fluid-structure partitioned procedures based on robin transmission conditions. **Journal of Computational Physics**, v. 227, n. 14, 7027 – 7051, 2008.

BARNES, M.R. Form-finding and analysis of prestressed nets and membranes. **Computers and Structures**, v. 30, n. 3, 685 – 695, 1988.

BATHE, K.J. **Finite Element Procedures**. Prentice-Hall, New Jersey, 1996.

BAŽANT, Z. and JIRÁSEK, M. Nonlocal integral formulations of plasticity and damage: Survey of progress. **Journal of Engineering Mechanics**, v. 128, n. 11, 1119–1149, 2002.

BELYTSCHKO, T.; GRACIE, R. and VENTURA, G. A review of extended/generalized finite element methods for material modeling. **Modelling and Simulation in Materials Science and Engineering**, v. 17, n. 4, 043001, 2009.

BOBARU, F. and DUANGPANYA, M. The peridynamic formulation for transient heat conduction. **International Journal of Heat and Mass Transfer**, v. 53, 4047 – 4059, 2010.

BOBARU, F. and DUANGPANYA, M. A peridynamic formulation for transient heat conduction in bodies with evolving discontinuities. **Journal of Computational Physics**, v. 231, n. 7, 2764 – 2785, Apr 2012.

BOBARU, F.; YANG, M.; ALVES, L.F.; SILLING, S.A.; ASKARI, E. and XU, J. Convergence, adaptive refinement, and scaling in 1d peridynamics. **International Journal for Numerical Methods in Engineering**, v. 77, n. 6, 852–877, 2009.

BROUGHTON, J.Q.; ABRAHAM, F.F.; BERNSTEIN, N. and KAXIRAS, E. Concurrent coupling of length scales: Methodology and application. **Phys. Rev. B**, v. 60, 2391–2403, Jul 1999.

BUEHLER, M.J. **Atomistic modeling of materials failure**. Springer (New York), 2008.

DE SOUZA NETO, E.A.; PERIC, D. and OWEN, D.R.J. **Computational methods for plasticity: theory and applications**. Wiley, 2011.

DU, Q. and ZHOU, K. Mathematical analysis for the peridynamic nonlocal continuum theory. **ESAIM: Mathematical Modelling and Numerical Analysis**, v. 45, n. 02, 217–234, 2011.

DUPUY, L.M.; TADMOR, E.B.; MILLER, R.E. and PHILLIPS, R. Finite-temperature quasicontinuum: Molecular dynamics without all the atoms. **Phys. Rev. Lett.**, v. 95, 060202, Aug 2005.

EMMRICH, E. and WECKNER, O. Analysis and numerical approximation of an integro-differential equation modeling non-local effects in linear elasticity. **Mathematics and Mechanics of Solids**, v. 12, n. 4, 363–384, 2007a.

EMMRICH, E. and WECKNER, O. On the well-posedness of the linear peridynamic model and its convergence towards the navier equation of linear elasticity. **Commun. Math. Sci**, v. 5, n. 4, 851–864, 2007b.

ERDOGAN, F. Fracture mechanics. **International Journal of Solids and Structures**, v. 37, 171–183, 2000.

FISH, J.; NUGGEHALLY, M.A.; SHEPHARD, M.S.; PICU, C.R.; BADIA, S.; PARKS, M.L. and GUNZBURGER, M. Concurrent atc coupling based on a blend of the continuum stress and the atomistic force. **Computer Methods in Applied Mechanics and Engineering**, v. 196, 4548 – 4560, 2007.

FOSTER, J.T.; SILLING, S.A. and CHEN, W.W. Viscoplasticity using peridynamics. **International Journal for Numerical Methods in Engineering**, v. 81, n. 10, 1242–1258, 2010.

FRANTZDALE, B.; PLIMPTON, S. and SHEPHARD, M. Software components for parallel multiscale simulation: an example with lammps. **Engineering with Computers**, v. 26, 205–211, 2010.

GRIEBEL, M.; KNAPEK, S. and ZUMBUSCH, G. **Numerical simulation in molecular dynamics**. Springer Berlin, 2007.

HAN, S.E. and LEE, K.S. A study of the stabilizing process of unstable structures by dynamic relaxation method. **Computers and Structures**, v. 81, n. 17, 1677 – 1688, 2003.

HAWKEN, D.F.; GOTTLIEB, J.J. and HANSEN, J.S. Review of some adaptive node-movement techniques in finite-element and finite-difference solutions of partial differential equations. **Journal of Computational Physics**, v. 95, n. 2, 254–302, 1991.

KILIC, B. **Peridynamic theory for progressive failure prediction in homogeneous and heterogeneous materials**. 2008. Tese (Doutorado). The University of Arizona.

KOHLHOFF, S.; GUMBSCH, P. and FISCHMEISTER, H.F. Crack propagation in b.c.c. crystals studied with a combined finite-element and atomistic model. **Philosophical Magazine A**, v. 64, n. 4, 851–878, 1991.

LEE, K.S.; HAN, S.E. and PARK, T. A simple explicit arc-length method using the dynamic relaxation method with kinetic damping. **Computers and Structures**, v. 89, n. 1-2, 216 – 233, 2011.

LEHOUCQ, R.B. and SEARS, M.P. Statistical mechanical foundation of the peridynamic nonlocal continuum theory: Energy and momentum conservation laws. **Phys. Rev. E**, v. 84, 031112, Sep 2011.

LEHOUCQ, R.B. and SILLING, S.A. Force flux and the peridynamic stress tensor. **Journal of the Mechanics and Physics of Solids**, v. 56, n. 4, 1566 – 1577, 2008.

LIU, W. and HONG, J.W. A coupling approach of discretized peridynamics with finite element method. **Computer Methods in Applied Mechanics and Engineering**, v. 15, 163 – 175, Oct 2012.

MACEK, R.W. and SILLING, S.A. Peridynamics via finite element analysis. **Finite Elements in Analysis and Design**, v. 43, n. 15, 1169 – 1178, 2007.

MILLER, R. and TADMOR, E.B. The quasicontinuum method: Overview, applications and current directions. **Journal of Computer-Aided Materials Design**, v. 9, 203–239, 2002.

MULLINS, M. and DOKAINISH, M.A. Simulation of the (001) plane crack in a-iron employing a new boundary scheme. **Philosophical Magazine A**, v. 46, n. 5, 771–787, 1982.

OTERKUS, E. **Peridynamic theory for modeling three-dimensional damage growth in metallic and composite structures**. 2010. Tese (Doutorado). The University of Arizona.

PARK, H.S. and LIU, W.K. An introduction and tutorial on multiple-scale analysis in solids. **Computer Methods in Applied Mechanics and Engineering**, v. 193, 1733 – 1772, 2004.

PARKS, M.L.; BOCHEV, P. and LEHOUCQ, R. Connecting atomistic-to-continuum coupling and domain decomposition. **Multiscale Modeling and Simulation**, v. 7, n. 1, 362–380, 2008a.

PARKS, M.L.; LEHOUCQ, R.B.; PLIMPTON, S.J. and SILLING, S.A. Implementing peridynamics within a molecular dynamics code. **Computer Physics Communications**, v. 179, n. 11, 777 – 783, 2008b.

PARKS, M.L.; LITTLEWOOD, D.J.; MITCHELL, J.A. and SILLING, S.A. Peridigm: A new paradigm in computational peridynamics. In **10th World Congress on Computational Mechanics, Sao Paulo, Brazil**. July 2012.

PLIMPTON, S.J. Fast parallel algorithms for short-range molecular dynamics. **J. Comp. Phys.**, v. 117, 1–19, 1995.

URL: *http://lammps.sandia.gov*

PLIMPTON, S.J. Lammps user's manual. **Sandia National Laboraties**, 2013.
URL: *http://lammps.sandia.gov*

RUDD, R.E. and BROUGHTON, J.Q. Coarse-grained molecular dynamics and the atomic limit of finite elements. **Phys. Rev. B**, v. 58, R5893–R5896, Sep 1998.

SELESON, P.; BENEDDINE, S. and PRUDHOMME, S. A force-based coupling scheme for peridynamics and classical elasticity. **Computational Materials Science**, , n. 0, Jun 2012.

SELESON, P. and PARKS, M.L. On the role of the influence function in the peridynamic theory. **International Journal for Multiscale Computational Engineering**, v. 9, n. 6, 689–706, 2011.

SELESON, P.; PARKS, M.L.; GUNZBURGER, M. and LEHOUCQ, R.B. Peridynamics as an upscaling of molecular dynamics. **Multiscale Modeling and Simulation**, v. 8, n. 1, 204, 2009.

SILLING, S.A. Reformulation of elasticity theory for discontinuities and long-range forces. **Journal of the Mechanics and Physics of Solids**, v. 48, n. 1, 175 – 209, 2000.

SILLING, S.A. Dynamic fracture modeling with a meshfree peridynamic code. **Computational fluid and solid mechanics**, pp. 641–644, 2003.

SILLING, S.A. and ASKARI, E. A meshfree method based on the peridynamic model of solid mechanics. **Computers and Structures**, v. 83, 1526 – 1535, 2005.

SILLING, S.A. and BOBARU, F. Peridynamic modeling of membranes and fibers. **International Journal of Non-Linear Mechanics**, v. 40, 395 – 409, 2005.

SILLING, S.A.; EPTON, M.; WECKNER, O.; XU, J. and ASKARI, E. Peridynamic states and constitutive modeling. **Journal of Elasticity**, v. 88, 151–184, 2007.

SILLING, S.A. and LEHOUCQ, R.B. Convergence of peridynamics to classical elasticity theory. **Journal of Elasticity**, v. 93, 13–37, 2008.

SILLING, S.A. and LEHOUCQ, R.B. Peridynamic theory of solid mechanics. **Advances in Applied Mechanics**, v. 44, 73–68, 2010.

SYMEONIDIS, V. and KARNIADAKIS, G.E. A family of time-staggered schemes for integrating hybrid dpd models for polymers: Algorithms and applications. **Journal of Computational Physics**, v. 218, n. 1, 82 – 101, 2006.

TADMOR, E.B.; ORTIZ, M. and PHILLIPS, R. Quasicontinuum analysis of defects in solids. **Philosophical Magazine A**, v. 73, n. 6, 1529–1563, 1996.

WAGNER, G.J. and LIU, W.K. Coupling of atomistic and continuum simulations using a bridging scale decomposition. **Journal of Computational Physics**, v. 190, n. 1, 249 – 274, 2003.

WAKEFIELD, D.S. Engineering analysis of tension structures: theory and practice. **Engineering Structures**, v. 21, n. 8, 680 – 690, 1999.

WECKNER, O.; MOHAMED, N. and ABDULLAH, N. Viscoelastic material models in peridynamics. **Applied Mathematics and Computation**, v. 219, n. 11, 6039–6043, 2013.

WERNIK, J. and MEGUID, S. Coupling atomistics and continuum in solids: status, prospects, and challenges. **International Journal of Mechanics and Materials in Design**, v. 5, 79–110, 2009.

WILDMAN, R.A. and GAZONAS, G.A. A perfectly matched layer for peridynamics in two dimensions. **Journal of Mechanics of Materials and Structures**, v. 7, n. 8, 765–781, 2013a.

WILDMAN, R.A. and GAZONAS, G.A. Peridynamic simulations of infinite regions using a perfectly matched layer. **Dynamic Behavior of Materials**, v. 1, 223–234, 2013b.

WOOD, R.D. A simple technique for controlling element distortion in dynamic relaxation form-finding of tension membranes. **Computers and Structures**, v. 80, n. 27-30, 2115 – 2120, 2002.

XIAO, S.P. and BELYTSCHKO, T. A bridging domain method for coupling continua with molecular dynamics. **Computer Methods in Applied Mechanics and Engineering**, v. 193, 1645 – 1669, 2004.

XU, M.; TABARRAEI, A.; PACI, J.T.; OSWALD, J. and BELYTSCHKO, T. A coupled quantum/continuum mechanics study of graphene fracture. **International Journal of Fracture**, v. 173, n. 2, 163–173, 2012.

YU, K. **Enhanced integration methods for the peridynamic theory.** 2011. Tese (Doutorado). Kansas State University.

ZHOU, K. and DU, G. Mathematical and numerical analysis of linear peridynamic models with nonlocal boundary conditions. **SIAM Journal on Numerical Analysis**, v. 48, n. 5, 1759–1780, 2010.